Fundamental Numerical Studies of Thermal Stratification Effects in Idealized Urban Areas

Weakly unstable thermal stratification effects on the elongated roll-structures downstream of a high-rise building, and its potential effect on pollutant dispersion in urban areas.

THESIS

submitted in partial satisfaction of the requirements for the degree of

MASTER OF SCIENCE

in Mechanical Engineering (Energy, Flow and Process Technology track)

at Delft University of Technology (TU Delft)

by

Pau Fradera i Soler

February, 2023

FACULTY ADVISORS

Professor Dr. ir. Mathieu Pourquie

Professor Dr. ir. Gerrit Elsinga

TABLE OF CONTENTS

ABSTRACT OF THE THESIS 3

TABLE OF VARIABLES 4

1. Motivation 5

1.1 Introduction 5

1.2 The Turbulent Atmospheric Boundary Layer 6

1.2.1 Buoyancy Effects 6

1.2.2 Character of the Turbulence (Shear vs. Buoyancy) 6

1.2.3 The Unstable Atmospheric Boundary Layer 7

1.3 Global Stability of the Atmospheric Boundary Layer 8

1.3.1 Global Stability 8

1.3.2 Obukhov Length-Scale 9

1.4 Large-Scale Rolls in Atmospheric Boundary Layers 10

1.4.1 Introduction to Large-Scale Rolls 10

1.4.2 Insight from studying the Transition from Neutral to Convective 11

1.5 Purpose, Research Questions and Methodology 15

2. The Scales of Turbulence 17

2.1 Length Scales 17

2.2 Time Scales 19

3. Nek5000 Solver 20

3.1 Spectral Element Methods 20

3.2 Governing Equations 21

3.3 Sub-Grid Scale Modelling 22

4. Turbulent Channel Flow Validation 24

4.1 Isothermal Turbulent Channel Flow 24

4.1.1 Introduction 24

4.1.2 Governing Equations 26

4.1.3 Geometry Domain 27

4.1.4 Fully-Resolved Turbulent Channel Flow 28

4.1.5 Domain Discretization - Mesh 30

4.1.6 Boundary Conditions 30

4.1.7 Simulation Settings 31

4.1.8 Results and Discussion 32

4.2 Non-Isothermal Turbulent Channel 35
4.2.1 Introduction 35
4.2.2 Governing Equations 39
4.2.3 Buoyancy Treatment – Boussinesq Approximation 39
4.2.4 Domain Discretization - Mesh 42
4.2.5 Simulation Settings 44
4.2.6 Results and Discussion 45
5. Surface-Mounted Cube Validation 57
5.1 Introduction 57
5.2 Governing Equations 60
5.3 Domain Discretization - Mesh 60
5.4 Boundary Conditions 63
5.5 Numerical Scheme 65
5.6 Simulation set up considerations 65
5.7 Results and Discussion 67
6. Thermal stratification effects on the rolls behind a high-rise building 74
6.1 Introduction 74
6.2 Governing Equations 76
6.3 Domain Discretization - Mesh 77
6.4 Boundary Conditions 78
6.5 Simulation set up considerations 80
6.6 Results and Discussion 83
6.6.1 Isothermal Flow Case 83
6.6.2 Non-Isothermal Flow Case 86
7. Conclusions and Future Work 92
REFERENCES 94

ABSTRACT OF THE THESIS

Pollution in urban environments is increasingly becoming a major concern for our societies which, together with the increasingly powerful capabilities provided by computational fluid dynamics (CFD), has made pollution dispersion a common topic of research during the last two decades. Several factors are relevant to the dispersion of pollutants in an urban environment, such as the variable roughness of the urban canopy and the thermal stratification conditions. However, the effects of these two factors are only partially understood, especially when it comes to their combined effects.

The present research work has been motivated by an unintuitive strengthening of the streamwise-elongated coherent structures of the atmospheric boundary layer (ABL), observed by Jayaraman & Brasseur (2021), for a certain range of weakly unstable thermal stratification conditions. Such observation evinced the existence of a sweet-spot where the large-scale streamwise-oriented counter-rotating vortical structures, characteristic of any turbulent boundary layer, were able to strengthen themselves by collecting small-scale thermal plumes, eventually creating the so-called large-scale atmospheric rolls. The importance of these findings lies in the fact that large-scale atmospheric rolls are known to be one of the most important structures when it comes to vertical transport of momentum and scalars (i.e. pollutants) in the ABL.

Following from this observation, we hypothesize that the counter-rotating roll structures behind a high-rise building could potentially exhibit a similar behaviour and strengthen themselves under weakly unstable thermal stratification conditions by collecting small-scale thermal plumes. If this was the case, it would enhance large-scale vertical mixing which could be beneficial for street canyon ventilation, reducing urban pollution levels. Therefore, the importance of studying the evolution of the roll structures behind a high-rise building under different thermal stratification conditions becomes evident.

In this regard, the present work has focused on the study of the roll structures behind a high-rise building under different thermal stratification conditions, by means of wall-resolved Large-Eddy Simulations (LES) using the Nek5000 Spectral Element Method (SEM) code. The present work has succeeded in providing a qualitative proof of concept of the presented hypothesis, proving that the rolls behind a surface-mounted cube (model for a high-rise building) under weakly unstable thermal stratification conditions do strengthen themselves in a similar manner as observed by Jayaraman & Brasseur (2021) for the ABL. Moreover, a reliable LES numerical model for simulating flow past a surface-mounted cube (high-rise building) has been built and thoroughly validated against DNS data, tuning the optimal mesh, and simulation and filtering settings.

TABLE OF VARIABLES

k	*Turbulence kinetic energy (TKE)*
$\bar{u}$	*Mean flow velocity, in general $\bar{\phi}$ denotes an averaged quantity.*
u'	*Velocity fluctuation, in general ϕ' denotes a fluctuating quantity.*
t	*Time*
θ_0	*Reference ground temperature*
$\bar{\theta}$	*Mean flow temperature*
θ'	*Temperature fluctuation*
Q_0	*Heat flux from Earth surface to ABL*
ρ	*Fluid density*
ρ_0	*Reference fluid density*
g	*Gravity*
ν	*Kinematic viscosity (molecular diffusion)*
μ	*Dynamic viscosity (molecular diffusion)*
K	*Eddy viscosity coefficient (K-theory)*
l_m	*Mixing length*
κ	*von Kármán constant*
u_τ	*Wall frictional velocity*
Ri	*Richardson number*
z_i	*Height of the capping inversion layer (boundary layer height)*
L	*Obukhov length-scale*
η	*Kolmogorov length-scale*
τ	*Kolmogorov time-scale*
ϵ	*Dissipation rate of turbulent kinetic energy*
c_p	*Specific heat at constant pressure*
λ	*Thermal conductivity*
α	*Thermal diffusivity*

Chapter 1

Motivation

1.1 Introduction

It is estimated by the World Health Organisation (WHO) that 90% of the human population lives in places where air quality exceeds WHO guideline limits. As a consequence, WHO estimates in 4.2 million the number of deaths that are a result of the exposure to ambient (outdoor) air pollution every year. Nowadays, 55% of the human population lives in cities but, according to the predictions by The World Bank, the human population living in cities will be doubled as of 2050, representing by then 70% of the entire world population. Therefore, pollution in urban environments, is and will increasingly be a major issue for our societies.

The arising interest in studying pollution dispersion in urban areas, together with the increasingly powerful capabilities provided by computational fluid dynamics (CFD), has made pollution dispersion a very common topic of research during the last 20 years.

Several factors are relevant to the dispersion of pollutants in an urban environment, such as the variable roughness due to the usually heterogeneous urban canopy, and the thermal stratification conditions. The effects of these two factors are only partially understood, especially when it comes to their combined effects. In the past, it was often assumed that the urban variable-height roughness would induce such a mixing that it would make thermal stratification condition effects negligible. However, recent works such as Tomas, Pourquie & Jonker (2016) [1] have shown that, despite the fact that the mixing indeed reduces the strength of the stratification, the effects of the stratification conditions still influence the internal boundary layer development over large distances, evincing that future works aiming to acquire a better knowledge of the urban atmospheric boundary layer and its effects in pollution dispersion should account for both variable height building and thermal stratification conditions. In this regard, this research work will focus on the study of the roll structures behind a high-rise building under different stratification conditions.

1.2 The Turbulent Atmospheric Boundary Layer

1.2.1 Buoyancy Effects

In large-scale geophysical flows, such as an Atmospheric Boundary Layer (ABL), the influence on turbulence of variations in density cannot be neglected [2]. Therefore, in an ABL we have, in general, a combination of turbulence production by shear, and by buoyancy. Hence, the turbulent kinetic energy (TKE) equation (using Boussinesq approximation) reads as:

$$\frac{Dk}{Dt} = -\overline{u'_\iota u'_\jmath}\frac{\partial \bar{u}_i}{\partial x_j} + \frac{g}{T_0}\overline{u'_\jmath \theta'}\delta_{j3} + \frac{\partial}{\partial x_j}\left[-\overline{k' u'_\jmath} - \frac{1}{\rho_0}\overline{p' u'_\jmath} + \nu\frac{\partial k}{\partial x_j}\right] - \nu\overline{\left(\frac{\partial u'_\iota}{\partial x_\jmath}\right)^2}$$

Where:

$$-\overline{u'_\iota u'_\jmath}\frac{\partial \bar{u}_i}{\partial x_j} \rightarrow Turbulence\ production\ by\ shear$$

$$\frac{g}{T_0}\overline{u'_\jmath \theta'}\delta_{j3} \rightarrow Turbulence\ production\ by\ buoyancy$$

The production of turbulent kinetic energy by means of mean-flow deformation work is always a positive net contribution. On the other hand, the effects of buoyancy can bring either, production or destruction of Turbulent Kinetic Energy (TKE), depending on the stratification condition.

The term $\overline{u'_\jmath \theta'}$ represents a turbulent temperature flux, and can be expressed, using K-theory, as:

$$-\overline{w'\theta'} = K_H\frac{\partial \bar{\theta}}{\partial z}$$

Which allows us to distinguish two cases, depending on the nature of the temperature profile:

$$Temperature\ increasing\ with\ height \rightarrow \frac{\partial \bar{\theta}}{\partial z} > 0 \rightarrow \overline{w'\theta'} < 0$$
$$\rightarrow Destruction\ of\ TKE\ (Stable\ Stratification)$$

$$Temperature\ decreasing\ with\ height \rightarrow \frac{\partial \bar{\theta}}{\partial z} < 0 \rightarrow \overline{w'\theta'} > 0$$
$$\rightarrow Production\ of\ TKE\ (Unstable\ Stratification)$$

1.2.2 Character of the Turbulence (Shear vs. Buoyancy)

There are two different sources of Turbulent Kinetic Energy (TKE): shear production and buoyant production (note that a source may also be negative, i.e. sink, in which case TKE is reduced). In this situation, the character of the turbulence will be determined by their relative strengths, which can be expressed by the (flux) Richardson number:

$$Ri = \frac{\frac{g}{T_0}\overline{w'\theta'}}{\overline{u'_\iota u'_\jmath}\frac{\partial \bar{u}_i}{\partial x_j}} \sim \frac{Buoyant\ turbulence\ production}{Shear\ turbulence\ production}$$

From which 3 different cases can be distinguished:

1. $Ri = 0 \rightarrow Neutral\ \ (Shear - driven\ ABL)$
   Buoyancy effects are negligible, shear is the dominant TKE production term.

2. $Ri < 0 \rightarrow Unstable\ stratification\ (Convective\ or\ Buoyancy - driven\ ABL)$
   Both the shear and the buoyancy production terms are sources of TKE. Therefore, their combined action results in increased turbulence intensity.

3. $Ri > 0 \rightarrow Stable\ stratification\ (Stably\ stratified\ ABL)$
   The buoyancy "production" term acts destroying TKE. Therefore, such a flow has a low turbulence intensity.

In both non-neutral cases, the more the Richardson number deviates from 0, the more that buoyancy will dominate over shear. For instance, if $Ri \ll 0$, buoyancy effects will be totally dominant, this situation being known as a fully-convective boundary layer (CBL).

On the other hand, the situation in which $Ri < 0$, but still satisfying: $|Ri| \sim O(1)$, is known as a weakly unstable stratified boundary layer. In these conditions, both shear-production and buoyant-production are relevant, and their combined effect will determine the features of the turbulence.

1.2.3 The Unstable Atmospheric Boundary Layer

The stratification nature of the ABL changes over the day. To briefly introduce the Stably Stratified ABL and the Unstably Stratified ABL (Convective) profiles, figures 1 & 2 show two illustrations from Stull (1988) [3], which is a great reference for a detailed explanation of the Atmospheric Boundary Layer.

Roughly speaking, the ABL tends to its stability situation, where lighter hot air rises through the ABL, giving place to the Stably Stratified BL shown in figure 1, which usually takes place during night.

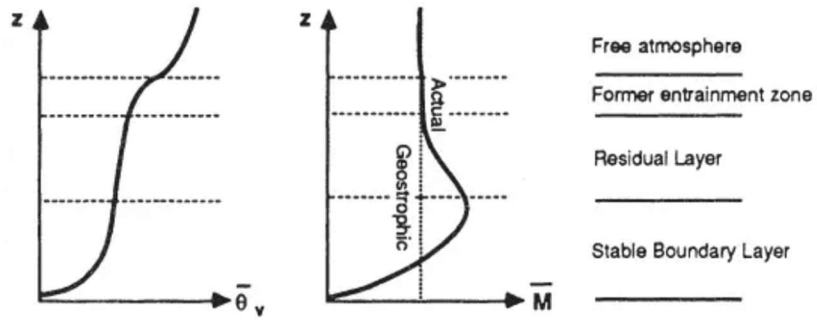


Figure 1: Temperature and Velocity profiles of an idealized stable boundary layer, from Stull (1988) [3].

However, during the day, the heating of the Earth surface by the Sun, introduces a heat flux from the ground into the ABL, causing transition to Unstably Stratified BL, illustrated in figure 2.

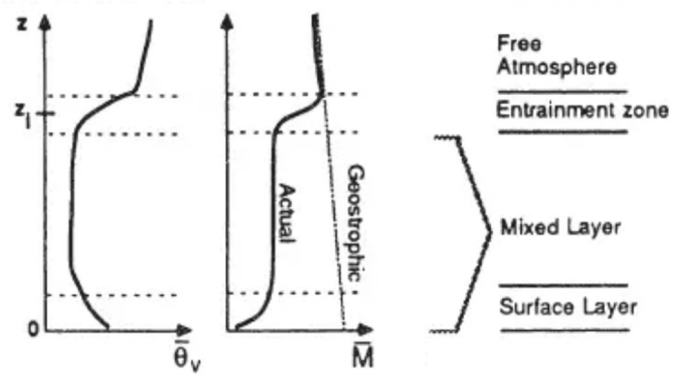


Figure 2: Temperature and Velocity profiles of an idealized unstable boundary layer, adapted from Stull (1988) [3].

The temperature profile of an idealized unstable boundary layer (figure 2) is usually described as being composed of three parts: Surface Layer, Mixed Layer, and Entrainment Zone (Inversion Layer).

The Surface Layer corresponds to what is commonly known as the wall-region in general wall-bounded flows. Above it, lies the Mixed Layer, which is the region where, due to vertical buoyant-mixing, the profile is roughly uniform. This region spans almost the entire boundary layer for strong unstable stratifications ($Ri \ll 0$, large vertical buoyant-mixing), while it becomes really small for weakly unstable stratification situations ($Ri < 0$, but still satisfying: $|Ri| \sim O(1)$). On top, we finally find the Entrainment Zone, also known as the Inversion Layer.

Note that in figures 1 & 2, the temperature profiles are represented in terms of $\bar{\theta}_v$, which stands for the mean virtual potential temperature (or just potential temperature), which is a commonly used quantity in meteorological literature and corrects the temperature accounting for the density change of a gas with height (which is significant for large-scale geophysical flows).

The current research will focus on (weakly) unstable situations, similar to the idealized illustration in figure 2 but, with a much shorter Mixed Layer due to the weak stratification, and therefore, the surface layer would span most of the boundary layer.

1.3 Global Stability of the Atmospheric Boundary Layer

1.3.1 Global Stability

The turbulence structure of the daytime atmospheric boundary layer, and its consequent transport properties, are directly related to the balance between shear- and buoyant-production, which determine the global stability state of the boundary layer. However, the previously introduced definition of the Richardson number, only serves as an indicative for local stability. Therefore, in the literature, the global stability of the daytime ABL capped by an inversion layer at height z_i is usually

parametrized by using what Jayaraman & Brasseur (2021) call the instability parameter [4], defined as: $-z_i/L$, being the stability condition:

$$unstable\ if \qquad -\frac{z_i}{L} > 0$$

Where z_i represents the height of the inversion layer, and L is the Obukhov length-scale, which is described in more detail in the next subsection.

1.3.2 Obukhov Length-Scale

The Obukhov length-scale is defined as:

$$L = -\frac{u_\tau^3}{\kappa\left(\frac{g}{\theta_0}\right)Q_0}$$

Where u_τ is the wall frictional velocity, Q_0 the heat flux from the ground into the ABL, θ_0 the reference potential temperature of the ground, and κ the von Kármán constant.

Similar to the Richardson number, the Obukhov length allows us to distinguish between three cases:

$$for\ L < 0 \rightarrow Unstable$$

$$for\ L > 0 \rightarrow Stable$$

$$for\ L = 0 \rightarrow Neutral$$

Thus, it follows that, at a certain position z along the ABL:

$$if\ z < -L \rightarrow shear\ production\ is\ dominant$$

$$if\ z > -L \rightarrow buoyancy\ production\ is\ dominant$$

From which it can be observed that the flow close to the ground is approximately neutral, and that buoyancy effects only come into play away from the ground [2]. From this observation, it can also be seen that, the Obukhov length-scale represents an order of magnitude estimate for the distance above the ground at which buoyancy production will first overcome shear production [4], and one can clearly understand how the instability parameter $-z_i/L$ characterizes, indeed, the nature of the ABL.

For completeness, we will proceed to use an order-of-magnitude analysis to show how the instability parameter ($-z_i/L$) used by Jayaraman & Brasseur (2021) relates to the (flux) Richardson number definition:

$$Ri = \frac{\frac{g}{\overline{T_0}}\overline{w'\theta'}}{\overline{u'v'}\frac{\partial\overline{u}}{\partial y}} \sim \frac{Buoyant\ turbulence\ production}{Shear\ turbulence\ production}$$

If we apply this to the wall region (which spans most of the BL for weakly unstable stratification conditions), where the shear stress is expected to be constant, and viscous stress negligible:

$$\frac{\tau}{\rho} = -\overline{u'v'} + \nu \underbrace{\frac{\partial \bar{u}}{\partial y}}_{\to 0} = u_\tau^2 \underbrace{\left(1 - \frac{y}{z_i}\right)}_{\sim 1} \to \; -\overline{u'v'} \sim u_\tau^2$$

Using Prandtl's mixing length (l_m) for closure:

$$l_m \sim \kappa y \to eddy\ sizes\ scale\ with\ wall - distance$$

Where κ is the von Kármán constant.

$$-\overline{u'v'} = (K)\frac{\partial \bar{u}}{\partial y} = \left({l_m}^2 \left|\frac{\partial \bar{u}}{\partial y}\right|\right)\frac{\partial \bar{u}}{\partial y} = \kappa^2 y^2 \left|\frac{\partial \bar{u}}{\partial y}\right|\frac{\partial \bar{u}}{\partial y} = u_\tau^2$$

The known logarithmic profile is obtained:

$$\bar{u} = \frac{u_\tau}{\kappa}\ln\left(\frac{y}{y_0}\right), \qquad from\ which\ it\ follows \to \quad \frac{\partial \bar{u}}{\partial y} \sim \frac{u_\tau}{\kappa\, z_i}$$

Moreover, in the log-region, neglecting diffusive heat transfer, one can state:

$$\overline{w'\theta'} \sim Q_0$$

Where Q_0 is the heat flux that the Earth surface provides to the ABL.

Finally, one can show by substitution that the instability parameter ($-z_i/L$) used by Jayaraman & Brasseur corresponds to minus the Richardson number:

$$Ri = \frac{\frac{g}{T_0}\overline{w'\theta'}}{\overline{u'v'}\frac{\partial \bar{u}_i}{\partial x_j}} \sim \frac{\frac{g}{T_0}Q_0}{-u_\tau^2\frac{u_\tau}{\kappa\, z_i}} \sim \frac{z_i}{-\frac{u_\tau^3}{\kappa\left(\frac{g}{T_0}\right)Q_0}} \sim \frac{z_i}{L} \quad \to \quad instability\ parameter = -\frac{z_i}{L} = -Ri$$

1.4 Large-Scale Rolls in Atmospheric Boundary Layers

1.4.1 Introduction to Large-Scale Rolls

One of the most important large-scale atmospheric boundary layer structures when it comes to vertical transport of momentum and scalars (i.e. pollutants) within the ABL, are the so called horizontal convective rolls or large-scale rolls [5]. Large-scale rolls are described by Jayaraman & Brasseur (2021) as being *"turbulent roughly helical motions that span the depth of the boundary layer and are highly elongated in the streamwise direction due to mean shear"* [4]. They can be visualized in satellite pictures by cloud streaks marking the tops of the thermal updraughts (figure 3). A schematic visualization of these organized eddies can be seen in figure 4, which is shown as counter-rotating vortex rolls with axes approximately in the direction of the mean wind.

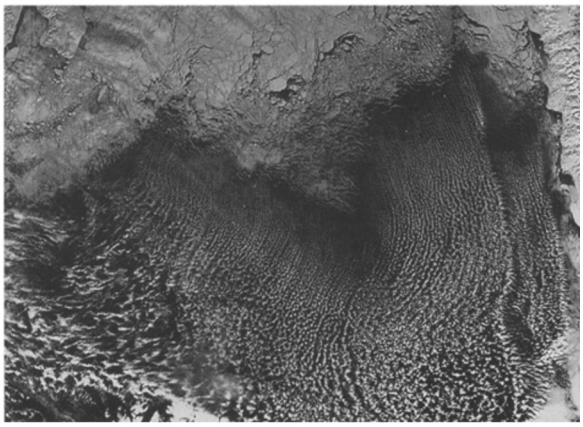


Figure 3: Satellite picture of organized streaky cloud-streets, from Etling & Brown (1993) [5].

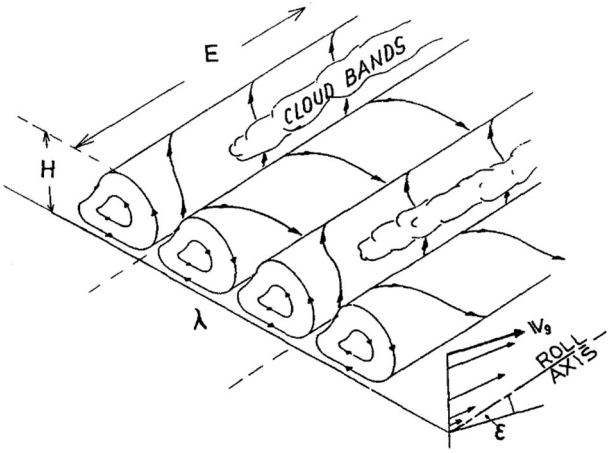


Figure 4: Illustration of the large-scale rolls in the planetary boundary layer, from Etling & Brown (1993) [5].

Many studies have shown that a combination of ground heat flux (i.e. unstable thermal stratification) and mean flow shear is needed for the creation of these structures, therefore: situations of weakly unstable thermal stratification [6].

1.4.2 Insight from studying the Transition from Neutral to Convective

The large-scale structure of the turbulent atmospheric boundary layer (ABL) is directly related to its global stability state, reflecting the balance between shear and buoyancy turbulence production. The dominant energy-containing eddies that make up such large-scale structure are responsible for most of the turbulent transport, and therefore, such large-scale structure has a direct impact on the mixing and the dispersion of pollutants within the ABL. In this regard, a series of works by Jayaraman & Brasseur [4], [7]–[9] studied the transition of the large-scale structure of the ABL from neutral (only shear-production of turbulence) to convective (dominated by buoyancy-production).

Jayaraman & Brasseur (2021) [4] considered the fully developed daytime ABL capped by an inversion layer at height z_i in regions where the boundary layer can be approximated as statistically homogeneous in the horizontal direction and as being in quasi-stationary equilibrium. Under these conditions, the statistical turbulence structure of the ABL depends on the previously introduced instability parameter: $-z_i/L$.

In a daytime unstable ($L < 0$) ABL, where both shear and buoyant production are present, the instability parameter $-z_i/L > 0$ allows us to distinguish between two limit behaviours:

Neutral limit: $-\frac{z_i}{L} \to 0$; $(-L \gg z_i)$

In the neutral limit, mean-shear is the only source of turbulence production, and it is forced by horizontal winds in the free atmosphere. The large-scale structure of such a shear-driven turbulent boundary layer, sketched in figures 5 & 6, is characterized by the presence of small-

and large-scale hairpin packets around coherent low-speed elongated-regions oriented in the direction of the mean flow with a spacing and size scaling with the boundary layer thickness (z_i) (Khanna & Brasseur 1998), (Adrian, 2007) [7], [10].

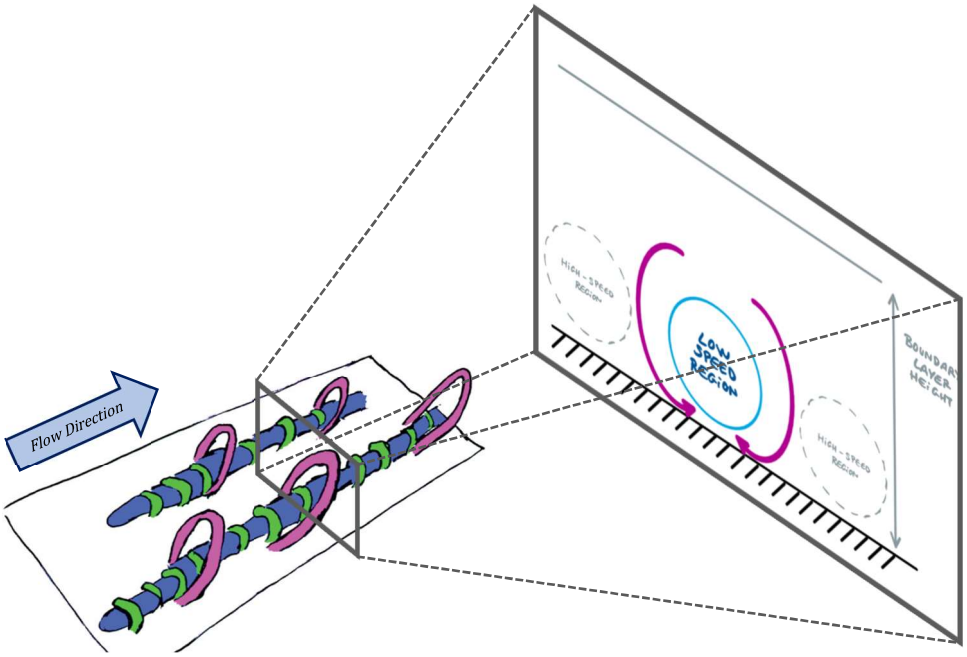


Figure 5: Sketch illustrating the elongated streamwise structures characteristic of isothermal turbulent boundary layers consisting of small- and large-scale hairpin packets (green and purple, respectively) around the low-speed regions (blue). Sketch adapted from Elsinga et al. (2010) [11].

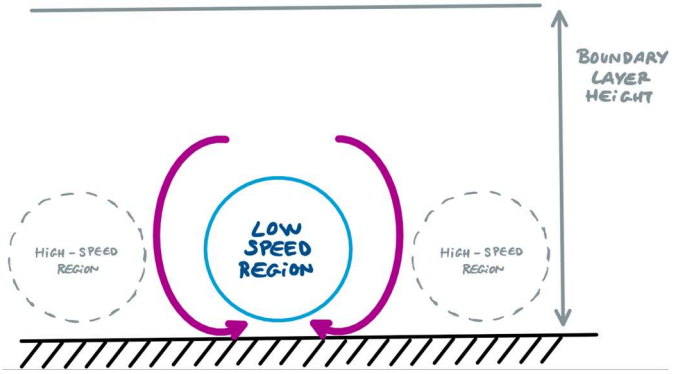


Figure 6: Sketch illustrating a cross-section of the large-scale structure of an isothermal turbulent boundary layer. The large-scale hairpin packets (purple) effectively generate counter-rotating vortices that scale with the boundary layer height.

Fully convectice limit: $-\frac{z_i}{L} \gg 1 \quad or \quad -\frac{z_i}{L} \to \infty\,; \qquad (-L \ll z_i)$

In the fully convective limit, buoyancy dominates turbulence production throughout the ABL, and the buoyancy-driven turbulence fluctuations of vertical velocity are organized as coherent updraughts creating turbulent Rayleigh-Bénard cells [4].

In between these two limits, shear and buoyancy production coexist in what is known as the ***Moderately convective BL***, which takes place in the weak instability range $-z_i/L \sim O(1-10)$.

In this situation, as described by Jayaraman & Brasseur (2021) [4], [7], thermal updraughts emanate from shear-driven low-speed streaks that localize buoyancy force by accumulating high temperature fluctuations. Therefore, the low-speed streaks and the thermal updraughts become spatially linked producing, as a consequence of the combined effect of shear and buoyancy, stronger coherent updraughts that trigger the large-scale rolls introduced in section 1.4.1.

Large-scale rolls are part of a multi-scale process in the ABL which can be roughly summarized as (figure 7): small-scale buoyancy-induced thermal plumes being collected in large-scale low-speed streaks, by large-scale hairpin packets, creating streamwise coherent sheets of warm upward-moving fluid (thermal updraughts) that, when reaching the capping inversion, roll back forming the downward legs of the large-scale horizontal rolls.

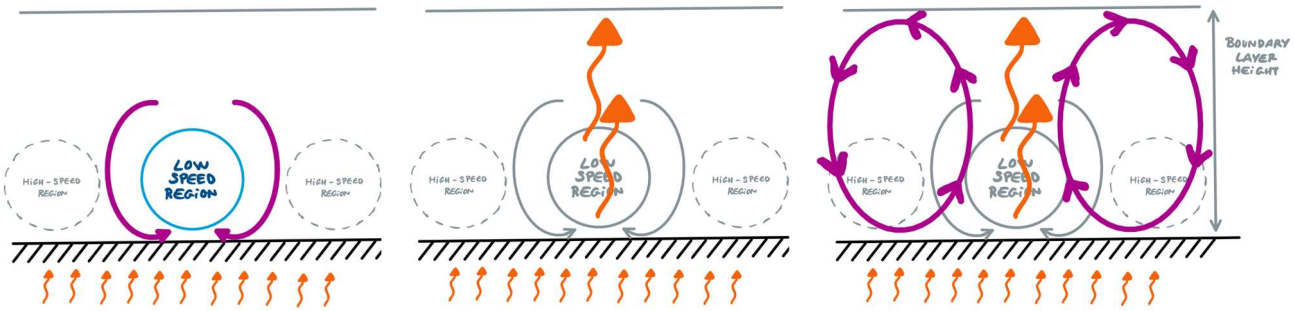


Figure 7: Sketch illustrating the multi-scale process by which shear-driven large-scale counter-rotating vortices (large-scale hairpin packets) become strengthened by collecting small-scale thermal plumes eventually generating large-scale rolls that span the entire boundary layer height.

With the focus on these large-scale rolls, Jayaraman & Brasseur (2021) [4] performed LES simulations of the ABL for different stratification conditions from neutral to moderately convective, finding an interesting non-monotonic behaviour of the coherence lengths, representing the large-scale rolls, to a systematic (weak) increase on unstable stratification.

Figure 8 shows, for different stability states, the contours of the *x*-component of velocity on the $z/z_i = 0.1$ plane (which allows us to visualize in dark blue the coherent low-speed streaks generated by mean shear rate), superimposed on a single isosurface of vertical velocity (which identifies the regions with strong buoyancy-driven updraughts). As observed by Jayaraman & Brasseur (2021) [4], those results show the spatial link between shear-induced low-speed streaks and buoyancy-induced updraughts, and how the structure evolves for different stability states, from neutral to moderately convective.

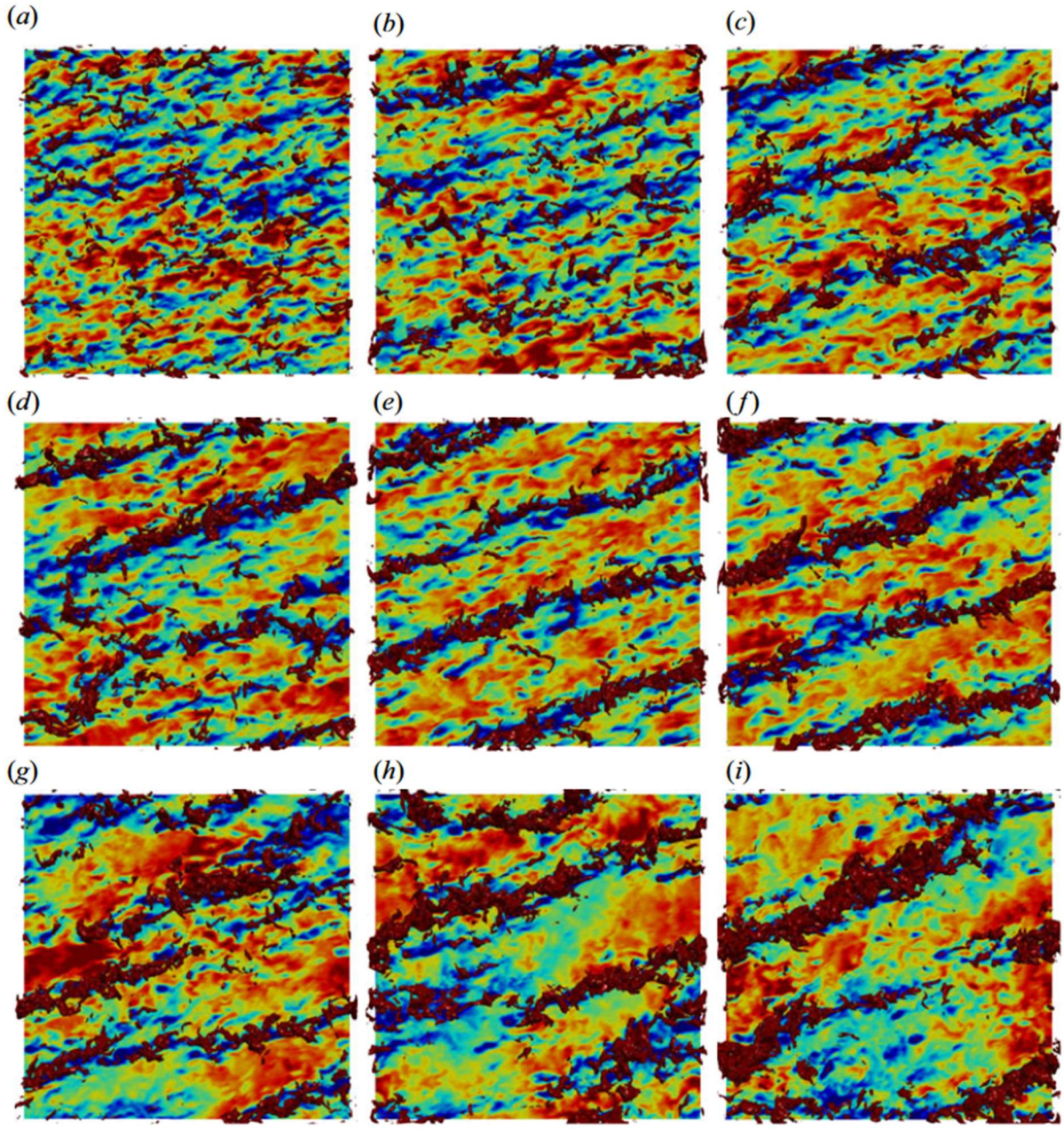


Figure 8: Visualization of the results from Jayaraman & Brasseur (2021). Contours of x-component velocity on the $z/z_i = 0.1$ plane superimposed to a single iso-surface (dark red) of vertical velocity for different stability states: (a) $-z_i/L = 0$; (b) $-z_i/L = 0.304$; (c) $-z_i/L = 0.433$; (d) $-z_i/L = 0.744$; (e) $-z_i/L = 0.916$; (f) $-z_i/L = 1.08$; (g) $-z_i/L = 1.42$; (h) $-z_i/L = 2.86$; (i) $-z_i/L = 3.84$.

Studying the transition from neutral to convective states, Jayaraman & Brasseur (2021) were able to observe a non-monotonic behaviour of the coherence lengths as the degree of instability increased, showing that there is a certain range of weakly unstable stratification conditions in which the coherence lengths of the structures are increased for increasing stratification, meaning that the large-scale rolls were becoming stronger and more prominent [4]. In particular, it was found that the maximally coherent roll state was found for an instability parameter $-z_i/L = 1.08$, which can be seen in figure 8 (f), and would correspond to a $Ri = -1.08$, as proved in section 1.3.2.

This observation could, at a first glance, seem unintuitive. One would expect unstable stratification to enhance vertical mixing and reduce the coherency of the streamwise structures. However, the reason for this increase in coherence length of streamwise structures for increasing unstable stratification (for a certain range) seems to lie in the nature of the previously described mechanism for large-scale rolls formation, where hairpin packets collect small-scale plumes generating concentrated updraughts that make the streamwise coherent structures stronger and more prominent.

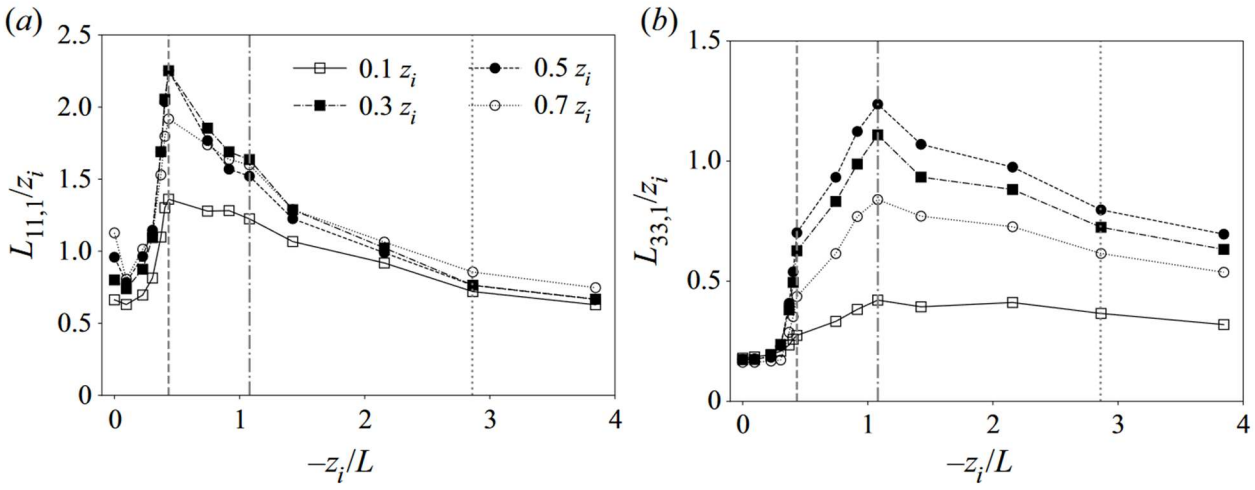


Figure 9: Non-monotonic variation of streamwise coherence lengths for increasing (in)stability parameter -z_i/L, from Jayaraman & Brasseur (2021).

Figure 9, shows the non-monotonic behaviour that Jayaraman & Brasseur (2021) observed for the horizontal coherence lengths representing those streamwise-elongated large-scale rolls [4]. One can clearly see that there is a range of weak unstable stratification where the buoyancy effects are increasing the coherence lengths instead of reducing them. After this small region, then the expected reduction in horizontal coherent lengths is observed.

Now that the large-scale rolls and the findings by Jayaraman & Brasseur (2021) have been presented, the purpose of the present research can be introduced.

1.5 Purpose, Research Questions and Methodology

A high-rise building in an urban environment can be roughly modelled as a surface-mounted cube. In this regard, figure 10 shows an schematic representation of the flow structures around a surface-mounted cube from Martinuzzi & Tropea (1993) [12].

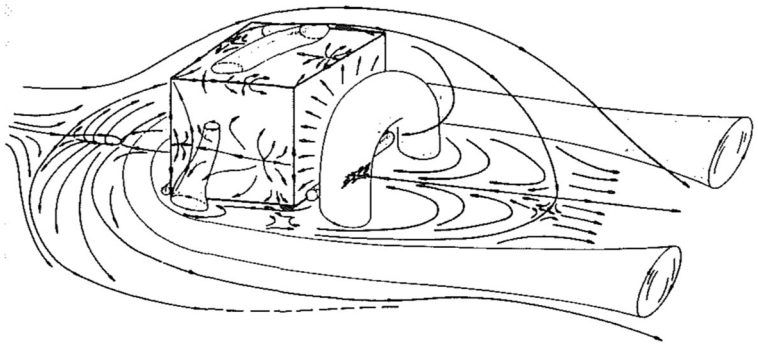


Figure 10: Schematic representation of the flow around a surface-mounted cube, from Martinuzzi & Tropea (1993) [12].

One can note that the roll structures in the far wake of the cube (rightmost part of figure 10) are counter-rotating vortical structures that look quite similar to the large-scale structures of the turbulent boundary layer, the only difference being that the rolls behind the cube are a mean-flow feature. However, the fact that those counter-rotating rolls are a mean-flow feature does not prevent them from strengthening themselves by the same mechanism as seen for the large-scale structures of the turbulent boundary layer. Therefore, the purpose of this research consists on studying whether these roll structures produced by the flow past a high-rise building can show a similar behaviour as the one observed by Jayaraman & Brasseur (2021) for the atmospheric large-scale rolls [4]. Meaning, to study if there will be a certain range of weak unstable stratification conditions at which those rolls strengthen themselves by collecting small-scale plumes and end up becoming more prominent.

The present research work will aim to answer the following questions:

1) Is there a range of weak unstable stratification conditions for which the rolls behind a high-rise building could strengthen themselves by collecting small-scale plumes in a similar way as observed in the formation of the large-scale atmospheric rolls?

2) If so, what would the effects be on pollutant dispersion in urban environments?

In order to find answers to our research questions, the present research work will conduct Large Eddy Simulations (LES) of the flow past a high-rise building for different stratification conditions.

The simulations will be carried out using the open source spectral element method (SEM) code Nek5000-V19. The code and the user defined settings will be validated simulating the canonical turbulent channel flow (TCF) and comparing against commonly used references, such as Kim, Moin & Moser (1987) [13]; Moser, Kim & Mansour (1999) [14]; and Lee & Moser (2015) [15], as well as simulating a non-isothermal turbulent channel flow and comparing against Pirozzoli et al. (2017) [16]. Moreover, a second validation case will be performed by reproducing the results of a recent accurate DNS work that simulated turbulent flow past a wall-mounted cube by Haering et al. (2021) [17].

Finally, after a very complete validation work, we will proceed to study the rolls downstream of the wake of the cube and their behaviour for different weak unstable thermal stratification conditions.

Chapter 2

The Scales of Turbulence

In the same way that one cannot measure the diameter of a needle using a tape measure, we cannot simulate properly a turbulent flow if our numerical model is not able to resolve the smaller and larger structures, as well as the shorter and longer lasting ones. We refer to those features as the length- and time-scales, respectively, and they are a key concept that needs to be understood when simulating turbulent flows.

A turbulent flow is a multiscale process with a wide range of time- and length- scales that depend on the physics of the flow. In our attempt to reproduce the reality via a discrete mesh, our grid resolution determines which scales are being represented and which ones are not. Therefore, a careful selection of the grid spacing (as well as time step) has to be done to ensure that we resolve properly the phenomena we are interested in.

Despite the fact that, as introduced in section 1.5, the present work will perform Large Eddy Simulations (LES), meaning only the large scales of the flow are resolved while the effects of the smallest scales are modelled, when working with turbulence it is always insightful to be aware of its wide range of scales. To that end, this section will provide a brief introduction of these scales, which will be used in the following chapters to assess the quality of our LES setup, as well as, to understand the mesh resolution requirements and illustrate how far from fully-resolved turbulence will our simulations be, providing useful information for the interpretation of our LES results.

2.1 Length Scales

The Kolmogorov length-scale was usually considered to be the smallest length-scale that has to be resolved on a computational mesh aiming to fully-resolve turbulence (DNS):

$$Kolmogorov\ length\ scale \rightarrow \ \eta = \left(\frac{\nu^3}{\epsilon}\right)^{1/4}$$

However, Moin & Mahesh (1998) [18] analysed different spectral DNS works whose results reached a very good agreement with experiments despite the fact that their mesh resolutions were larger than the Kolmogorov scale, concluding that the requirement of resolving up to Kolmogorov length-scale may actually be too strict. Figure 11 from Moin & Mahesh (1998) collects the resolutions used in several spectral DNS simulations in terms of Kolmogorov units, where one can see that those highly respected DNS simulations were using resolutions slightly larger than the Kolmogorov length-scale.

Flow	Resolution in η
Curved channel (MM)	$\Delta z = 3.75,\ \Delta r = 0.13,\ r_c\,\Delta\theta = 11.25$
Plane channel (KMM)	$\Delta x = 7.5,\ \Delta y = 0.03,\ \Delta z = 4.4$
Boundary layer (S)	$\Delta x = 14.3,\ \Delta y = 0.33,\ \Delta z = 4.8$
Homogeneous shear (RMR)	$\Delta x = 7.8,\ \Delta y = 3.9,\ \Delta z = 3.9$
Isotropic turbulence (W)	$\Delta x = 4.5,\ \Delta y = 4.5,\ \Delta z = 4.5$

[a]MM, KMM, S, RMR, and W denote Moser & Moin 1987, Kim et al 1987, Spalart 1988 ($R_\theta = 1410$), Rogers et al 1986 (Run C128U), and Wray's (AA Wray, unpublished information) DNS of Comte-Bellot & Corrsin's (1971) experiment, respectively.

Figure 11: Table from Moin & Mahesh (1998) showing the grid resolution in Kolmogorov length-scales used in different spectral DNS.

Based on this observation, they argued that the smallest length-scale that has to be resolved depends on the energy spectrum, and is typically larger than the Kolmogorov length-scale. They concluded that the actual requirement for accurate DNS simulations was to ensure that the computational mesh resolves the scales where most of the dissipation occurs. Therefore, the smallest resolved length-scale is required to be of the order of the Kolmogorov length-scale, but not necessary equal to it [18].

For instance, the work by Moser & Moin (1987) [19] showed that most of the dissipation in a curved channel occurs at scales greater than $15\,\eta$. Which leads to the conclusion that, for the specific case of the curved channel flow, ensuring that the mesh resolves at least $15\,\eta$ could be enough to get DNS-like-accurate results [18]. This point will be used in upcoming sections to claim that it is reasonable to assume that an LES simulation resolving around $15\,\eta$ can be considered a very accurate LES, whose results are expected to be very close to an actual DNS.

Finally, for the interpretation of the results from the upcoming sections, it is interesting to introduce the ratio of the Kolmogorov scales to the scales of the macro-structure, which is often known as the scale separation. Using the Reynolds number definition, one can write the ratio of Kolmogorov scales to scales of macro-structure, i.e. integral length scale (L) as:

$$\frac{L}{\eta} \sim Re^{3/4}$$

Where: $Re = \frac{UL}{\nu}$

2.2 Time Scales

In order to fully resolve the turbulence, i.e. doing DNS, one needs to take into consideration the time scales too. The smallest time-scale in turbulence is the Kolmogorov time-scale which is defined as:

$$Kolmogorov\ time\ scale \rightarrow \tau = \left(\frac{\nu}{\varepsilon}\right)^{1/2}$$

The scale separation concept introduced in section 2.1 applies to time-scales too, however, from the ratio of the Kolmogorov time-scale to the integral time-scale (T) we find a different scaling with the Reynolds number:

$$\frac{T}{\tau} \sim Re^{1/2}$$

This means that for increasing Reynolds numbers, the Kolmogorov length-scale becomes smaller significantly faster than the Kolmogorov time-scale. Therefore, despite the fact that when doing a DNS one has to ensure that the Kolmogorov time-scale is resolved, it is usually the Kolmogorov length-scale the critical one, which is the reason why usually more attention is paid to the length-scales.

Chapter 3

Nek5000 Solver

3.1 Spectral Element Methods

The spatial discretization used in NEK5000 is based on the spectral element method (SEM) that was introduced by Patera (1984) [20], where he proposed a combination of the generality of the finite element method (FEM), together with the accuracy of spectral techniques, for the solution of the incompressible Navier-Stokes equations.

This combination, also called by him: hybrid finite element-spectral method, was intended to exploit the accuracy of spectral techniques while bypassing their main drawback: the potentially extremely difficult implementation for general complex flow geometries. It is also relevant to mention, that a second drawback of spectral techniques was also overcome, namely the fact that spectral methods require periodicity in the flow direction, which was no longer a condition for SEM.

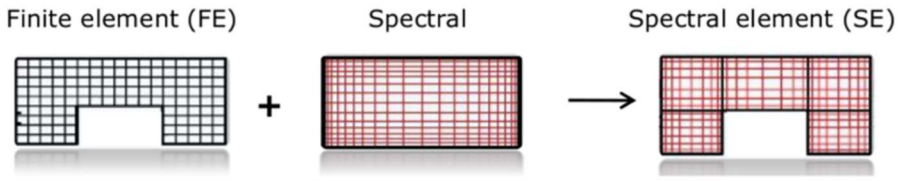


Figure 12: Illustration of the combination of spectral techniques and finite elements, from Prasad (2016) [21].

As shown in figure 12, in the spectral element method the domain is discretised into a series of elements, just like in the finite element method. However, the flow variables are represented using, as local basis functions, high-order Lagrangian interpolant polynomials on a Gauss-Lobatto-Legendre (GLL) point distribution within each element. Figure 13 exemplifies some basis functions for different polynomial orders.

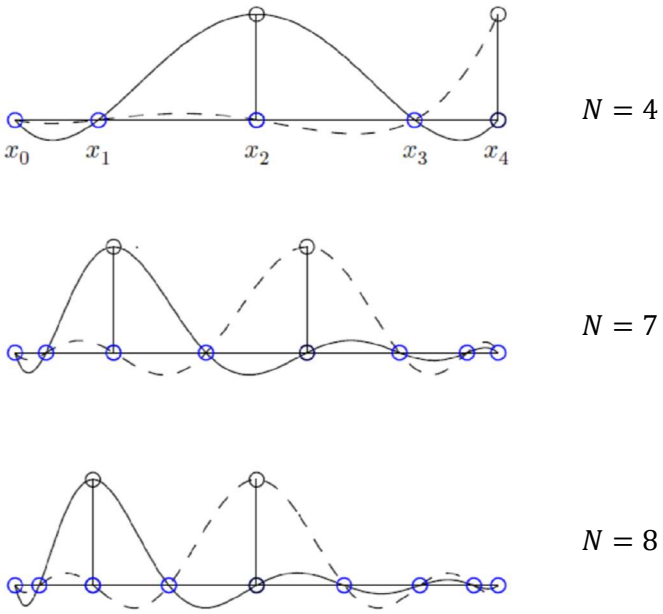


Figure 13: Lagrangian polynomial basis functions for different GLL collocation points. Adapted from Prasad (2016) [21].

In addition to the already stated higher-order accuracy of the spectral element method, among their advantages one can mention its very small numerical dispersion and dissipation, which makes it ideal for stability calculations, turbulence transition and intermittency, long time integrations, and high-turbulence-intensity flows. Moreover, SEM computational error decays exponentially with increasing Lagrange polynomial order, allowing for faster convergence than FEM with less degrees of freedom, which in turn means less computational cost. Finally, one of the main strengths of the spectral element code Nek5000 is its excellent scalability.

For further details on the NEK5000 solver, refer to Deville et al. (2002) [22].

3.2 Governing Equations

Nek5000 spectrally solves the Incompressible Navier-Stokes Equations, namely mass and momentum conservation equations (written below for constant fluid viscosity):

$$\nabla \cdot \boldsymbol{u} = 0$$

$$\rho\left(\frac{\partial \boldsymbol{u}}{\partial t} + \boldsymbol{u} \cdot \nabla \boldsymbol{u}\right) = -\nabla p + \mu \nabla^2 \boldsymbol{u} + \rho \boldsymbol{f}$$

Which, in nondimensional form reads as:

$$\frac{\partial \boldsymbol{u}^*}{\partial t^*} + \boldsymbol{u}^* \cdot \nabla \boldsymbol{u}^* = -\nabla p^* + \frac{1}{Re} \nabla^2 \boldsymbol{u}^* + \boldsymbol{f}^*$$

Where: $Re = \frac{\rho U L}{\mu}$ (Reynolds number)

Moreover, when solving for temperature, the energy equation comes into play governing convective and conductive heat transfer, as well as heat sources or sinks:

$$\rho c_p \left(\frac{\partial T}{\partial t} + \boldsymbol{u} \cdot \nabla T \right) = \nabla \cdot (\lambda \nabla T) + q'''$$

Where: $\lambda \rightarrow thermal\ conductivity$ $q''' \rightarrow volumetric\ heat\ source$

Which, in nondimensional form reads as:

$$\frac{\partial T^*}{\partial t^*} + \boldsymbol{u}^* \cdot \nabla T^* = \frac{1}{Pe} \nabla^2 T + q'''^*$$

Where: $Pe = \frac{LU}{\alpha}$ (Peclet number) $\alpha = \frac{\lambda}{\rho c_p}$ (Thermal diffusivity)

3.3 Sub-Grid Scale Modelling

Nek5000 offers two stabilization filtering options which are intended to drain energy at the smallest wavelengths providing the required sub-grid scale dissipation, also providing a stabilization mechanism when all scales of the flow are being resolved.

On one hand, their built in Explicit Filter is based on the method described in Fischer & Mullen (2001) [23]. In short, this stabilization filter applies a low-pass filtering operation after every time step, which explicitly filters the solution and drains energy from the small wavelengths acting as a sub-grid scale dissipation model for our Large Eddy Simulation.

On the other hand, the user can also use the built in *High-Pass Filter (hpfrt)*, which is based on the method by Stolz et al. (2005) [24]. In this method, a convolution operator representing a low-pass filtering is used.

$$\widetilde{\boldsymbol{u}} = G \cdot \boldsymbol{u}$$

$$where: \quad \begin{matrix} G \rightarrow filter\ kernel \\ \widetilde{\boldsymbol{u}} \rightarrow low-pass\ filtered \\ \boldsymbol{u} \rightarrow original\ signal \end{matrix}$$

Subsequently, a high-pass filter is constructed from the difference between the original, $\boldsymbol{u}$, and the low-pass filtered, $\widetilde{\boldsymbol{u}}$, signals, and weighted by a constant χ:

$$\chi(\boldsymbol{u} - \widetilde{\boldsymbol{u}})$$

Finally, this term is subtracted from the RHS of the momentum and energy equations, providing the required energy drain for our Large Eddy Simulation:

$$\frac{\partial \boldsymbol{u}}{\partial t} + \boldsymbol{u} \cdot \nabla \boldsymbol{u} = -\nabla p + \frac{1}{Re}\nabla^2 \boldsymbol{u} - \chi(\boldsymbol{u} - G \cdot \boldsymbol{u})$$

$$\frac{\partial T}{\partial t} + \boldsymbol{u} \cdot \nabla T = \frac{1}{Pe}\nabla^2 T - \chi(T - G \cdot T)$$

In both cases, the user can tune the filter *cut-off ratio*, which controls which of the highest modes will be affected by the filter, and the *filter weight*, which controls its strength.

Chapter 4

Turbulent Channel Flow Validation

Prior to an actual simulation, a validation stage is required. This stage is intended to test the solver and the used settings, validating the results against trusted data from literature, in order to gain confidence on the numerical model's adequacy. In this regard, a series of three validation cases has been designed so that they provide validation for all the phenomena present in the actual case that we aim to simulate: a surface-mounted cube subject to weakly unstable thermal stratification.

The first validation case will consist of the canonical turbulent channel flow, which is an ideal starting point due to its geometrical simplicity that allows for fast and easy-to-set up simulations. Secondly, a step further will be taken by simulating a non-isothermal turbulent channel flow at different unstable thermal stratification conditions. Finally, the isothermal turbulent flow past a surface-mounted cube will provide the last validation stage, while allowing us to validate the computational mesh that will be used in our cases of study.

Once these validation cases have been successfully conducted, we will be able to proceed with the simulation of the study cases that will allow us to asses our research questions.

4.1 Isothermal Turbulent Channel Flow

4.1.1 Introduction

The easiest wall-bounded turbulent flow to simulate is the turbulent channel flow (TCF) being, therefore, widely documented in the state of the art. Moreover, such a flow case is also of important relevance for our work since, as it will be described in Chapter 6, a concurrent simulation of a turbulent channel flow will be used to generate the turbulent inflow for our final cases of study. For these

reasons, the simulation of this canonical flow will be used to become familiar with turbulent flow simulations with Nek5000, and the key aspects to bear in mind when simulating such a multiscale phenomenon. Figure 14 shows the sketch of the flow geometry of a turbulent channel flow.

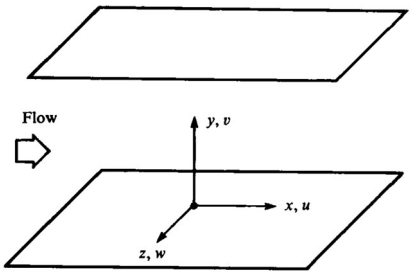


Figure 14: Sketch of the flow geometry of a turbulent channel flow, from Kim, Moin & Moser (1987).

Several highly citated works have been conducted on the TCF, such as the early DNS work by Kim, Moin & Moser (1987) [13] at low Reynolds number ($Re_\tau = 180$), or the more recent DNS work by Lee & Moser (2015) [15], reaching up to $Re_\tau = 5200$.

As commonly used when analysing TCF, the definitions of the frictional velocity (u_τ) and viscous length-scale (δ_v) are introduced:

$$u_\tau = \sqrt{\frac{\tau_{wall}}{\rho}} \qquad ; \qquad \delta_v = \nu \sqrt{\frac{\rho}{\tau_{wall}}} = \frac{\nu}{u_\tau}$$

The introduced viscous scales allow to present the results in dimensionless manner by using the so-called wall-units: u^+, y^+.

$$u^+ = \frac{\bar{u}}{u_\tau} \qquad ; \qquad y^+ = \frac{y}{\delta_v} = \frac{y}{\nu / u_\tau}$$

Furthermore, the so-called frictional Reynolds number (Re_τ) can be defined as:

$$Re_\tau = \frac{u_\tau \, h}{\nu} = \frac{h}{\delta_v}$$

Where h is the half-channel height.

The characteristic features of a TCF can be seen in figures 15 & 16, which show the mean-velocity profile and the root-mean-square velocity fluctuations from Kim, Moin & Moser (1987). The horizontal axis representing wall-normal distance, is expressed in terms of y^+, i.e. normalized by the viscous

length-scale (δ_v). While the mean-velocity ($\bar{u}$), and its variance ($\overline{u_i' u_i'}$), are normalized using the frictional velocity (u_τ), and the frictional velocity squared ($u_\tau{}^2$), respectively.

$$u^+ = \frac{\bar{u}}{u_\tau} \qquad u_{rms} = \frac{\overline{u'u'}}{u_\tau{}^2} \qquad v_{rms} = \frac{\overline{v'v'}}{u_\tau{}^2} \qquad w_{rms} = \frac{\overline{w'w'}}{u_\tau{}^2}$$

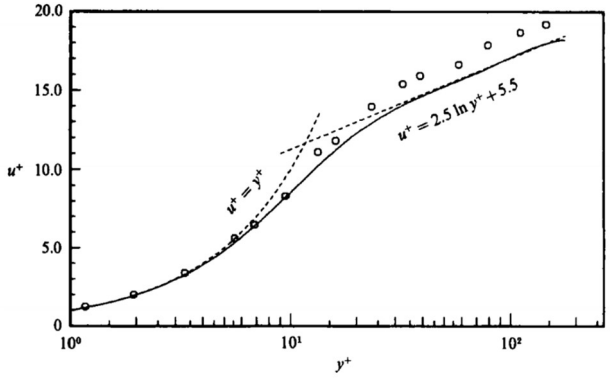


Figure 15: Mean-velocity profile of a TCF, from Kim, Moin & Moser (1987).

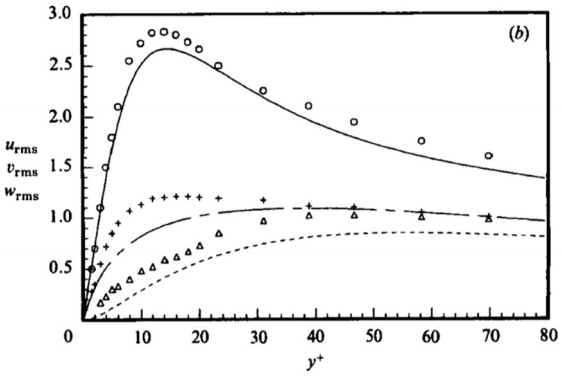


Figure 16: Root-mean-square velocity fluctuations of a TCF, from Kim, Moin & Moser (1987).

For this validation stage, the results from Lee & Moser (2015) [15] for the turbulent channel flow at $Re_\tau = 544$, are taken as reference. Such value of Re_τ is achieved by imposing a $Re_{bulk} = \frac{(2h)u_b}{\nu} = 20000$, as reported by Lee & Moser (2015), where for convenience: the bulk velocity, $u_b = 1$, and the half-channel height, $h = 1$.

4.1.2 Governing Equations

As introduced in section 3.2, Nek5000 spectrally solves the Conservative Form of the Incompressible Navier-Stokes Equations (Momentum and Mass conservation), for constant fluid viscosity and density:

$$\nabla \cdot \boldsymbol{u} = 0$$

$$\rho\left(\frac{\partial \boldsymbol{u}}{\partial t} + \nabla \cdot (\boldsymbol{u}\boldsymbol{u})\right) = -\nabla p + \mu \nabla^2 \boldsymbol{u}$$

Finally, the energy drain to model sub-grid scales dissipation is achieved by applying the Explicit Filter [23] introduced in section 3.3.

4.1.3 Geometry Domain

The main reason why a turbulent channel flow is the easiest-to-simulate wall-bounded turbulent flow is the fact that, with the proper choice of the domain size, we are allowed to use periodic boundary conditions along the two statistically homogenoeus directions (streamwise and spanwise).

The reason why the size of the domain is that important lies on the multiscale nature of turbulence. This needed size is determined by the distance along which the turbulence is no longer correlated, and it is usually known as the minimal flow unit. By making sure that the turbulence is not correlated between domain boundaries, we are effectively making sure that our computational domain is not constraining the large-scale structures of the flow. Figure 17, from Kim, Moin & Moser (1987), shows two-point correlation results along streamwise and spanwise directions for a turbulent channel flow, which allow us to estimate the required domain size based on the needed distance downstream (and spanwise) for which the two-point correlations vanish.

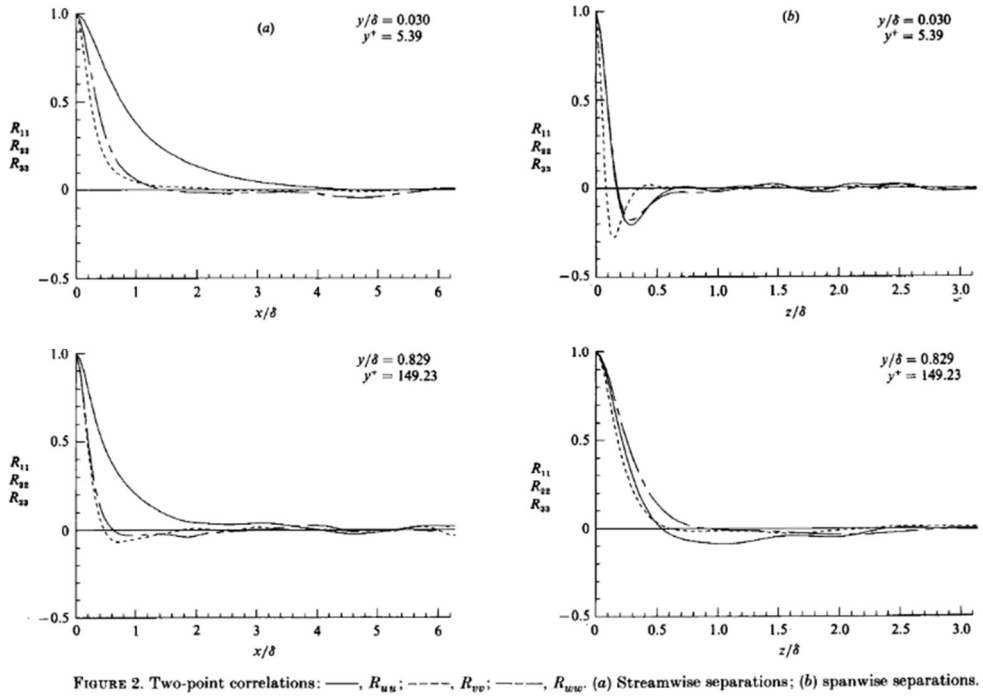


FIGURE 2. Two-point correlations: ——, R_{uu}; – – – –, R_{vv}; — — —, R_{ww}. (a) Streamwise separations; (b) spanwise separations.

Figure 17: Two-point correlations from Kim, Moin & Moser (1987) [13]. In this figure: $\delta = h =$ half-channel height.

Many highly citated works in the field, such as the work by Kim, Moin & Moser (1987) [13], used $L_x = 4\pi h$ - where $h = 1$ is the half channel height - for the streamwise direction, and $L_z = 2\pi h$ for the spanwise direction. However, looking at figure 17, it is clear that at distances $L_x = 2\pi h$ and $L_z = \pi h$, the two-point correlations are already virtually zero. Meaning that such domain size would already ensure that the turbulence is uncorrelated across pairs of periodic domain boundaries. This has been tested in detail by Prasad 2016 [21], validating that the later domain sizes ($L_x = 2\pi h$ and $L_z = \pi h$) yield to the same results as the larger domains. Based on this, the current work will use these domain sizes in the turbulent channel flow simulation, which will imply a significant computational cost reduction while still providing accurate results.

4.1.4 Fully-Resolved Turbulent Channel Flow

While setting up any CFD simulation, one has to make sure that the used discretization of the domain is adequate to capture the physics. As introduced in Chapter 2, the relevant length-scale for determining the needed mesh resolution is the Kolmogorov length-scale, meaning no insightful discussion about mesh resolution for simulating turbulence can be made without discussing how small those small scales are. Despite the fact that this work will not be resolving all the scales of turbulence, it is interesting to discuss how would a DNS resolution look like so that we know how our LES-resolution relates to that of fully-resolved turbulence. To that end, in this section we will use state of the art data to estimate the order of magnitude of the Kolmogorov length-scales for our channel simulations, as well as present commonly used DNS-resolutions in literature.

First of all, the work by Kim, Moin & Moser (1987) reported for $Re_\tau = 180$ a channel-height-averaged Kolmogorov length-scale of around ~ 2 wall-units [13]. Moreover, the work by Morishita et al. (2011) [25] and (2019) [26] provides a reference for the Kolmogorov length-scale obtained from turbulent channel flow DNS results of the average dissipation rate, for different Reynolds numbers. Based on the data reported by Morishita et al. (2019), figure 18 shows the Kolmogorov length-scale (in wall-units) as a function of the normalized wall distance for TCF at different frictional Reynolds numbers.

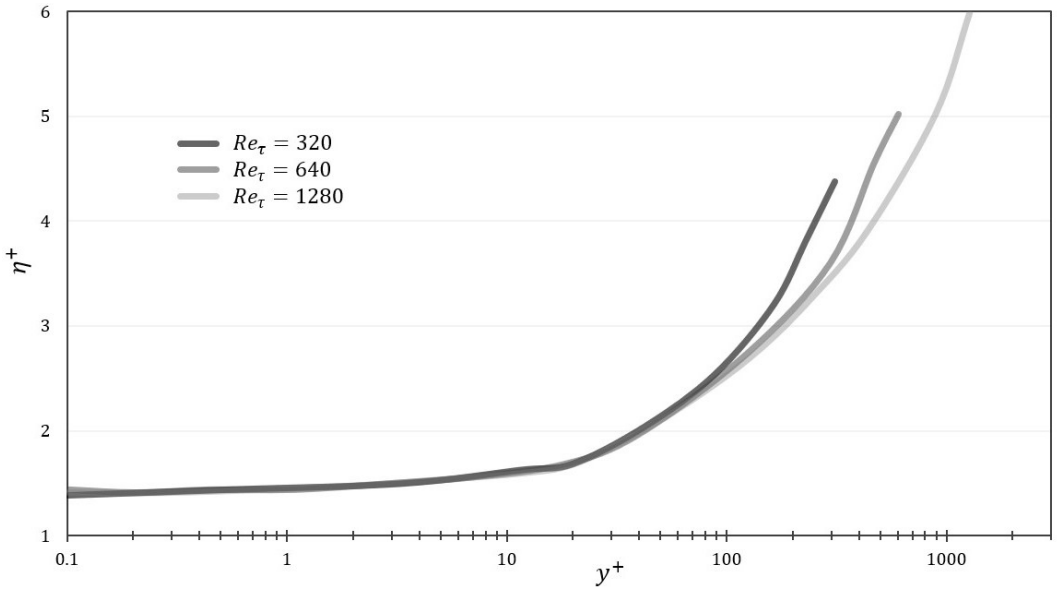


Figure 18: Kolmogorov length-scale (in wall-units) as a function of the normalized wall distance for turbulent channel flow at different frictional Reynolds numbers. Figure made using the data from Morishita et al. (2019) [26].

From figure 18 one can notice that the Kolmogorov length-scale expressed in wall-units (η^+) is a weak function of the Reynolds number. Moreover, the minimum value $\eta^+ \sim 1.5$, which is found in the near-wall region, is virtually independent on the Reynolds number.

Moreover, if we limit ourselves to low Reynolds numbers, there is not a too large variability on the local Kolmogorov length-scale along the wall-normal direction. Therefore, it is reasonable to use the averaged Kolmogorov length-scale across the channel height (η^+_{avg}) as a global estimate for the Kolmogorov length-scale. Table 1 summarizes the values of η^+_{avg} for some frictional Reynolds numbers within the range used in the present thesis ($Re_\tau = 178 - 825$).

Once again, we can point out that, for low Reynolds numbers, the global estimate for the Kolmogorov length-scale (η^+_{avg}) is not a very strong function of the Reynolds number. Furthermore, since η^+_{avg} increases as Re_τ increases, we are in the safe side if we take $\eta^+_{avg} \sim 2$ as the global estimate for the Kolmogorov-length scale within our range of Reynolds numbers.

Re_τ	η^+_{avg}	Source
180	~ 2	*Reported by Kim, Moin & Moser (1987).*
320	~ 3.0	*Computed from the data by Morishita et al. (2011,2019).*
640	~ 3.4	
1280	~ 4.3	

Table 1: Averaged Kolmogorov length-scale across the channel height.

Second of all, regarding commonly used DNS-resolutions in literature, previous turbulent channel flow works such as Moser & Moin (1984) [27] and Kim, Moin & Moser (1987) [13] have proved that resolutions of $\Delta x^+ \approx 12\ (\sim 6\eta)$, $\Delta z^+ \approx 7\ (\sim 3.5\eta)$ and $\Delta y^+_{centerline} \approx 4.4\ (\sim 2.2\eta)$ were enough to resolve the most important turbulent scales, despite being larger than their estimate for the Kolmogorov length-scale (~ 2 wall-units). Moreover, the work by Lee & Moser (2015), which is being used as reference for the present validation chapter, used also similar resolutions as those reported by Kim, Moin & Moser (1987). While further analysis from Jimenez (2003) states a slightly more strict requirement for DNS resolution of the order of $\Delta x^+ \approx 8$, $\Delta z^+ \approx 4$ and $\Delta y^+_{max} \approx 8$ in the centreline of the channel [28].

Note that the previously mentioned resolutions refer to the bulk of the flow only. When it comes to the needed resolution for resolving a boundary layer over a wall, $y^+_{wall} < 1$ is usually used to ensure the presence of at least a few points on the viscous sublayer ($< 5^+$). However, in DNS works, y^+_{wall} is usually brought significantly below the unity, to values around $0.05 - 0.5$ [13], [15].

Having presented an estimate for the Kolmogorov length-scale and the commonly used DNS-resolutions for TCF, the following section will proceed to introduce the resolution guidelines that will be used for all the LES simulations contained in the present thesis.

4.1.5 Domain Discretization - Mesh

The guidelines for well-resolved LES on Nek5000 proposed by Negi et al. [29] will be used throughout the entire project. Those guidelines require:

$$\Delta y_w^+ < 1; \qquad \Delta x^+ < 20; \qquad \Delta z^+ < 9$$

It can be observed that these guidelines are close to the DNS resolutions presented in section 4.1.4, not being even twice as coarse. Moreover, using our estimate for the Kolmogorov length-scale $\eta_{avg}^+ \sim 2$ we can express these resolution guidelines in terms of Kolmogorov-length-scales as:

$$\Delta y_w^+ < 1 \ \ (\sim 0.5\eta) \qquad \Delta x^+ < 20 \ \ (\sim 10\eta) \qquad \Delta z^+ < 9 \ \ (\sim 4.5\eta)$$

At this point, based on Moin & Mahesh (1998) [18] and Moser & Moin (1987) [19] presented in section 2.1, we assume that we can consider our resolution to be enough to guarantee almost DNS-like accuracy if it resolves $\sim 15\eta$, despite the fact that we are not dealing with a curved channel. Therefore, we can claim that the guidelines from Negi et al. [29], that will be used throughout the entire thesis, will ensure that most of the dissipation is resolved and will produce almost DNS-like accuracy.

Finally, the mesh has been generated using the Nek5000 built-in mesh generator (genbox). The mesh follows a uniform distribution in the streamwise (x) and spanwise (z) directions, while an hyperbolic tangent stretching function distributes the points in the wall-normal (y) direction. Table 2 summarizes the main features of the used mesh.

	N_x	N_y	N_z	*wall stretching parameter*	*polynomial order*	Δy_w^+	Δx_{max}^+	Δz_{max}^+	Δy_{max}^+
LES mesh for $Re_\tau = 544$	36	20	32	1.8	7	< 0.82	20.5 ($\sim 10.3\,\eta$)	11.5 ($\sim 5.8\,\eta$)	22.1 ($\sim 11.0\,\eta$)

Table 2: Summary showing mesh resolution, stretching parameter and polynomial order for $Re_\tau = 544$. Nx, Ny, Nz represent number of global mesh elements in each direction. Resolutions in wall-units, together with an estimate in Kolmogorov-length-scale-units using $\eta_{avg}^+ \sim 2$.

4.1.6 Boundary Conditions

As already introduced, boundary conditions for a turbulent channel flow are rather simple. Both the top and the bottom walls are no-penetration and no-slip, while a periodic boundary condition is used along the two statistically homogeneous directions, i.e. x (*inlet*, *outlet*) and z (*sides*) directions.

In order to accelerate flow development, a suitable initial condition has been generated based on the mean flow profile described by the empirical Reichardt function, which approximates properly both, the near-wall and the logarithmic region:

$$u^+ = \frac{1}{\kappa}\ln(1+\kappa y^+) + 7.8\left[1 - e^{\left(-y^+/11\right)} - \frac{y^+}{11}e^{\left(-y^+/3\right)}\right]$$

Where: $u^+ \rightarrow Dimensionless\ velocity$ $y^+ \rightarrow Dimensionless\ wall\ distance$ $\kappa \rightarrow von\ Kármán\ ct. \approx 0.41$

Finally, in order to trigger the transition to turbulence, a sinusoidal perturbation is superimposed to the mean flow profile obtained from the Reichardt function.

4.1.7 Simulation Settings

The work from Mason & Callen [30] provides guidelines for some time considerations for simulating isothermal turbulent channel flows. On one hand, a guideline for the time needed for flow developing is presented. However, since the required time for flow development is highly dependent on the used initial conditions (i.e. we are using a Reichardt's function and superimposing a sinusoidal perturbation to bypass turbulence transition), we decide to assess the flow full development by monitoring the wall-shear stress (τ_{wall}) over time until it stabilizes oscillating around a mean value (figure 19).

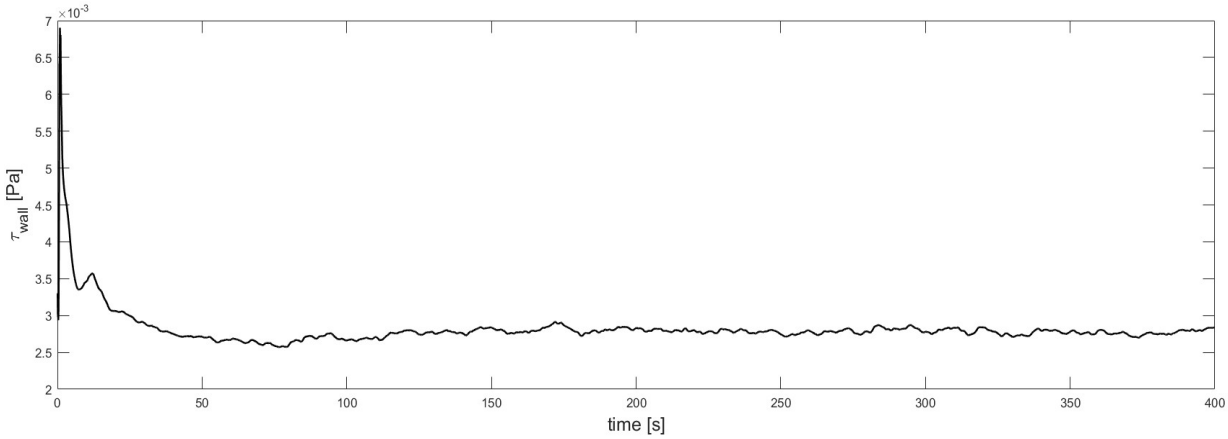


Figure 19: The development of the turbulent channel flow (Re_τ=544) has been verified by monitoring the wall-shear stress evolution over time.

On the other hand, Mason & Callen [30] also presents a criterion to determine an appropriate averaging window for taking flow statistics. Their guideline states that the averaging window should satisfy the following requirement:

$$10\frac{h}{u_\tau}$$

For the given frictional Reynolds number: $Re_\tau = 544 \rightarrow\ u_\tau = 5.43 \cdot 10^{-2}$, therefore:

$$Averaging\ window = \ 10\frac{h}{u_\tau} = 10\frac{1}{5.43 \cdot 10^{-2}} = 184.2\ s$$

Therefore, we conclude that once we have ensured full flow development, an averaging window of 245 seconds will be optimal to capture proper statistics.

Regarding the numerical scheme and running settings, a 2nd order backward differences scheme, together with an operator-integration factor scheme (OIFS) extrapolation, has been used for the time stepping. A time step of $7 \cdot 10^{-3}$ seconds has been used ($CFL = 1.5$), which is within the stable CFL-range of the used scheme [31]. An initial guess was made based on the stability criteria of the used scheme, followed by a time-step independency study, where it has been verified that the solution no longer improves when the time-step is further reduced.

4.1.8 Results and Discussion

From the resulting wall shear stress (τ_{wall}) from our simulation, the corresponding frictional Reynolds number (Re_τ) can be computed.

$$Re_\tau = \frac{u_\tau\, h}{\nu} = \frac{\sqrt{\frac{\tau_{wall}}{\rho}}\ h}{\nu} = 542.7$$

The obtained frictional Reynolds number exhibits a relative discrepancy with respect to the $Re_\tau = 544$ reported on the reference paper, of just 0.24%. This great matching of the shear stress proves an excellent prediction of the interaction between the flow and the walls by our LES simulation.

Regarding the relevant profiles, figures 20 & 21, present the obtained mean velocity profile and the root-mean-square velocity fluctuations, for which the fluctuating quantities have been computed using that for a sufficiently large averaging window on statistically steady state flow field, the average of the fluctuations equals the variance minus the mean squared:

$$\overline{u'u'} = \overline{u\,u} - \bar{u}\,\bar{u}$$

Same for the remaining two components of velocity, however: $\bar{v} = \bar{w} = 0$, due to the flow geometry.

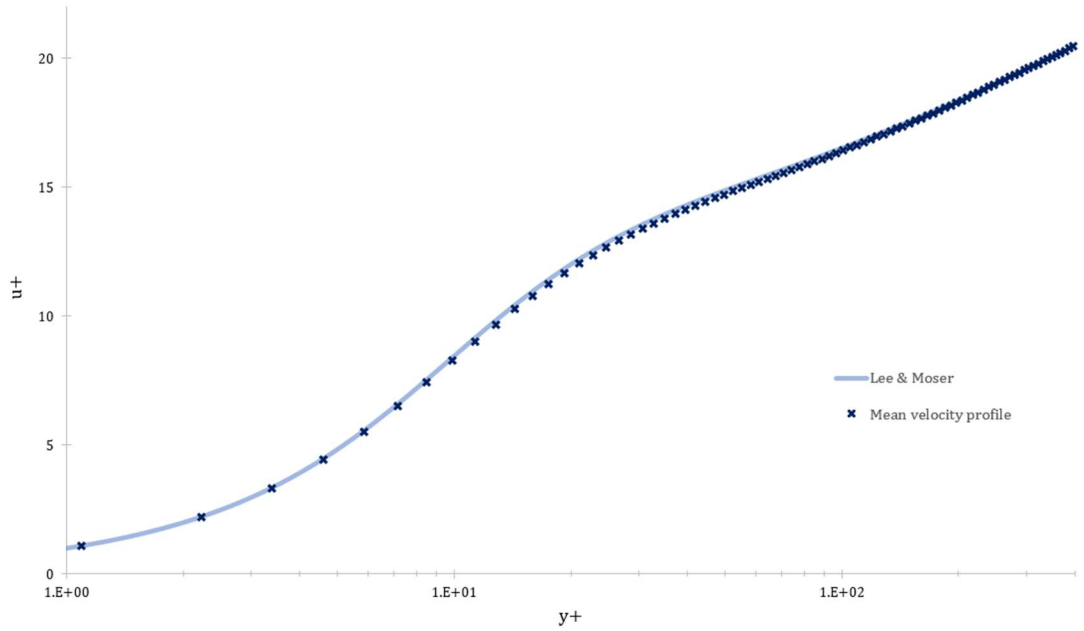


Figure 20: Mean velocity profile in wall units. Thick solid line represents the data from Lee & Moser (2015), while the cross-markers represent the obtained LES results from the present work.

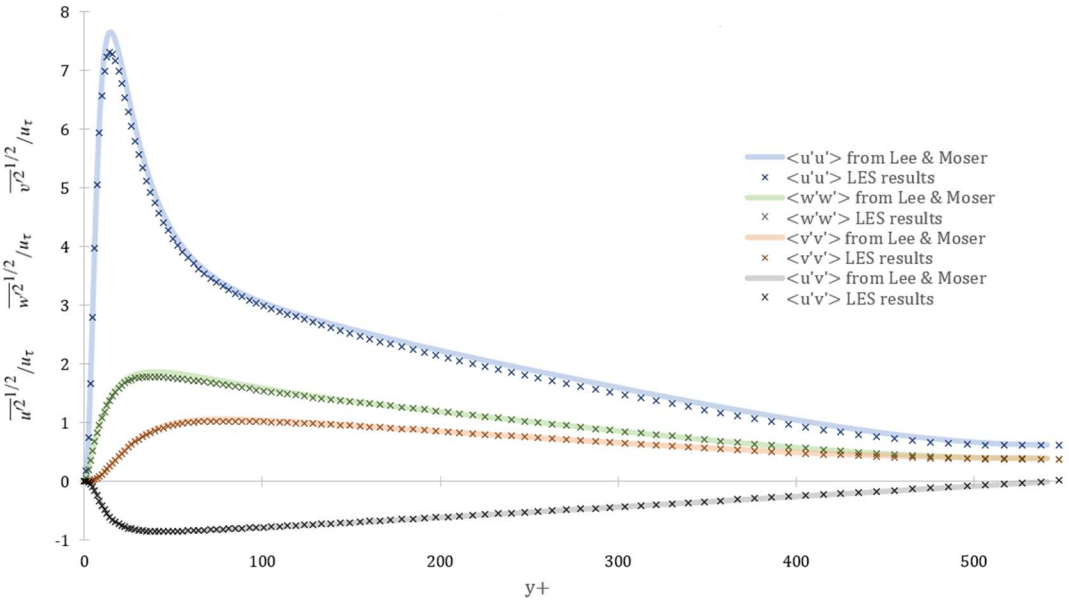


Figure 21: Root-mean-square velocity fluctuations normalized by the wall shear velocity. Thick solid line represents the data from Lee & Moser (2015), while the cross-markers represent the obtained LES results from the present work.

Finally, from these results we can easily obtain the turbulent kinetic energy (TKE) profile (figure 22), which is the trace (half) of the Reynolds stress tensor, as follows:

$$k = \frac{1}{2}[\overline{u'u'} + \overline{v'v'} + \overline{w'w'}]$$

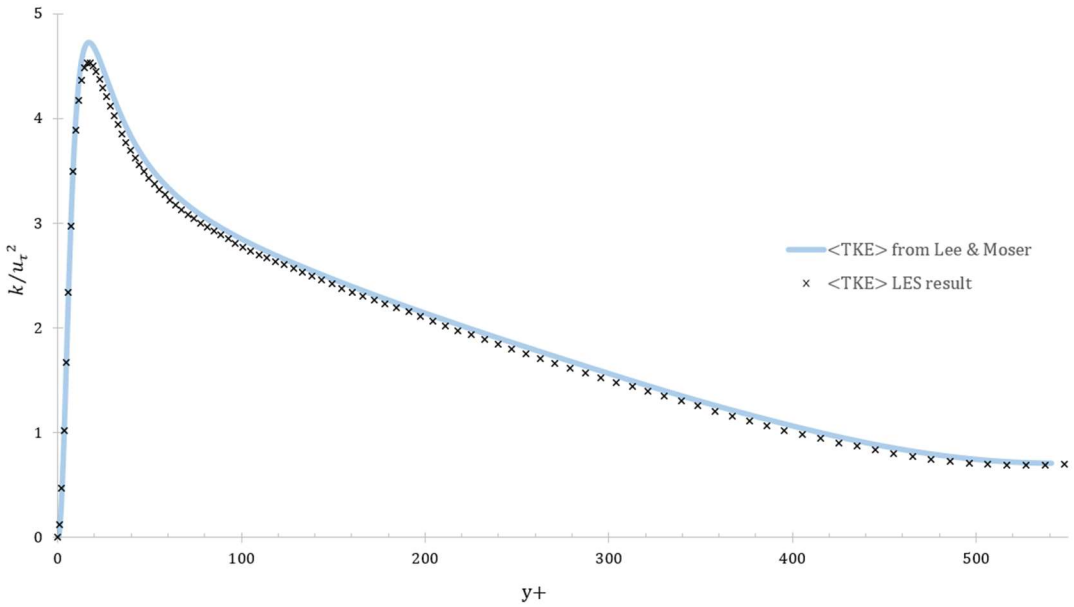


Figure 22: Turbulent kinetic energy (TKE) normalized by the wall shear velocity squared. Thick solid line represents the data from Lee & Moser (2015), while the cross-markers represent the obtained LES results from the present work.

Overall, we can conclude that our TCF LES results completely match those reported by Lee & Moser (2015) [15], concluding our first validation stage.

4.2 Non-Isothermal Turbulent Channel

4.2.1 Introduction

In our way to model our study case of interest, the following step in the validation process consists of validating the ability of the code and the adequacy of the settings for simulating unstable stratification problems. Therefore, we will proceed introducing buoyancy effects in a turbulent channel flow case.

Regarding the physics of the flow problem, the three dimensionless numbers that determine the dynamics of a turbulent channel flow under thermal unstable stratification are: Reynolds (Re_b), Rayleigh (Ra), and Prandtl (Pr) numbers:

$$Re_b = \frac{(2h)u_b}{\nu} \qquad Ra = \frac{\beta\ g\ \Delta\theta\ (2h)^3}{\alpha\ \nu} \qquad Pr = \frac{\nu}{\alpha}$$

Moreover, the magnitude(*) of the Richardson (Ri_b) number can be expressed as a combination of these 3 numbers as:

$$Ri_b = \frac{Ra}{\mathrm{Pr}\ (Re_b)^2} = \frac{2\ \beta\ g\ \Delta\theta\ h}{{u_b}^2}$$

In this regard, the work by Pirozzoli et al. (2017) [16] performed DNS simulations in pressure-driven turbulent channel flow with imposed unstable thermal stratification for a wide range of Reynolds and Rayleigh numbers, at fixed unity Prandtl number, providing an ideal reference for validation purposes.

The domain size requirement for an isothermal turbulent channel flow has been previously introduced, however, it is important to point out that the box-size requirements for the non-isothermal case are completely different. The reason for this lies on the fact that the flow structures that will appear are also different, and should not be constrained by the domain. In this regard Pirozzoli et al. (2017) performed a box-size study, concluding that a box of size $L_x = 16h$, $L_y = 2h$, $L_z = 8h$, where h is the half-channel height, was appropriate. Consequently, such flow geometry was also used in our validation work, and can be seen in figure 23.

(*) *Note that, according to the definition from Chapter 1, an unstable thermal stratification condition is characterized by $Ri < 0$. However, once the nature of the stratification condition is established to be unstable, it is easier to just use the magnitude of the Richardson number to characterize the strength of the unstable stratification condition. Therefore, from now on, all the cases described, which will range from neutral to unstable, will be characterized by the magnitude of the Richardson number.*

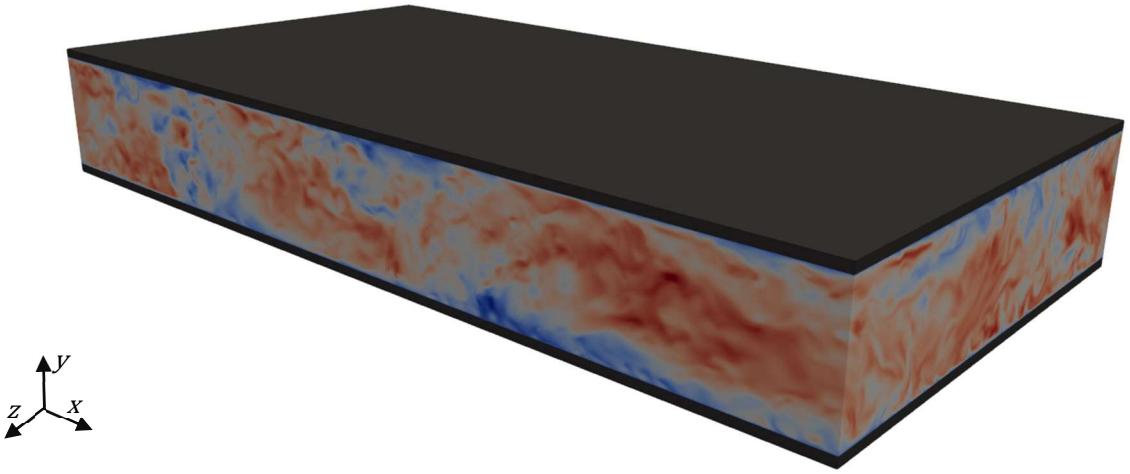


Figure 23: Geometry used in this work for the non-isothermal turbulent channel flow study.

Regarding the boundary conditions, the walls were no-slip and had a specified nondimensional temperature ($\theta_{bottom\,wall} = 1.0$ and $\theta_{top\,wall} = 0$), while periodic boundary conditions were used in the homogeneous directions, x and z. Whereas, regarding the numerics, the work by Pirozzoli et al. (2017) solved the incompressible Navier-Stokes equations and modelled the buoyancy effect using the Boussinesq approximation. The flow solver used was an existing solver described in Pirozzoli et al. (2016) [32]. Such solver uses staggered central second-order finite-differences in space, while time advancement uses an hybrid third-order Runge-Kutta algorithm coupled with a second-order Crank-Nicolson scheme on its fractional step procedure. Finally, convective and diffusive terms are treated explicitly and implicitly respectively.

Finally, among the different conditions studied in Pirozzoli et al. (2017), we will focus on our range of interest, which comprises weakly unstable stratification conditions, being the cases that will be simulated in this work: $Ri = 0.01$, $Ri = 1$, and $Ri = 10$. These three cases have been selected in order to visualize the evolution of the flow pattern from a shear-dominated situation ($Ri = 0.01$), to a situation near the range where Jayaraman and Brasseur (2021) [4] observed the strengthening of the rolls ($Ri = 1$) and, finally to a situation where buoyancy becomes so strong that the rolls break up ($Ri = 10$) (figure 25). These three cases perfectly illustrate the combined effects of shear and buoyancy, as well as the existence of a sweet-spot regarding the strengthening of the streamwise rolls, providing with a perfect case for our validation purposes, which will ensure that we are properly simulating the physics we are interested in.

To start with, the results from Pirozzoli et al. (2017) shown in figure 24 will be used to conduct a detailed quantitative validation of the turbulence statistics for each flow case.

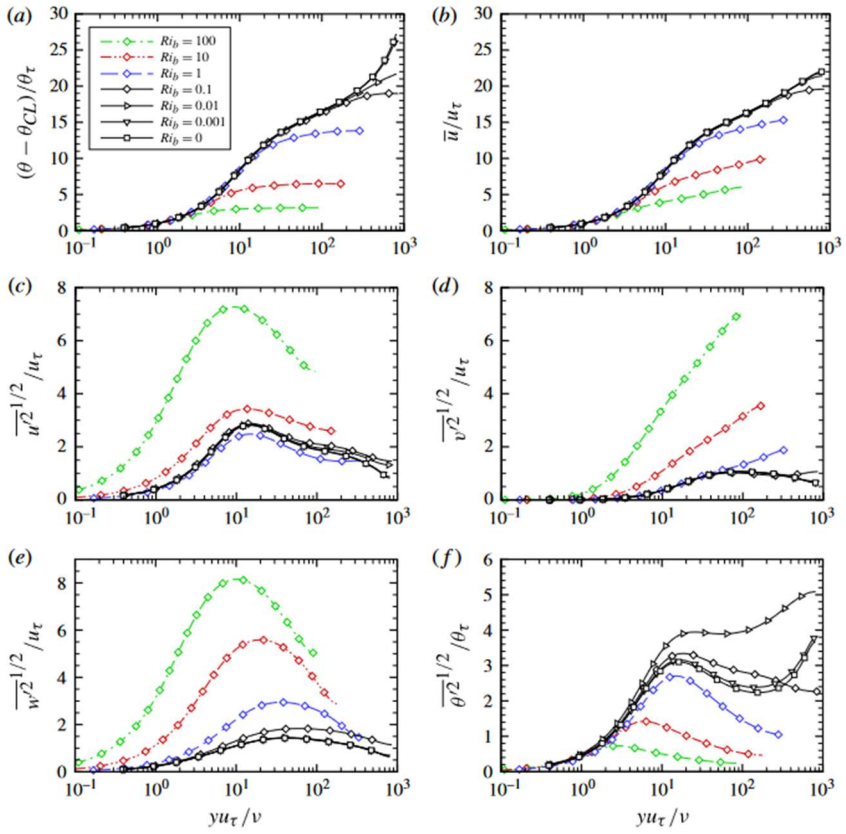


Figure 24: Turbulence statistics for quantitative comparison, from Pirozzoli et al. (2017) [16].

In addition, a more qualitative analysis will be conducted using some of the results obtained by Pirozzoli et al. (2017) that are summarized in figure 25. Instantaneous vertical (wall-normal) velocity fluctuations (v') and temperature fluctuations (θ') are shown, for different Richardson numbers, at the channel centre plane ($y = h$). The contour plots are composed of 24 contour levels representing each variable on a range which spans ± 3 standard deviations of that variable from its mean value, being negative values blue and positive values red. Therefore, those fluctuating quantities are represented in normalized terms relative to the deviation from their mean value, each plot having a different range scale. Meaning that the same colour on two different Ri-cases plots does not mean the same absolute value of the fluctuation.

As already described in previous sections, we can identify two limit cases regarding the turbulence structures in a wall-bounded flow. On one hand, a shear-dominated turbulent flow ($Ri \to 0$) is characterized by shear-driven elongated structures. While, on the other hand, a buoyancy-dominated turbulent flow ($Ri \gg 1$) is characterized by vertical Rayleigh-Bénard-like updraughts that dismantle any streamwise elongated structures. However, in between these two limit cases, there are states where both, shear and buoyancy are of similar magnitude, such that the shear-driven streamwise-elongated structures are still a feature of the flow, not being dismantled by vertical updraughts, but being strengthened instead, bringing as a consequence the formation of the large-scale rolls that have been described in Chapter 1. Having all of this in mind, some interesting comments regarding the results shown on figure 25 will follow.

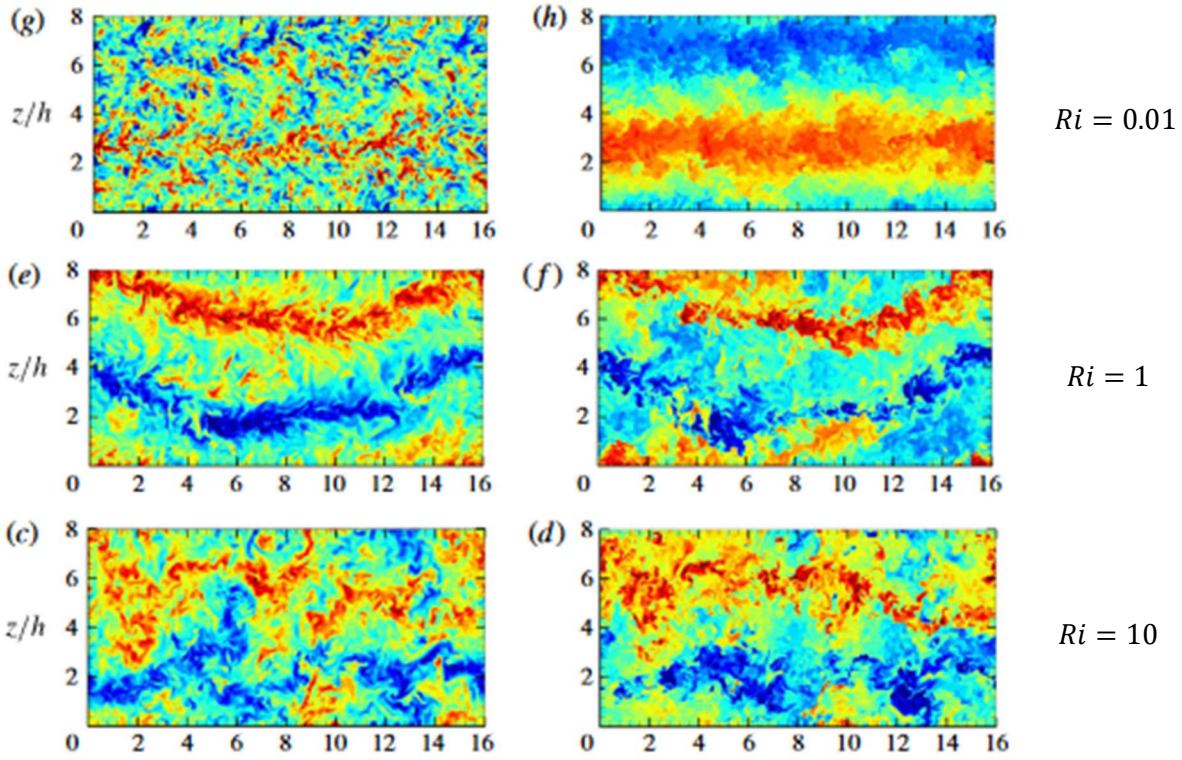


Figure 25: Instantaneous vertical (wall-normal) velocity fluctuations (left) and temperature fluctuations (right) at the channel centre for different Richardson numbers, from Pirozzoli et al. (2017). The contour plots show 24 contour levels representing each variable on a range of ±3 standard deviations from its mean value, being negative values blue and positive values red.

On one hand, it is interesting to observe that for the $Ri = 0.01$ case we can already see some correlation between the wall-normal velocity fluctuations and the temperature fluctuations. However, in such a low Richardson number flow, buoyancy effects are not strong enough to have a significant impact on the global turbulence structure and, therefore, we see the usual tending-to-isotropic turbulence which is characteristic of the centreline of an isothermal turbulent channel.

On the other hand, observing the $Ri = 1$ case, we can see how the buoyancy has become strong enough to cause transition from a shear-driven turbulence structure to a structure composed of streamwise elongated large-scale rolls that span the entire channel height, in the same manner as described in Chapter 1 for the Atmospheric Boundary Layer (ABL). Moreover, it can be seen that the range where the rolls appear for the non-isothermal turbulent channel is similar to the range where the large-scale rolls appeared for the ABL in Jayaraman & Brasseur (2021) work, being such range around $Ri = 1$, and reaching the maximally coherent state for $Ri = 1.08$ [4].

Finally, the case for $Ri = 10$ is ideal to visualize how, as buoyancy becomes more dominant, the coherent elongated structures are blown up and substituted by vertical Rayleigh-Bénard-like updraughts.

4.2.2 Governing Equations

As introduced in section 3.2, Nek5000 spectrally solves the Conservative Form of the Incompressible Navier-Stokes Equations (Momentum and Mass conservation), for constant fluid viscosity and density:

$$\nabla \cdot \boldsymbol{u} = 0$$

$$\rho\left(\frac{\partial \boldsymbol{u}}{\partial t} + \nabla \cdot (\boldsymbol{u}\boldsymbol{u})\right) = -\nabla p + \mu \nabla^2 \boldsymbol{u} + \rho \boldsymbol{f}$$

Where, f is the forcing term (acceleration) as defined by Boussinesq approximation, and which will be described in more detail in the upcoming section:

$$f = g\beta(T - T_{ref})$$

While, the Temperature field is described by the Energy Equation:

$$\rho c_p \left(\frac{\partial T}{\partial t} + \boldsymbol{u} \cdot \nabla T\right) = \nabla \cdot (\lambda \nabla T)$$

Finally, the energy drain to model sub-grid scales dissipation is achieved by applying the Explicit Filter [23] introduced in section 3.3.

4.2.3 Buoyancy Treatment – Boussinesq Approximation

For weakly unstable thermal stratification conditions, the buoyancy effect can be approximated by the Boussinesq approximation. Using this approximation, the buoyancy effects can be accounted for by modelling a body-force term, rather than including a variable flow density, which makes the simulation much more simple. This theory breaks down when the temperature differences becomes large, as studied in the work by Gray & Giorgini (1976) [33] where, apart from providing with a new method for deriving the Boussinesq approximation, the limits of its validity were explicitly determined, using non-dimensional analysis, in terms of temperature differences and length-scales. In conclusion, since in our study cases we limit ourselves to weakly unstable stratification conditions, we can safely consider Boussinesq approximation as being valid. Moreover, the work by Pirozzoli et al. [16] used the Boussinesq approximation as well, therefore we shall use the same model for buoyancy to compare to their results.

The Boussinesq forcing term is defined as:

$$F_{Boussinesq} = \rho g \beta (T - T_{ref})$$

Moreover, as previously introduced, the three dimensionless numbers that determine the dynamics of our flow problem are Reynolds, Rayleigh, and Prandtl numbers*:*

$$Re_b = \frac{(2h)u_b}{\nu} \qquad Ra = \frac{\beta\ g\ \Delta\theta\ (2h)^3}{\alpha\ \nu} \qquad Pr = \frac{\nu}{\alpha}$$

Where: $2h$ is the channel height.

While, the magnitude of the Richardson number can be expressed as a combination of these 3 numbers as:

$$Ri_b = \frac{Ra}{\mathrm{Pr}\ (Re_b)^2} = \frac{2\ \beta\ g\ \Delta\theta\ h}{{u_b}^2}$$

Setting up the desired dimensionless numbers: Re_b, Ra, Pr

This subsection provides a description of the calculations required to properly set up the nondimensional parameters of the simulation. For convenience, some parameters are set to unity:

$$\rho = 1.0 \qquad c_p = 1.0 \qquad u_b = 1.0 \qquad \Delta\theta = 1.0 \qquad h = 1$$

To find the appropriate value of dynamic viscosity (μ) we proceed as follows:

$$Ri_b = \frac{Ra}{\mathrm{Pr}\ (Re_b)^2} \rightarrow (Re_b)^2 = \frac{Ra}{Ri_b\,\mathrm{Pr}}$$

$$\left[\frac{2\ \overbrace{h}^{=1}\ u_b}{\frac{\mu}{\underbrace{\rho}_{=1}}}\right]^2 = \frac{Ra}{Ri_b\,\mathrm{Pr}} \rightarrow \frac{[2\ u_b]^2 Ri_b\,\mathrm{Pr}}{Ra} = \mu^2$$

$$\mu = 2\ \overbrace{u_b}^{=1}\sqrt{\frac{Ri_b\,\mathrm{Pr}}{Ra}} = 2\sqrt{\frac{Ri_b\,\mathrm{Pr}}{Ra}}$$

Using the obtained value of dynamic viscosity (μ) one can check that we have the right Reynolds:

$$Re_b = \frac{(2h)u_b}{\nu} = \frac{\overbrace{\rho}^{=1}\left(2\overbrace{h}^{=1}\right)\overbrace{u_b}^{=1}}{\mu} = \frac{2}{\mu}$$

Once the dynamic viscosity (μ) has been determined, we set the thermal conductivity (λ) so that we get the desired Prandtl number ($\mathrm{Pr} = 1$).

$$Pr = \frac{\nu}{\alpha} = \frac{\frac{\mu}{\underbrace{\rho}_{=1}}}{\frac{\lambda}{\underbrace{\rho\ c_p}_{=1}}} = \frac{\mu}{\lambda} = 1 \rightarrow \lambda = \mu$$

Moreover, the dimensionless temperature (θ) definition reduces the temperature boundary conditions to:

$$\theta = \frac{T - T_{top\ wall}}{T_{bottom\ wall} - T_{top\ wall}}$$

$$\theta_{bottom\ wall} = 1.0 \qquad \theta_{top\ wall} = 0$$

Finally, the Boussinesq forcing term can be added to the "*userf*" subroutine from the so-called "*user*" file in Nek5000, as an acceleration per unit volume ($\widetilde{ffy}$):

$$\tilde{F} = \rho\ g\ \beta\ (\theta - \theta_{ref}) \qquad \left[\frac{force}{unit\ volume}\right]$$

$$\widetilde{ffy} = g\ \beta\ (\theta - \theta_{ref}) = g\ \beta\ \theta \qquad \left[\frac{acceleration}{unit\ volume}\right]$$

$\theta_{ref} = 0$, defined as the temperature at the top wall.

Where the factor ($g\ \beta$) can be expressed in terms of the Rayleigh number to obtain the forcing acceleration per unit volume ($\widetilde{ffy}$):

$$Ra = \frac{\beta\ g\ \overbrace{\Delta\theta}^{=1} \left(2\ \overbrace{h}^{=1}\right)^3}{\alpha\ \nu} = \frac{\beta\ g\ (2)^3}{\frac{\nu^2}{\underbrace{Pr}_{=1}}} = \frac{\beta\ g\ (2)^3}{\left(\frac{\mu}{\underbrace{\rho}_{=1}}\right)^2} \rightarrow \beta\ g = \frac{Ra\ \mu^2}{(2)^3}$$

$$\widetilde{ffy} = g\ \beta\ (\theta - \theta_{ref}) = \frac{Ra\ \mu^2}{(2)^3}\ \theta$$

Alternatively, the acceleration per unit volume can also be found using Richardson number:

$$Ri_b = \frac{Ra}{\mathrm{Pr}\ (Re_b)^2} = \frac{2\ \beta\ g\ \overbrace{\Delta\theta}^{=1}\ \overbrace{h}^{=1}}{\underbrace{{u_b}^2}_{=1}} = 2\ \beta\ g \rightarrow \beta\ g = \frac{Ri_b}{2}$$

$$\widetilde{ffy} = g\ \beta\ (\theta - \theta_{ref}) = \frac{Ri_b}{2}\ \theta$$

4.2.4 Domain Discretization - Mesh

The LES meshes used for the non-isothermal turbulent channel flow will use the same mesh quality guidelines that were used in the isothermal turbulent channel flow case, i.e. the criteria for well-resolved LES by Negi et al. [29], $\Delta y_w^+ < 1$; $\Delta x^+ < 20$; $\Delta z^+ < 9$. However, in mixed convection problems an extra check has to be conducted to make sure that we are not only resolving properly the momentum boundary layer, but that the thermal boundary layer is also being properly resolved.

Following the steps from Pirozzoli et al. [16], the reference by Shishkina et al. 2010 [34] is used for checking that the thermal boundary layer is being properly resolved. This work provides correlations that allow us to estimate the number of nodes that have to be placed within the thermal and the momentum boundary layers, so that one can verify a posteriori if the thermal boundary layer is being properly resolved. Relations (42) and (43) from Shishkina et al. 2010 [34] provide the estimate of the minimum number of nodes that the computational mesh needs to have in each the thermal and the momentum boundary layers. Which for our particular study case in which Prandtl number is = 1, means that the resolution needed to resolve the thermal boundary layer is exactly the same as the needed to resolve the momentum boundary layer [34]. From this, we can state that if we build our mesh in a way that the momentum boundary layer is properly resolved (i.e. $y^+ < 1$) we should be on the safe side and we will also be resolving properly the thermal boundary layer.

Moreover, reasoning from a conceptual point of view: in a fluid with Prandtl number unity, in laminar regime, the thermal and momentum boundary layers will have the same thickness. However, in a turbulent boundary layer their relative thickness could be influenced by the turbulent mixing, which is related to the turbulent Prandtl number. In general, for a low Reynolds turbulent boundary layer -meaning not too extreme effects from turbulent mixing-, if the fluid's Prandtl number is =1, and if we are not too far from neutral conditions, one would expect the thermal and the momentum boundary layer thicknesses to be of a similar order of magnitude. Therefore, we can safely initially assume that the thermal and the momentum boundary layers will be of similar thickness, build our mesh so that it satisfies the criteria for resolving the momentum boundary layer (i.e. $y^+ < 1$), and we can check a posteriori from our results that the thermal boundary layer is indeed similar order of magnitude as the momentum BL, which will prove that the thermal boundary layer is properly resolved. The results from this a posteriori check are shown in figure 26, where we could verify that indeed the thermal boundary layer and the momentum boundary layer have virtually the same thickness, which finally confirms that our mesh design criteria was correct and both the momentum and the thermal boundary layer are being properly resolved.

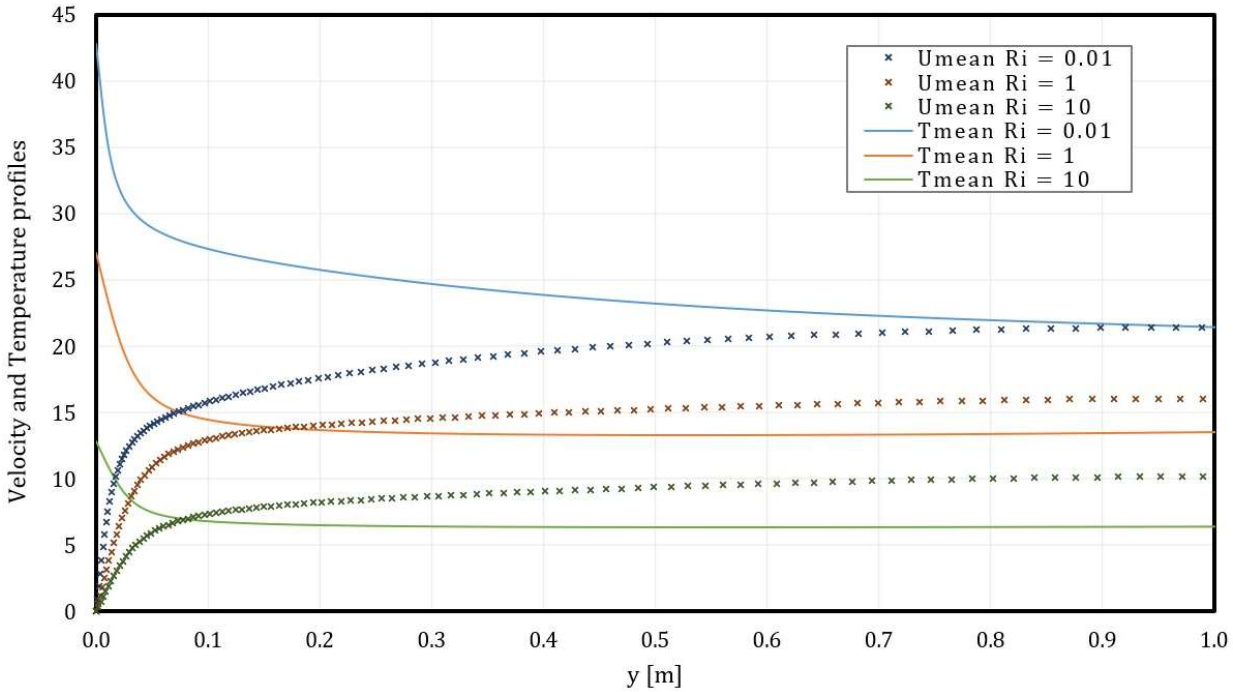


Figure 26: Figure from our a posteriori check that confirms that the momentum and the thermal boundary layers virtually have the same thickness, confirming that the mesh used in the simulations properly resolves both boundary layers.

Finally, table 3 summarizes the main features of the used meshes for each of the cases. We can conclude that our meshes satisfy the guidelines suggested by Negi et al. [29], except by $Ri = 0.01$ case, whose higher Reynolds number would have made the simulation too time consuming. For that case, we have been more permissive, however, it is still a completely reasonable resolution for an LES.

Additionally, using the estimated of the Kolmogorov length-scale in wall units discussed in section 4.1.4, we have also expressed our mesh resolution in terms of Kolmogorov-length-scales. Despite the fact that it is just an approximation, it is already insightful.

	N_x	N_y	N_z	*wall stretching parameter*	*polynomial order*	Δy_w^+	Δx_{max}^+	Δz_{max}^+	Δy_{max}^+
$\boldsymbol{Ri = 10}$	60	14	52	1.8	7	< 0.41	10.3 ($\sim 5.1\,\eta$)	5.9 ($\sim 2.95\,\eta$)	10.2 ($\sim 5.1\,\eta$)
$\boldsymbol{Ri = 1}$	60	16	52	1.9	7	< 0.60	20.2 ($\sim 10.1\,\eta$)	11.6 ($\sim 5.8\,\eta$)	18.4 ($\sim 9.2\,\eta$)
$\boldsymbol{Ri = 0.01}$	66	18	54	2.2	7	< 0.81	43.1 ($\sim 21.55\,\eta$)	26.3 ($\sim 13.15\,\eta$)	43.6 ($\sim 21.8\,\eta$)

Table 3: Summary showing mesh resolution, stretching parameter and polynomial order used for each case. Nx, Ny, Nz represent the number of global mesh elements in each direction. Resolutions are expressed in wall units, together with an estimate in Kolmogorov-length-scale-units.

4.2.5 Simulation Settings

The simulation has been set up using the same domain and boundary conditions used by Pirozzoli et al. (2017), which have been introduced in section 4.2.1. The flow development has been assessed by monitoring the wall shear stress time evolution, being the flow considered as fully developed only when the signal was fluctuating around a fixed mean value. Only once the flow has proven to be fully developed did we start taking statistics. Figure 27 shows the behaviour of the wall shear stress signal over a period of 200 seconds once the flow was already fully developed.

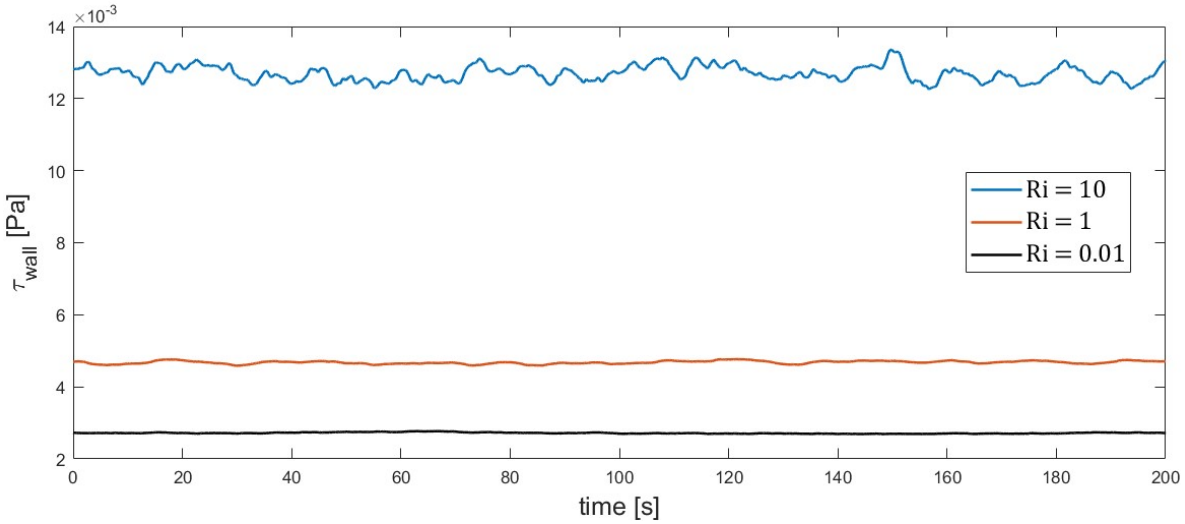


Figure 27: Wall-shear stress signal over a period of 200 seconds proving the flow is fully developed for the studied cases.

Regarding the required averaging window in order to obtain proper statistics, due to the lack of references on the required averaging window for a non-isothermal channel flow, the criteria for an isothermal turbulent channel flow by Mason & Callen [30] has been used as a first guess. The adequacy of the such averaging window will be evaluated a posteriori by setting up consecutive simulations and comparing the results, as well as, by analysing the effect of doubling the averaging window. These a posteriori tests will be described in section 4.2.6.

According to Mason & Callen, once the flow is fully developed, the required averaging window to properly capture the statistics of the flow can be estimated as:

$$10\frac{h}{u_\tau}$$

Where $h = 1$ is the half-channel-width.

	$\boldsymbol{u_\tau}$	$\boldsymbol{10\frac{h}{u_\tau}}$
$\boldsymbol{Ri = 0.01}$	$5.2 \cdot 10^{-2}$	191.82
$\boldsymbol{Ri = 1}$	$6.8 \cdot 10^{-2}$	147.19
$\boldsymbol{Ri = 10}$	0.113	88.48

Table 4: Required averaging window for each case according to the criterion by Mason & Callen.

Table 4 summarizes the averaging window requirements for our three cases of study. From those observations, and due to the relatively low computational cost of such a simulation, it has been decided that an averaging window of 200 seconds will be used for all the three cases.

Regarding the numerical scheme and running settings, a 2nd order backward differences scheme, together with operator-integration factor scheme (OIFS) extrapolation, has been used for the time stepping. Such combination on Nek5000 usually allows to use up to $CFL = 5$ without any stability issues [31]. However, in this case, due to the presence of the Boussinesq forcing term, the CFL had to be lowered to keep the simulation stable.

This constrain on the time-step is more restrictive the more dominant buoyancy becomes. Since the Boussinesq term is directly proportional to the Richardson number, this means that the constrain was more critical for the $Ri = 10$ case, for which the CFL number had to be brought down to 1.4. On the other hand, for $Ri = 1$ and $Ri = 0.01$, we could use $CFL = 1.5$ and $CFL = 1.7$ respectively.

Finally, it is relevant to mention that in addition to setting up an appropriate CFL so that the computation remains stable, a time-step independency study has been conducted, testing lower target CFL and verifying that the solution no longer changes when reducing CFL.

4.2.6 Results and Discussion

The comparison of the heat transfer and skin friction can be done, in global terms, by means of known dimensionless numbers. The heat transfer at the wall can be characterized by the Nusselt number (Nu), which is defined as:

$$Nu = \frac{2\, q_w\, h}{\alpha\, \Delta\theta}$$

Where:

$$q_w \; is \; the \; wall \; heat \; flux \; in \; W/m^2 \qquad \text{and} \qquad h \; is \; the \; half - channel \; height$$

While the skin friction is commonly parametrized by the Friction Coefficient (C_f):

$$C_f = \frac{2\, \tau_w}{\rho\, {u_b}^2}$$

If the Prandtl number is set to unity ($Pr = 1$), the thee dimensionless numbers that govern the flow are: Reynolds (Re_b), Richardson (Ri_b), and Rayleigh (Ra) numbers. Table 5 summarizes the main parameters for each of the three computed cases, together with the nondimensional numbers obtained in the current study compared to the ones reported by Pirozzoli et al. (2017) [16].

	$Ri_b = 0.01$	$Ra = 10^7$	$Re_b = 31{,}623$
Present work results	$Re_\tau = \frac{h\, u_\tau}{\nu}$	$Nu = \frac{2\, h\, q_w}{\alpha\, \Delta\theta}$	$C_f = \frac{2\, \tau_w}{\rho\, {u_b}^2}$
	824.50	38.52	$5.44 \cdot 10^{-3}$
Pirozzoli et al.	823.19	37.87	$5.42 \cdot 10^{-3}$
Relative discrepancy	0.16%	1.71%	0.34%

	$Ri_b = 1$	$Ra = 10^8$	$Re_b = 10{,}000$
Present work results	$Re_\tau = \frac{h\, u_\tau}{\nu}$	$Nu = \frac{2\, h\, q_w}{\alpha\, \Delta\theta}$	$C_f = \frac{2\, \tau_w}{\rho\, {u_b}^2}$
	342.02	25.31	$9.36 \cdot 10^{-3}$
Pirozzoli et al.	351.01	25.44	$9.85 \cdot 10^{-3}$
Relative discrepancy	2.56%	0.52%	4.99%

	$Ri_b = 10$	$Ra = 10^8$	$Re_b = 3{,}162$
Present work results	$Re_\tau = \frac{h\, u_\tau}{\nu}$	$Nu = \frac{2\, h\, q_w}{\alpha\, \Delta\theta}$	$C_f = \frac{2\, \tau_w}{\rho\, {u_b}^2}$
	178.16	27.73	$2.54 \cdot 10^{-2}$
Pirozzoli et al.	179.12	27.67	$2.56 \cdot 10^{-2}$
Relative discrepancy	0.54%	0.22%	0.81%

Table 5: Imposed Richardson, Rayleigh and Reynolds for each of the study cases, together with the resulting frictional Reynolds, Nusselt, and Friction Coefficient, in comparison with Pirozzoli et al. (2017) results [29].

It can be seen from table 5 that the matching of those relevant dimensionless numbers is accurate, exhibiting in most of the cases a relative discrepancy with the DNS reference of less than 2%. This observation proves that the global heat and momentum exchange between flow and walls is accurately predicted, the only exception being the case for $Ri = 1$ which, despite having a perfect match of the heat transfer, shows a slightly larger discrepancy on the momentum exchange with the wall, rising the relative discrepancy of the skin friction coefficient up to almost 5%.

More analysis will be conducted on the $Ri = 1$ case, however, an explanation for this larger discrepancy can be anticipated by arguing that a case where both competing phenomena, buoyancy and shear, are of the same order of magnitude ($Ri = 1$) is physically a more challenging situation compared to a case where either buoyancy or shear is dominating by 1 or 2 orders of magnitude, corresponding to $Ri = 10$ and $Ri = 0.01$ respectively.

On the other hand, the analysis of turbulence statistics allows for a more detailed and local validation. In this regard, figures 28-33 show the turbulence statistics, normalized by frictional velocity and temperature, together with the data reported by Pirozzoli et al. (2017) [16].

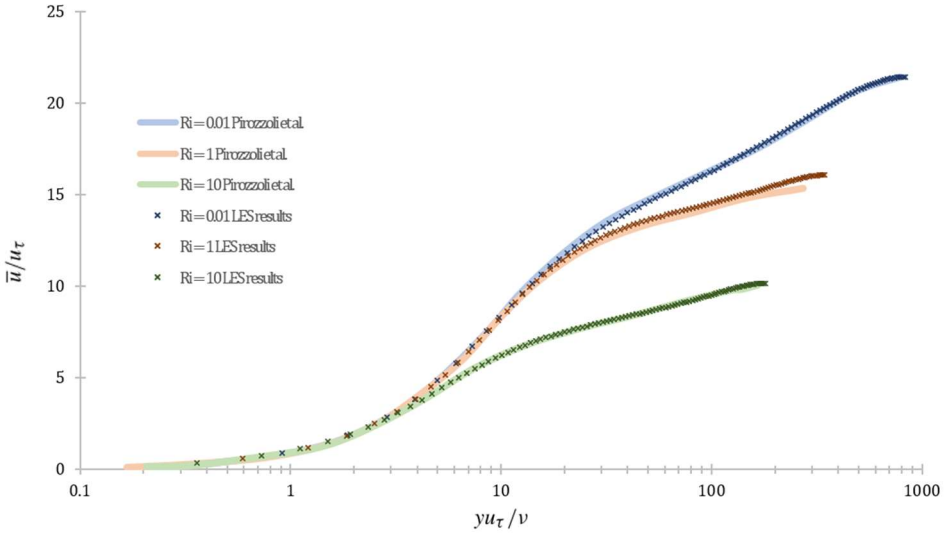


Figure 28: Shear-scaled mean velocity profile for Ri = 0.01, 1, and 10. Thick solid lines representing the results from Pirozzoli et al., while cross-markers represent the obtained LES results in the present work.

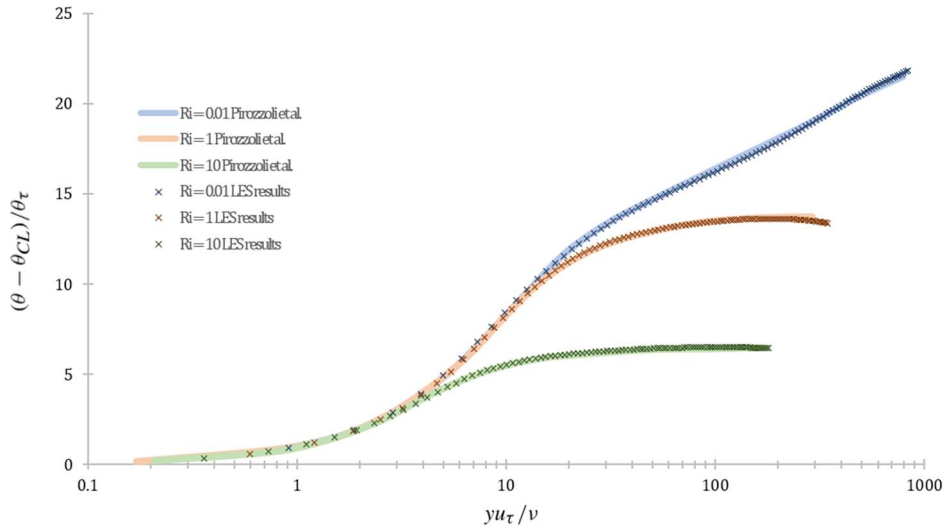


Figure 29: Shear-scaled mean temperature profile for Ri = 0.01, 1, and 10. Thick solid lines representing the results from Pirozzoli et al., while cross-markers represent the obtained LES results in the present work.

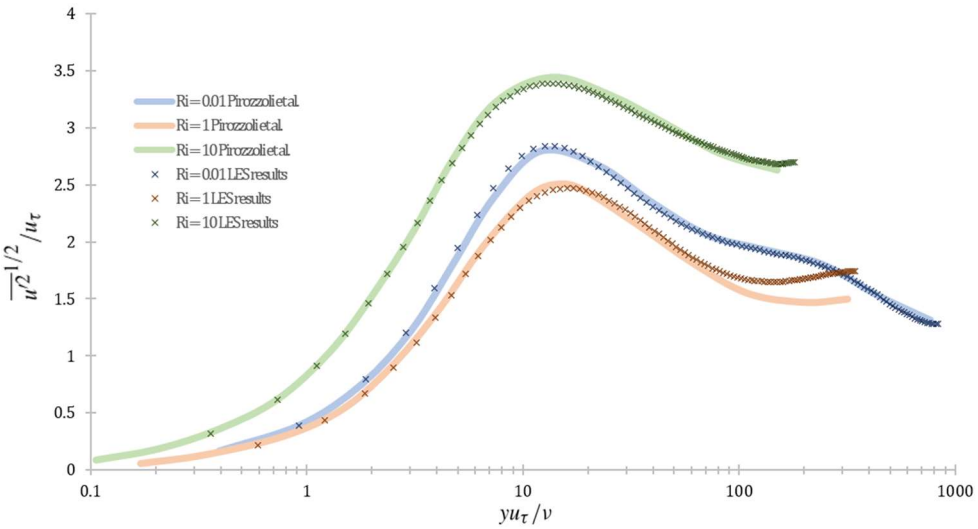


Figure 30: Shear-scaled streamwise velocity fluctuations for Ri = 0.01, 1, and 10. Thick solid lines representing the results from Pirozzoli et al., while cross-markers represent the obtained LES results in the present work.

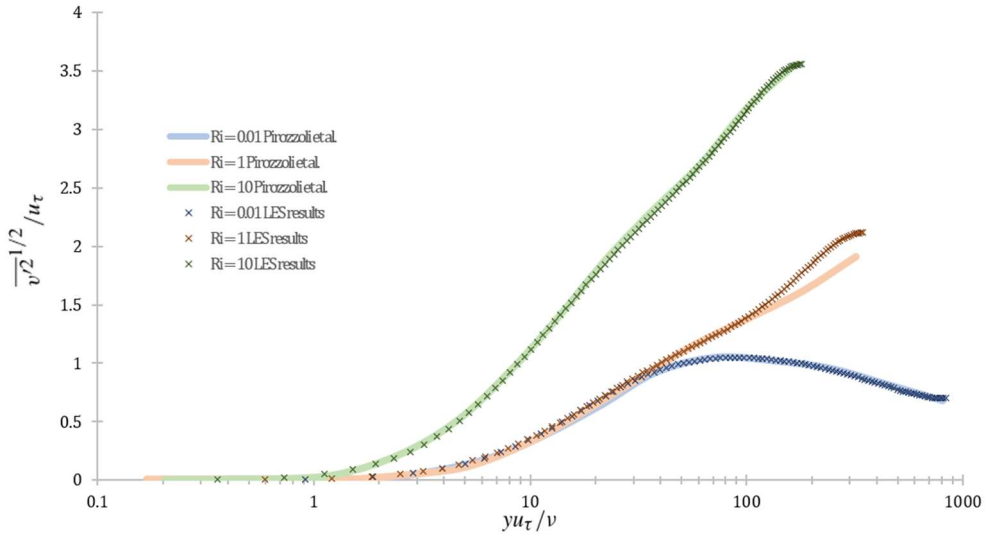


Figure 31: Shear-scaled vertical velocity fluctuations for Ri = 0.01, 1, and 10. Thick solid lines representing the results from Pirozzoli et al., while cross-markers represent the obtained LES results in the present work.

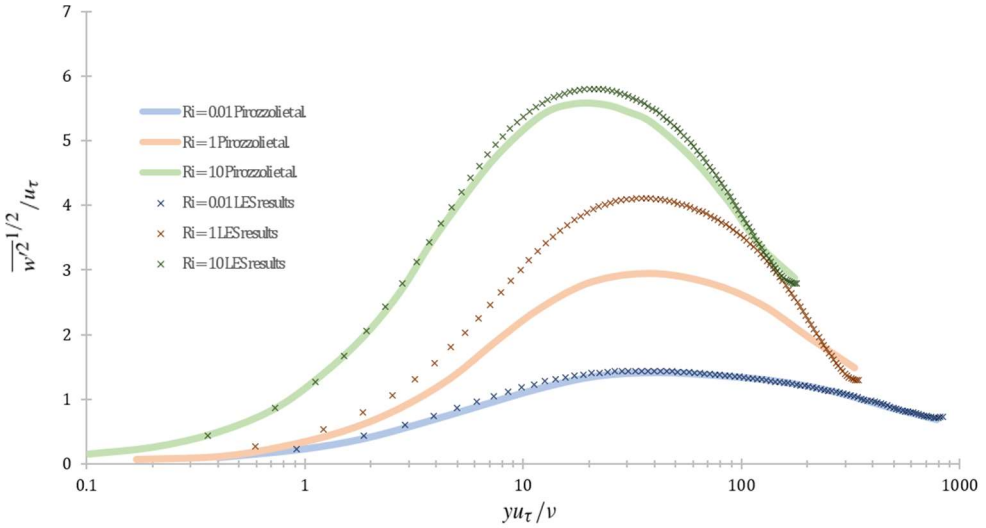


Figure 32: Shear-scaled spanwise velocity fluctuations for Ri = 0.01, 1, and 10. Thick solid lines representing the results from Pirozzoli et al., while cross-markers represent the obtained LES results in the present work.

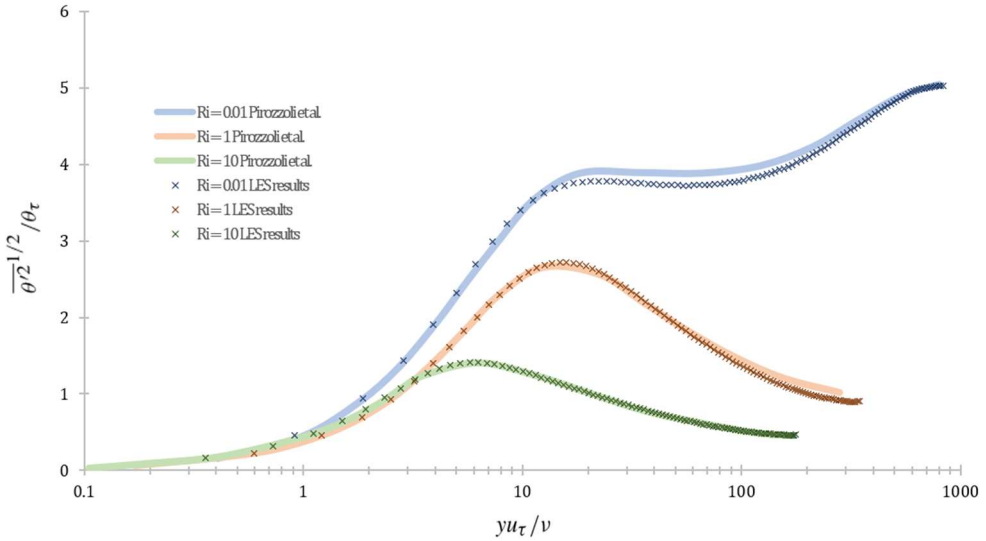


Figure 33: Shear-scaled temperature fluctuations for Ri = 0.01, 1, and 10. Thick solid lines representing the results from Pirozzoli et al., while cross-markers represent the obtained LES results in the present work.

As seen in figures 28-33, the turbulence statistics for $Ri = 0.01$ and $Ri = 10$ cases are virtually the same as the reported from the reference paper for both, the mean flow and the fluctuating quantities, proving a perfect prediction of the turbulence flow features for those cases.

However, in a similar manner that what was observed when analysing the Nusselt number and the Friction Coefficient, the matching is not that perfect when it comes to the $Ri = 1$ case, which still matches the mean profiles but misses some fluctuating quantities in the region near the channel centreline. In particular, the diagonal terms of the Reynolds stress tensor - $\overline{u'u'}$, $\overline{v'v'}$, and $\overline{w'w'}$ - are overpredicted in the vicinity of the channel centreline, meaning that there seems to be an accumulation of turbulent kinetic energy in that region, which could be the consequence of an insufficient energy drainage from our sub-grid-scale model.

Finally, it is also relevant to point out that despite the fact that the $Ri = 1$ case shows some discrepancies on the fluctuating velocity terms, the temperature fluctuations do match the reference data. This observation is consistent with, and is probably related to, our previous observation that the Nusselt number for the $Ri = 1$ case exhibited a relative discrepancy with the reference of 0.52%, while the Friction Coefficient was exhibiting a discrepancy of 4.99%, meaning that heat transfer was being better predicted than momentum transfer.

In order to make sure that the observed slight discrepancy that our LES results shows for the $Ri = 1$ case is not due to an incorrect set up of our simulation, we proceed with some tests, while discussing possible reasons of such mismatch.

First of all, we are certain that it does not have to do with a poor mesh resolution because the mesh has been designed following highly accepted state of the art references and we have also taken care to verify that both, momentum and thermal boundary layers, are properly resolved. However, to provide a proof for it, a mesh with DNS resolution, whose features are summarized in table 6, has been tested.

	N_x	N_y	N_z	wall stretching parameter	polynomial order	Δy_w^+	Δx_{max}^+	Δz_{max}^+	Δy_{max}^+
DNS mesh for $Ri = 1$	100	24	80	2.0	7	< 0.32	12.1 ($\sim 6.1\,\eta$)	7.6 ($\sim 3.8\,\eta$)	13.0 ($\sim 6.5\,\eta$)
LES mesh for $Ri = 1$	60	16	52	1.9	7	< 0.60	20.2 ($\sim 10.1\,\eta$)	11.6 ($\sim 5.8\,\eta$)	18.4 ($\sim 9.2\,\eta$)

Table 6: Features of the DNS-resolution mesh tested for $Ri = 1$ case, compared to the original LES mesh.

In conclusion, as it can be seen in figures 34-39, the results obtained with the DNS-resolution mesh for the $Ri = 1$ case are virtually the same as the ones previously obtained with our LES mesh, providing with the final proof that our LES mesh is perfectly well-suited for our flow problem and that it cannot be the reason for the results discrepancy.

On the other hand, the observed higher turbulent kinetic energy in the bulk of the flow, in the centre line region, could suggest that there might be a lack of flow development. Despite the fact that proper flow development has already been verified by monitoring the tangential wall stress and verifying that it stabilizes fluctuating around a fixed mean value, an extra test was conducted. The test consisted of running 4 consecutive runs of the $Ri = 1$ case, verifying that we obtain the exact same results for all 4 simulations. In addition, the last of those simulations used an averaging window twice as long (now 400 s, while originally it was 200 s), obtaining again the same results, as it can be seen in figures 34-39. This series of tests confirms that our flow solution is already fully developed, and it also proves that the used averaging window is sufficient to capture the flow statistics.

Finally, a check on the adequacy of the used time-step (through imposed CFL) has been conducted. Initially, the $Ri = 1$ case had been run targeting $CFL = 1.5$, therefore, we restart the case reducing the CFL to 0.5. Once again, the results obtained are exactly the same as obtained with the originally used CFL, as it can be seen on figures 34-39.

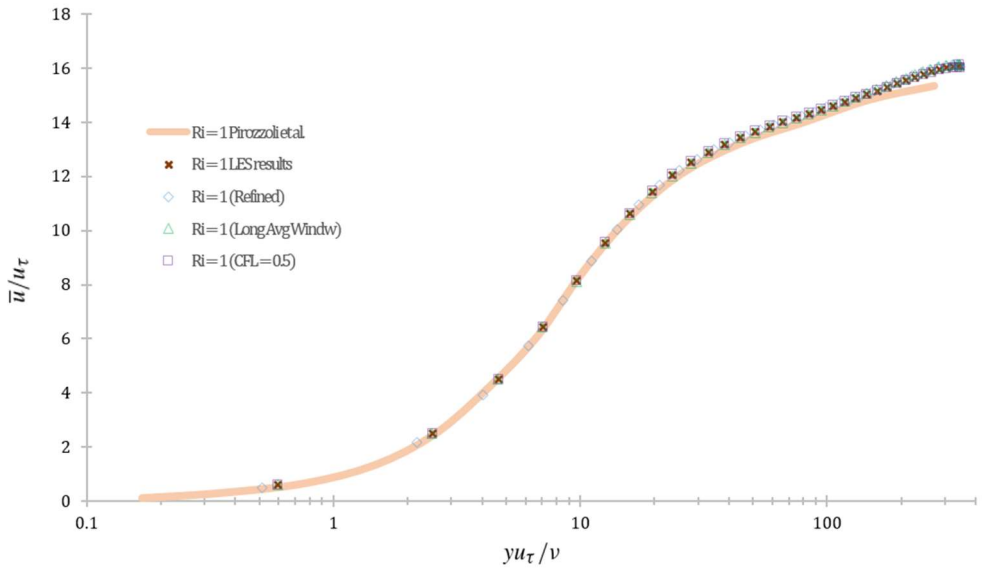


Figure 34: Shear-scaled mean velocity profile for Ri = 1, assessing the potential effect of mesh refinement, increase of averaging window, and reduction of target CFL.

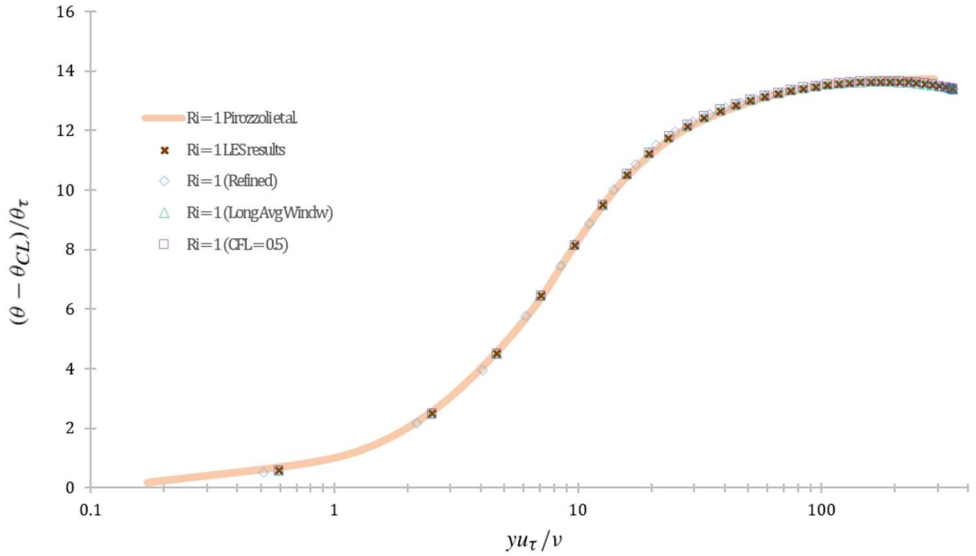


Figure 35: Shear-scaled mean temperature profile for Ri = 1, assessing the potential effect of mesh refinement, increase of averaging window, and reduction of target CFL.

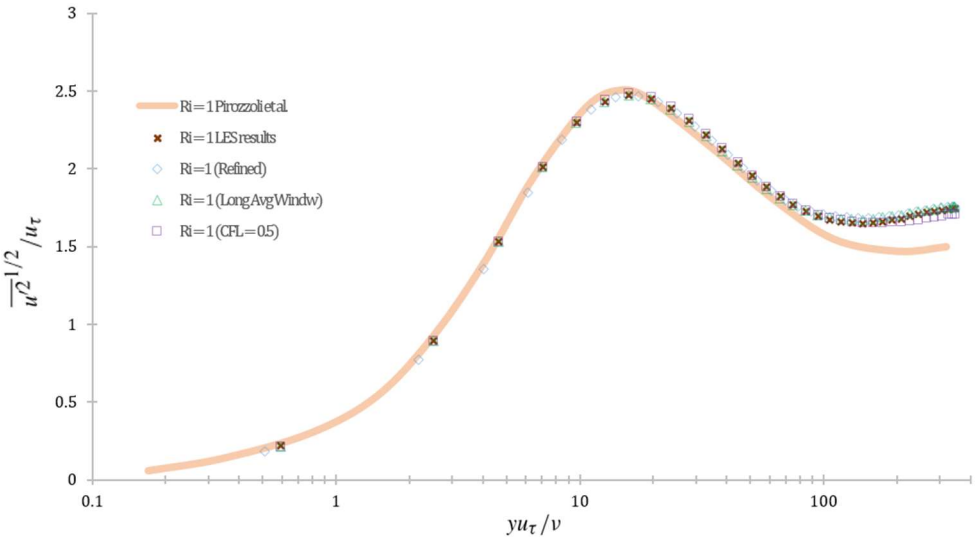


Figure 36: Shear-scaled streamwise velocity fluctuations for Ri = 1, assessing the potential effect of mesh refinement, increase of averaging window, and reduction of target CFL.

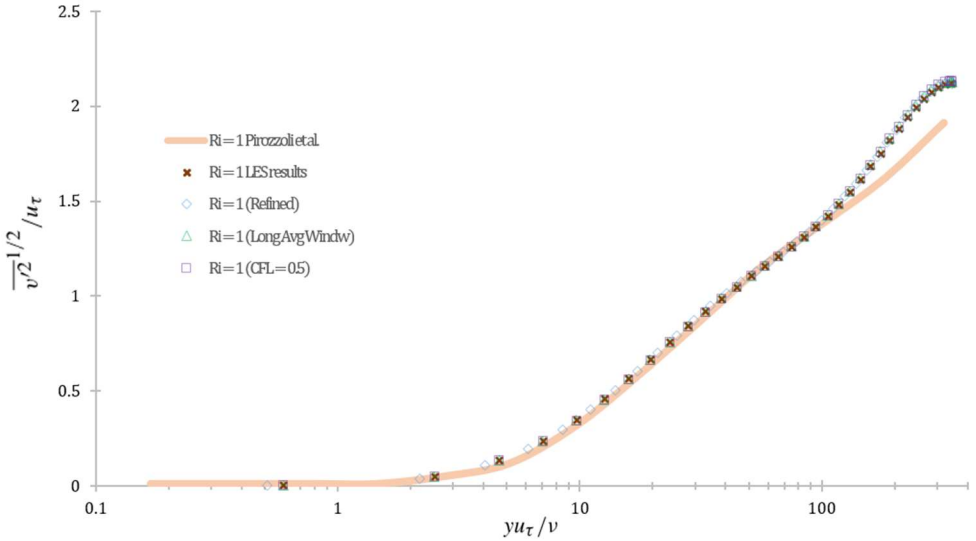


Figure 37: Shear-scaled vertical velocity fluctuations for Ri = 1, assessing the potential effect of mesh refinement, increase of averaging window, and reduction of target CFL.

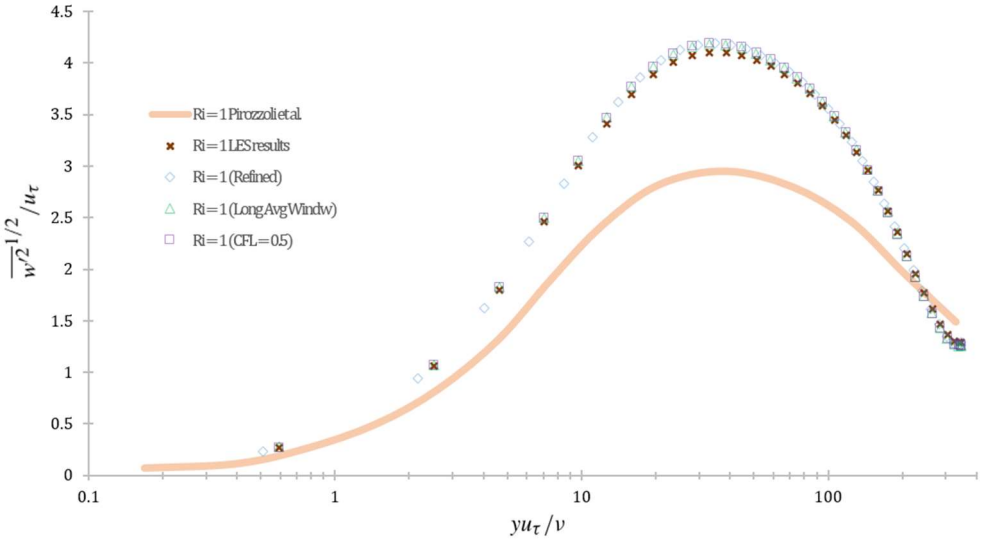


Figure 38: Shear-scaled spanwise velocity fluctuations for Ri = 1, assessing the potential effect of mesh refinement, increase of averaging window, and reduction of target CFL.

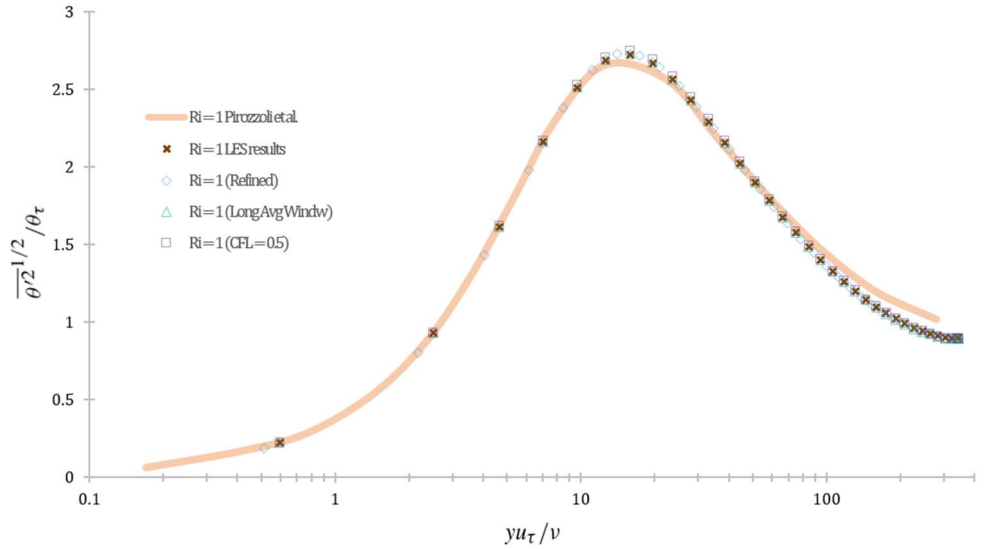


Figure 39: Shear-scaled temperature fluctuations for Ri = 1, assessing the potential effect of mesh refinement, increase of averaging window, and reduction of target CFL.

In conclusion, the results shown in figures 34-39 prove that our simulation does not have any problem due to the time step, nor the flow development, the averaging window or the mesh resolution. Therefore, it validates that our simulation settings are correct.

The only remaining possible settings of the simulation that one could guess could be responsible for the mismatch with Pirozzoli et al. (2017) [16] are the filtering settings, which represent the main drawback of not resolving all the turbulent scales and relying on sub-grid scale models. This was one of the first hypothesis that were considered, when the LES results were obtained, due to the fact that there seemed to be an accumulation of turbulent kinetic energy in the vicinity of the centreline, which could be an indication of an insufficient energy drain from our sub-grid scale model. However, as a result of the series of tests conducted on the $Ri = 1$ case, we could see how the use of a DNS-

resolution mesh produced the exact same result as our LES mesh, which is a solid proof that the SGS modelling of our LES should not be responsible for the mismatch.

Therefore, we can conclude that the reason of the mismatch with Pirozzoli et al. (2017) results is not clear despite the fact that a thorough testing has been conducted giving a solid degree of reliability to our results.

Finally, figures 40-42 provide a qualitative comparison against the results from Pirozzoli et al. (2017) that were introduced in figure 25. Instantaneous vertical (wall-normal) velocity fluctuations (v') and temperature fluctuations (θ') are shown for $Ri = 0.01$, 1 and 10, at the channel centre plane ($y = h$).

The field on the top of each set of figures corresponds to the one reported by Pirozzoli et al. (2017), being followed bellow by 5 instantaneous captures from our LES results, taken at every 1/5 of the averaging window. It was necessary to provide several instantaneous captures to have a meaningful comparison, due to the fact that the reported result from the reference consisted of only one single instantaneous caption.

From observation of the results, it is clear that the flow features are perfectly matched when comparing our LES results to the DNS reference data. For a physical description of each case, refer to section 4.2.1.

Overall, we can conclude that this chapter successfully validated the flow solver and the used settings for the simulation of non-isothermal turbulent flows by comparing against the Pirozzoli et al. (2017) DNS results. Moreover, it has also been confirmed that there is a specific range of unstable stratification conditions for which the coupling between temperature and wall-normal velocity fluctuations ends up feeding the formation of large-scale rolls, in the same manner as observed by Jayaraman & Brasseur (2021) [4] for the ABL.

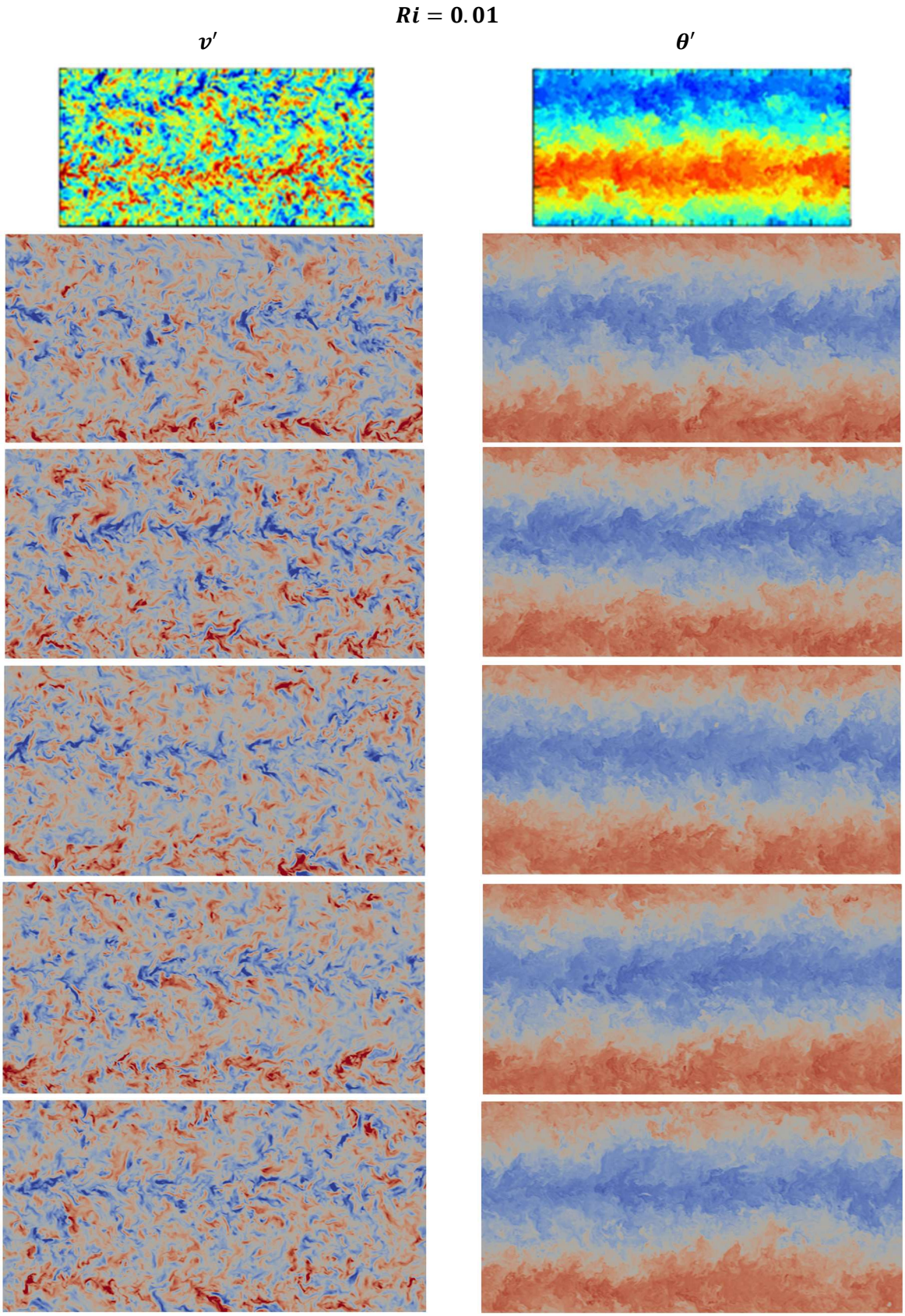


Figure 40: Instantaneous vertical (wall-normal) velocity fluctuations (left column) and temperature fluctuations (right column) at the channel centre for Ri = 0.01 case. Above: result from Pirozzoli et al. (2017), below: instantaneous capture at every 1/5 of the averaging window. The contour plots show 24 contour levels representing each variable on a range of ±3 standard deviations from its mean value, being negative values blue and positive values red.

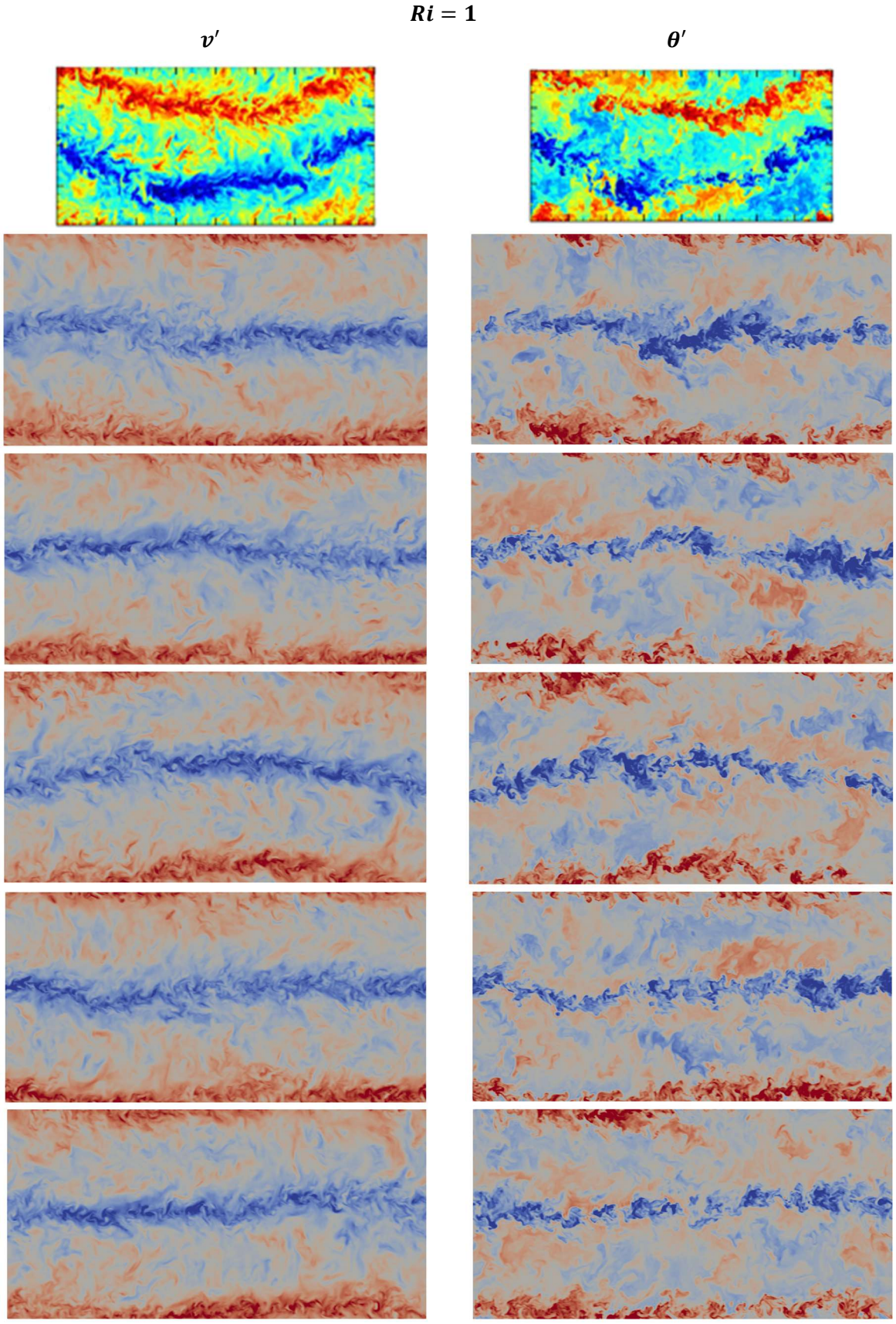


Figure 41: Instantaneous vertical (wall-normal) velocity fluctuations (left column) and temperature fluctuations (right column) at the channel centre for Ri = 1 case. Above: result from Pirozzoli et al. (2017), below: instantaneous capture at every 1/5 of the averaging window. The contour plots show 24 contour levels representing each variable on a range of ±3 standard deviations from its mean value, being negative values blue and positive values red.

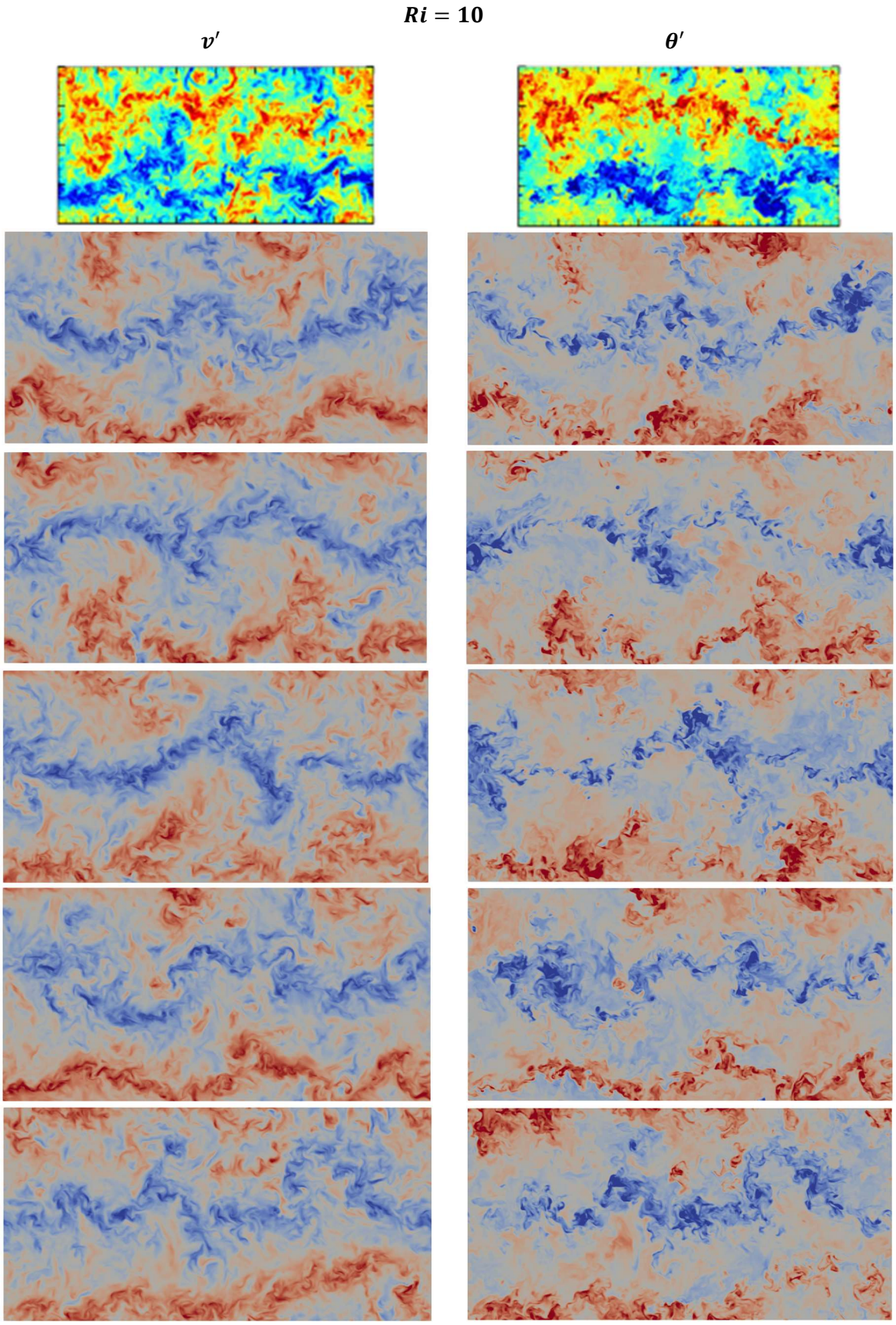


Figure 42: Instantaneous vertical (wall-normal) velocity fluctuations (left column) and temperature fluctuations (right column) at the channel centre for Ri = 10 case. Above: result from Pirozzoli et al. (2017), below: instantaneous capture at every 1/5 of the averaging window. The contour plots show 24 contour levels representing each variable on a range of ±3 standard deviations from its mean value, being negative values blue and positive values red.

Chapter 5

Surface-Mounted Cube Validation

5.1 Introduction

So far, our validation process has allowed us to confirm that the settings and usage of Nek5000 are correct for simulation of non-isothermal wall-bounded turbulence. In the last validation stage, we want to quantitatively verify that the code and settings are also appropriate for our geometry of study, which consists of a so-called surface-mounted cube. In addition, this validation work will serve to validate the computational mesh that will be used for the final study case presented in Chapter 6.

In this regard, Haering et al. (2021) [17] conducted very accurate DNS simulations of a surface-mounted cube subjected to two very different laminar inflow conditions: a Blasius boundary layer profile with $\delta_{99} = 2H$ - where H is the cube height - (case A), and a Blasius profile with $\delta_{99} = 0.25H$ (case B). The authors selected these two cases, because a case where the cube is immersed in the boundary layer (case A), and a case where the cube extends through the boundary layer (case B), represent the limiting cases that an obstacle can experience, being a highly sheared inflow (case A) and an almost uniform inflow (case B).

The geometry studied by Haering et al. [17] consisted of a cube of dimension $H = 1$ mounted on a smooth no-slip surface contained in a box of size $(7.5 \times 3.0 \times 2.0)H$, allowing for a wake length of $4.5H$. Periodic boundary conditions where used on the lateral sides, while a free-slip condition was imposed on the top of the domain and zero pressure gradient at the outflow. The domain was discretized using approximately 240K 9th order spectral elements, as shown in figure 43, ensuring that all dissipative scales were resolved.

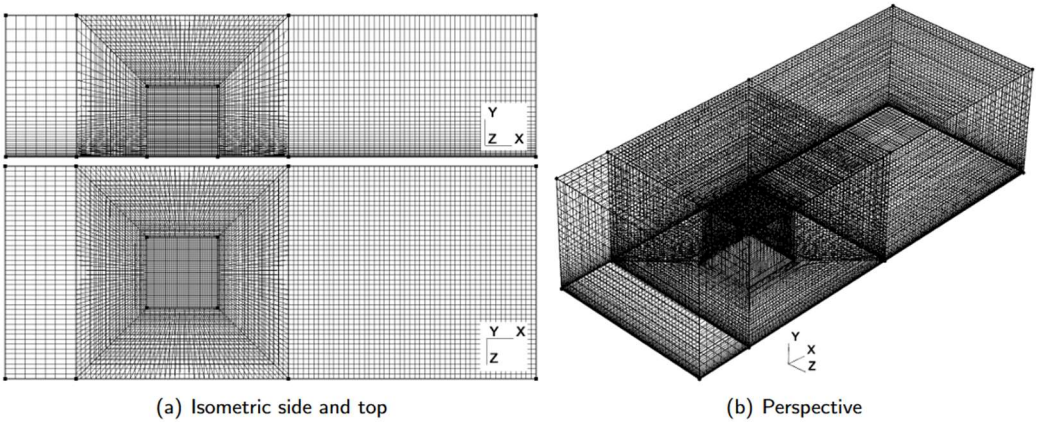


Figure 43: Discretization of the studied geometry, from Haering et al. [17].

The simulations were performed in the range of Reynolds numbers $\gtrsim 3{,}000$, where it has been observed that most of the large-scale flow characteristics are largely Reynolds-independent [35]–[37]. The flow conditions of the two studied cases are characterized by the Reynolds number, based on the cube height H and the inflow velocity at $y = H$, namely Re_{u_h}. Then, for case A: $Re_{u_h} = 2929.7$, and for case B: $Re_{u_h} = 3900$. The knowledge that the large-scale flow characteristics become qualitatively similar, from $Re_{u_h} \gtrsim 3{,}000$ on, is very interesting because it allows us to extrapolate the conclusions to real atmospheric flows, whose actual Reynolds numbers are much larger.

The work by Haering et al. (2021) [17] provided accurate results describing qualitatively and quantitatively the mean-flow and the turbulence. Among their results, the present work will focus on evaluating the matching of the results presented in figures 44-49.

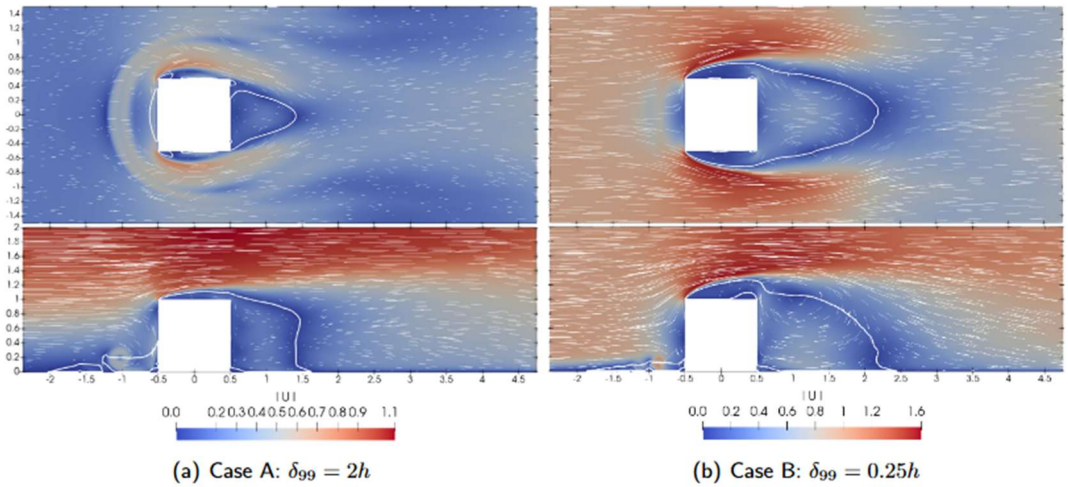


Figure 44: Time-average velocity magnitudes at a spanwise plane of y = 0.25 (top) and vertical plane z = 0 (bottom) for both cases. Solid white line corresponds to u = 0 and highlights the recirculation region. White dashes represent velocity field. From Haering et al. [17].

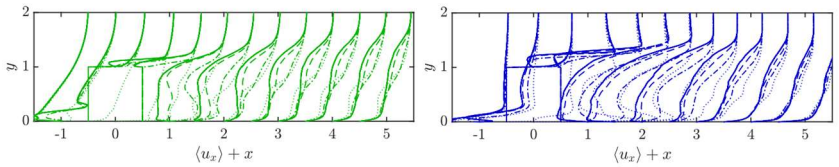


Figure 45: Time-average streamwise velocity profiles at streamwise increments of 0.5H along spanwise planes of 0.0H (–), 0.25H (––), 0.5H (–·), 0.75H (···) offset from the centre of the cube. From Haering et al. [17].

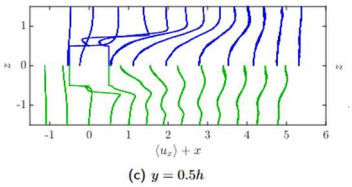


Figure 46: Time-average streamwise velocity profiles at vertical plane y = 0.5H. Case A (green), case B (blue). From Haering et al. [17].

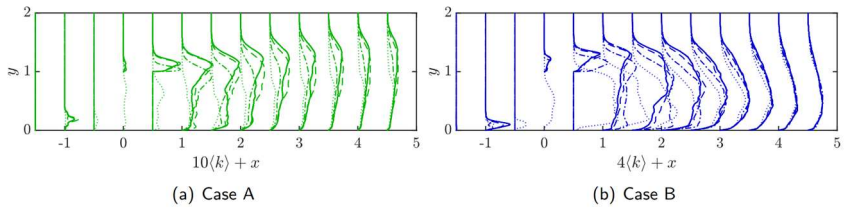


Figure 47: Time-average turbulent kinetic energy profiles at streamwise increments of 0.5H along spanwise planes of 0.0H (–), 0.25H (––), 0.5H (–·), 0.75H (···) offset from the centre of the cube. From Haering et al. [17].

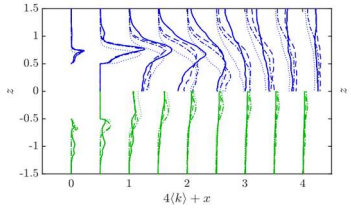


Figure 48: Time-average turbulent kinetic energy at different vertical planes. Case A (green), case B (blue). From Haering et al. [17].

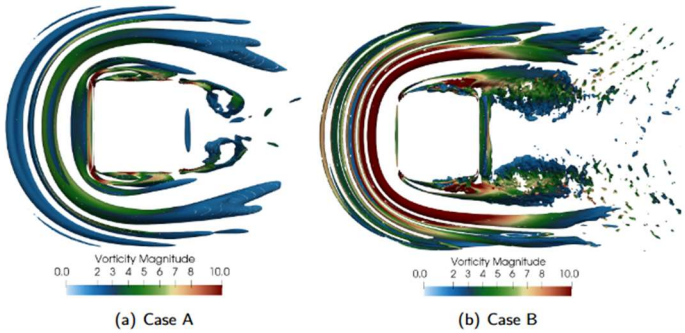


Figure 49: Horseshoe vortex system shown by Q-criterion iso-surface (=0.5) coloured by the vorticity magnitude. Displayed from bottom looking up over a thin slab of 0.25H. From Haering et al. [17].

One has to bear in mind that the main purpose of the present work is to study whether or not the rolls behind a surface-mounted cube under certain stratification conditions show a similar behaviour as was observed by Jayaraman & Brasseur (2021) [4] for a smooth wall. As introduced in Chapter 1, they found that for a certain range of weakly unstable stratification the large-scale rolls of the ABL were strengthened by collecting small-scale plumes.

It is clear that those roll structures belong to large-scale flow features and, as a matter of fact, they were studied by Jayaraman & Brasseur using Large Eddy Simulations, which supports our choice of using LES instead of fully-resolved DNS. Moreover, there is a significant difference between the large-scale structures in a turbulent boundary layer and the rolls that develop behind a surface-mounted cube, the former being a feature of turbulence, while the later are a feature of the mean-flow. This is another reason supporting the idea that we should be able to properly simulate the rolls downstream

of a cube using LES. Furthermore, using Large Eddy Simulation will imply a much lower computational cost, compared to a DNS resolution.

However, it is important to mention that the fact that the roll structures behind the cube may be different in nature (i.e. mean-flow feature) does not prevent them from behaving similarly and strengthening themselves by the same mechanism as the large-scale atmospheric rolls.

In the following subsections of this chapter the work conducted in order to validate our settings and our mesh against Haering et al. [17] results will be described.

5.2 Governing Equations

As previously introduced in section 3.2, Nek5000 spectrally solves the Conservative Form of the Incompressible Navier-Stokes Equations (Momentum and Mass conservation), for constant fluid viscosity and density:

$$\rho\left(\frac{\partial \boldsymbol{u}}{\partial t} + \nabla \cdot (\boldsymbol{u}\boldsymbol{u})\right) = -\nabla p + \mu \nabla^2 \boldsymbol{u} + \rho \boldsymbol{f}$$

$$\nabla \cdot \boldsymbol{u} = 0$$

Since the simulations for this chapter are isothermal, there is no need to solve the Energy Equation.

Finally, the energy drain to model sub-grid scales dissipation is achieved by applying the Explicit Filter [23] introduced in section 3.3.

5.3 Domain Discretization - Mesh

The mesh used by Haering et al. [17] (figure 43) consisted of 240K 9^{th} order spectral elements in a significantly computationally demanding DNS simulation. However, in our LES simulation we do not intend to resolve up to the smallest scales, therefore we can afford discretizing our domain using approximately 10.2K 8^{th} order spectral elements instead. Figures 50-51 show several views of the LES mesh built with ICEM CFD for the simulation of the surface-mounted cube.

Regarding the mesh topology, most of the blocks consisted of H-type blocks, except for the region surrounding the unit cube which has been discretized using O-type blocks. This choice is made to optimize performance, allowing for local refinement and avoids having too small cells in high velocity regions, which would have been the case if all the blocks had been H-blocks, and which would have forced us to decrease considerably the time step in order to have the desired CFL, consequently increasing the computational cost.

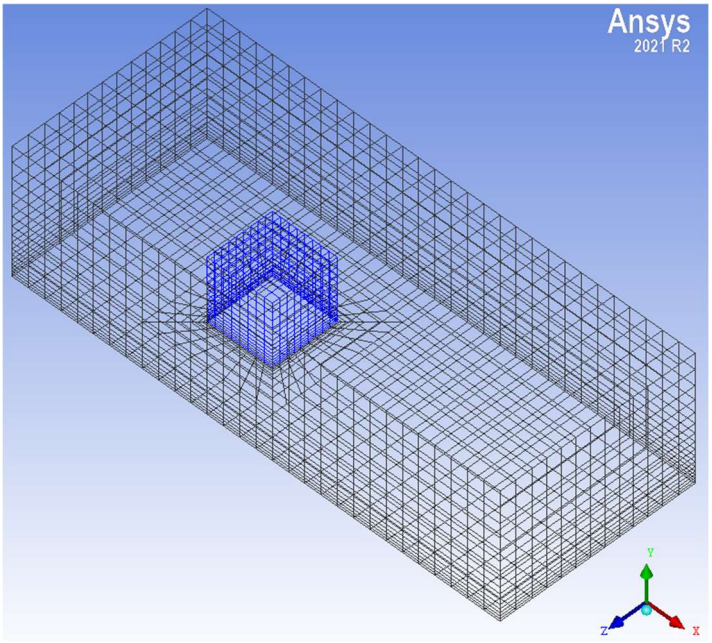


Figure 50: Isometric view of the surface ICEM-generated mesh.

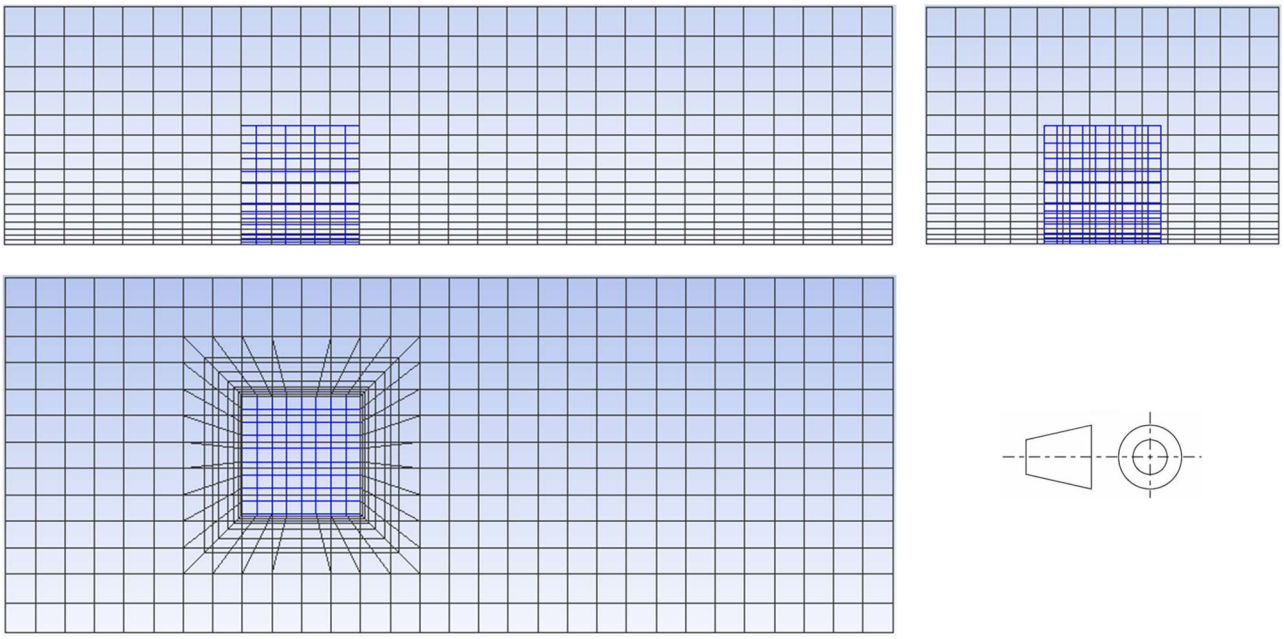


Figure 51: First-angle projection of the surface ICEM-generated mesh.

In a similar fashion as in the previous simulations, the reference mesh resolution guidelines used are those by Negi et al. [29], where they performed a detailed validation work on turbulent boundary layers over wings using Nek5000 and established guidelines for a so-called well-resolved LES simulation. Their guidelines dictate that the resolution at walls should satisfy:

$$\Delta y_w^+ < 1\ ;\ \Delta x^+ < 20\ ;\ \Delta z^+ < 9$$

While the resolution at the wake of an obstacle should satisfy:

$$\frac{\Delta_{cell}}{\eta} < 9$$

Where the Kolmogorov length-scale is defined as:

$$\eta = \left(\frac{\nu^3}{\varepsilon}\right)^{1/4}$$

Where:

$$\nu = \frac{\mu}{\rho}$$

$$\Delta_{cell}, \qquad is\ the\ local\ cubic\ root\ of\ the\ cell\ volume$$

Those guidelines provide a reliable reference on the required resolution for our case of study and they have already been used in LES works similar to the present one, such as Stuck et al. 2021 [38]. However, in our engineering trade between accuracy and speed, we shall discuss whether or not some of the criteria can been made more permissive.

First of all, as introduced in Chapter 2, it is known that most of the dissipation usually occurs at scales above the Kolmogorov length-scale, and that attempting to resolve close to, or up to the Kolmogorov length-scale, may be a bit too strict [18]. For instance, for a curved channel, most of the dissipation has already taken place at scales greater than $15\ \eta$ [19]. Therefore, it is reasonable to say that we can use: $\Delta_{cell}/\eta < 15$ as our resolution criterion in the wake of the obstacle. Especially, taking into account that we are performing an LES simulation with sub-grid scale effects being modelled.

Finally, some of the wall-resolution criteria have been made more permissive to keep computational cost reasonable. Figure 52 and table 7 summarize the used resolution, which approximately satisfies the guidelines stated by Negi et al. It has to be mentioned that the used resolution is already a very good resolution for an LES in Spectral Element Method, which could be very close to an actual DNS.

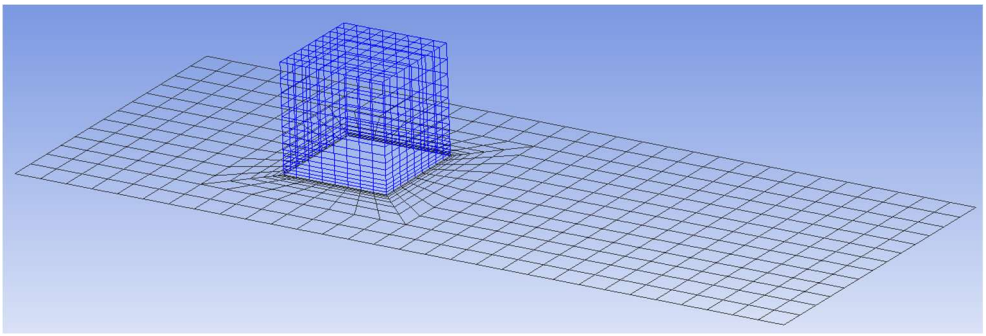


Figure 52: Surface mesh of the wall-type boundaries, showing bottom wall and cube.

$\Delta y_w^+ < 1$
$\Delta x^+ < 23$
$\Delta z^+ < 23$
$\frac{\Delta_{cell}}{\eta} < 15$

Table 7: Mesh resolution.

5.4 Boundary Conditions

As previously stated, the inflow profiles were Blasius profiles. To do so, some routines from the Nek5000 example case "*Blasius*" have been adapted to provide the adequate inflow for each of the cases, which are illustrated in figure 53.

$Case\ A \rightarrow \delta_{99} = 2H$	$Case\ B \rightarrow \delta_{99} = 0.25H$

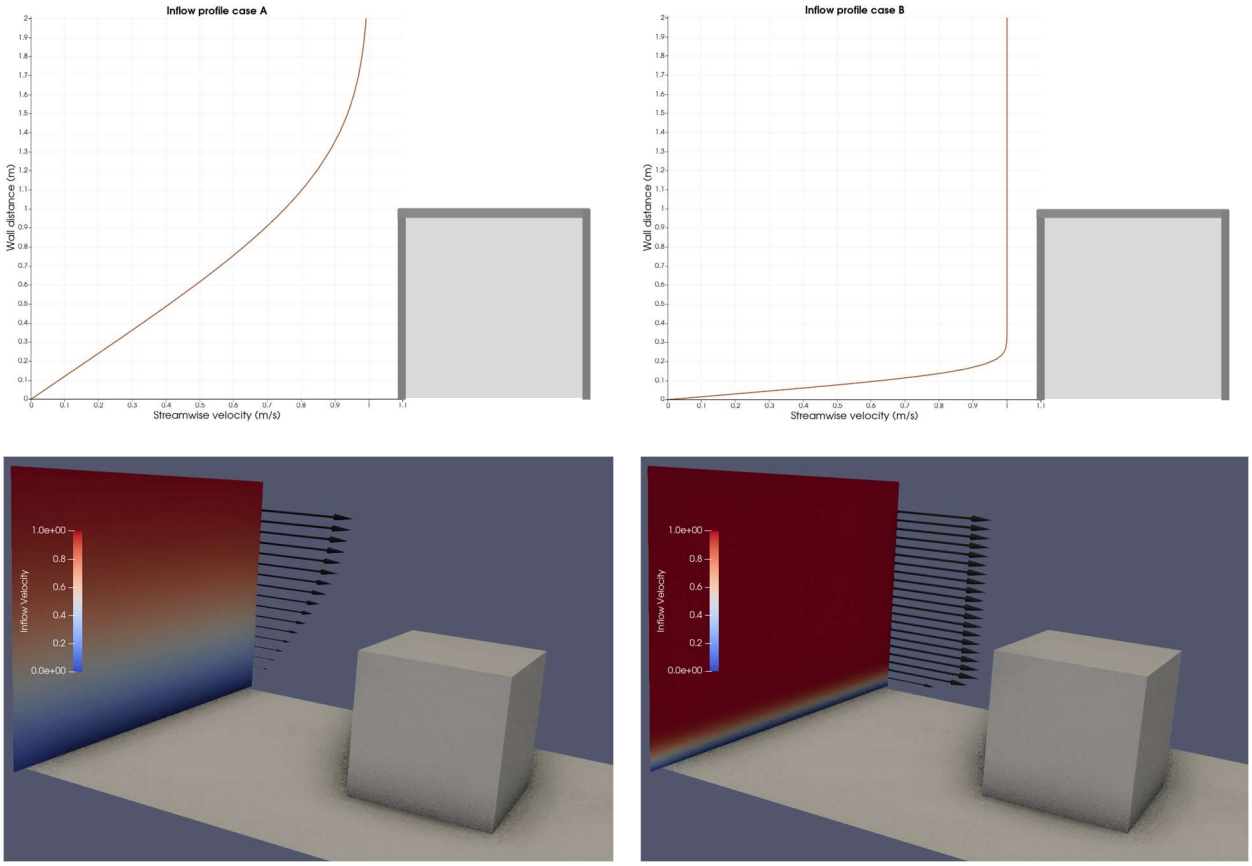


Figure 53: Illustration of the two different inflow conditions.

Due to the large disparity of inflow conditions among the existing works regarding a surface-mounted cube in the literature, using a single Reynolds number definition to describe the flow condition may be misleading. Using as length-scale the cube height (H), the Reynolds number is sometimes based on: 1) the maximum inlet velocity, 2) the velocity at the cube height of the inflow, or 3) the inflow bulk velocity.

In this regard, the work by Haering et al. used for both case A and case B, the same Reynolds number based on the cube height and the maximum inflow velocity, which we will call the $Re_{u_{max}}$, being $Re_{u_{max}} = 3900$.

$$Re_{u_{max}} = \frac{\rho\, U_{MaxInflow}\, H_{cube}}{\mu} = \left(\frac{UL}{\nu}\right) = 3900$$

From this, we set up the parameters of our non-dimensional simulation to match their flow conditions, yielding to a value of dynamic viscosity to be used in both cases of $\mu = 0.00\overline{025641}\ \left[\frac{kg}{m \cdot s}\right]$, while setting density $\rho = 1.0\,\frac{kg}{m^3}$.

$$\mu = \frac{\rho\, U_{MaxInflow}\, H_{cube}}{Re_{max}} = \frac{(1)\,(1)\,(1)}{(3900)} = 0.00\overline{025641}\ \left[\frac{kg}{m \cdot s}\right]$$

This value of the dynamic viscosity was used for both, case A and case B, being the only difference between the two cases the boundary layer thickness of the imposed Blasius profile, being $\delta_{99} = 2H$ for case A, and $\delta_{99} = 0.25H$ for case B. From this, the different Reynolds number definitions can be summarized as in table 8.

$Case\ A \rightarrow \delta_{99} = 2H$	$Case\ B \rightarrow \delta_{99} = 0.25H$
$Re_{max} = \frac{\rho\, U_{Max_Inflow}\, H_{cube}}{\mu} = 3900$ $where: \quad U_{Max_{Inflow}}(y = 2) \cong 1.0$	$Re_{ma} = \frac{\rho\, U_{Max_Inflow}\, H_{cube}}{\mu} = 3900$ $where: \quad U_{Max_{Inflow}}(y = 2) = 1.0$
$Re_{bulk} = \frac{\rho\, U_{Bulk_{Inflow}}\, H_{cube}}{\mu} = 2559.6$ $where: \quad U_{Bulk_{Inflow}} = 0.656319$	$Re_{bulk} = \frac{\rho\, U_{Bulk_{Inflow}}\, H_{cube}}{\mu} = 3730$ $where: \quad U_{Bulk_{Inflow}} = 0.956429$
$Re_{u_h} = \frac{\rho\, U_{Inflow_at_H}\, H_{cube}}{\mu} = 2929.7$ $where: \quad U_{Inflow_{@H}}(y = H) = 0.751216$	$Re_{u_h} = \frac{\rho\, U_{Inflow_at_H}\, H_{cube}}{\mu} = 3900$ $where: \quad U_{Inflow_{@H}}(y = H) = 1.0$

Table 8: Values of the different Reynolds number definitions that are commonly used in literature, for our two study cases.

The zero pressure gradient outflow boundary conditions in turbulent flows comes with the challenge that, especially for such a small domain as ours where the cube is quite close to the outlet, there can be inflow at the outlet, which would cause a sudden increase on divergence and consequent crash of the run. To avoid this, the implemented *turb_outflow* outlet treatment in Nek5000 has been used, which uses a convective speed to adjust the divergence at the outlet region making sure there is no inflow. This effectively accelerates the flow at the outlet and therefore, in our analysis of the results we should bear in mind that the results from the region near the outlet can be affected by this artificial outlet treatment.

5.5 Numerical Scheme

Regarding the numerical scheme and running settings, a 2nd order backward differences scheme, together with operator-integration factor scheme (OIFS) extrapolation, has been used for the time stepping. Such combination on Nek5000 usually allows to use up to $CFL = 5$ without any stability issues [31], for the most simple flow geometries. However, for our more complex surface-mounted cube geometry, our time-step independency study has determined that we must keep our CFL below 1.5. While the simulation was initialized using variable time-step fixing a target CFL, once the flow was fully developed, a constant time step has been used in order to increase the accuracy of the averaging.

5.6 Simulation set up considerations

Regarding the simulation time, there are two main factors that are determinant: 1) the time needed to get a statistically steady state, and 2) the required averaging window to be able to capture the statistics that properly characterize the mean flow.

The first has been taken care of by monitoring the horizontal component of the drag force over the cube and the floor and making sure it stabilizes fluctuating around a mean value, which ensures that the flow was fully developed. Figure 54 shows the drag force signal for the two cases of study over a time span equal to two times the used averaging window for statistics calculation, once the flow field was already fully developed and right before recording our statistics.

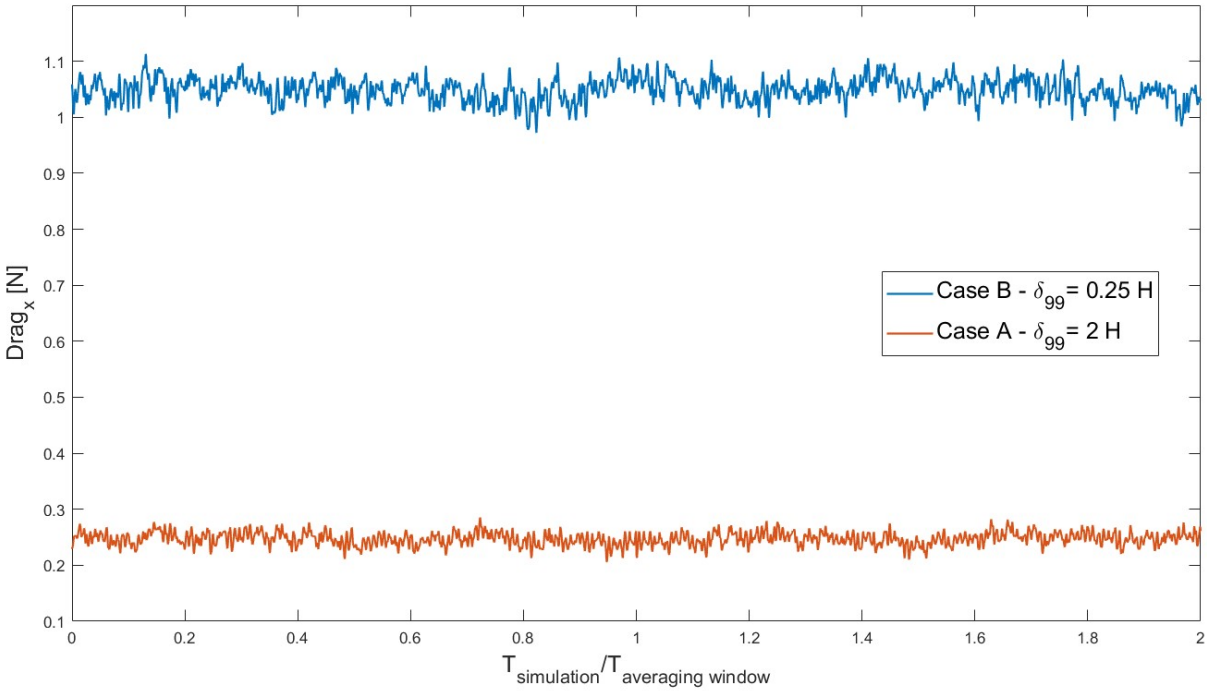


Figure 54: Time-evolution of the horizontal component of the drag force on geometry walls. Time is normalized by the used averaging window since both simulations had different time requirements.

Regarding the later, commonly used guidelines are available in literature. First of all, the needed averaging window can be characterized in terms of a relevant time-scale for the flow developing over the surface mounted cube, which can be defined based on the cube height and the bulk flow velocity and is commonly known in literature as "*convective time*".

$$t_{convective} = \frac{H_{cube}}{U_{bulk}}$$

In this regard, according to Haering et al. [17], in simulations without homogeneous directions, local averaging should be performed over a period exceeding 100 convective times for bluff body flows, as proven by Rodi et al. (1997) [37], where different averaging times ranging from 10 to 200 convective times where studied. In consequence, the present work will take the average of our statistics over 200 convective times, which is definitely on the safe side and will ensure the proper capture of statistics as well as symmetry of the results.

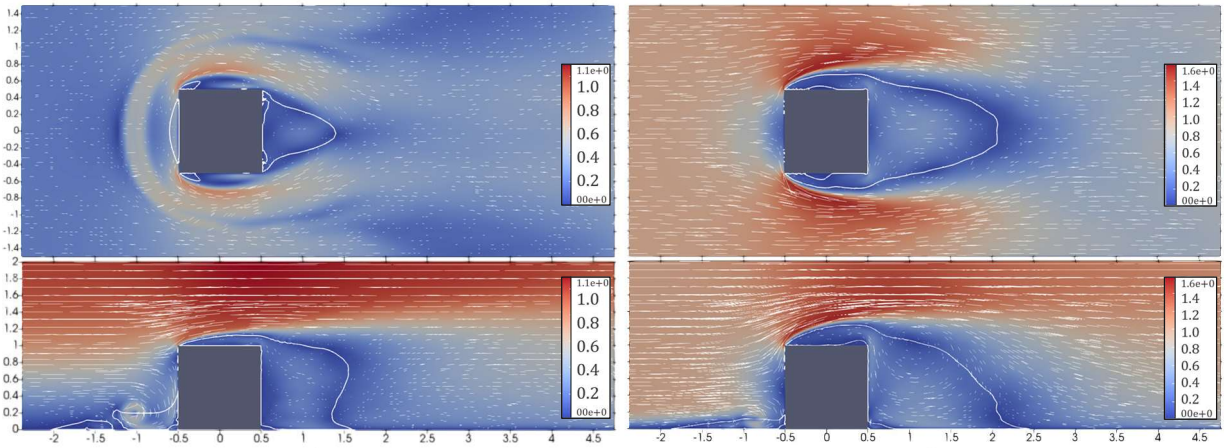
As it can be seen in table 9, for the $\delta_{99} = 2H$ case, a convective time corresponds to 1.524 seconds of simulation time, meaning that if we want to allow for 200 convective times we need to perform the averaging over 302.5 seconds of simulation. Whereas, for the $\delta_{99} = 0.25H$ case, a convective time corresponds to 1.045 seconds of simulation, which requires us to perform the averaging over 209.6 seconds of simulation.

	$U_{Bulk_{Inflow}}$	$t_{convective} = \frac{H_{cube}}{U_{bulk}}$	*averaging window in seconds of simulation*
$Case\ A \rightarrow \delta_{99} = 2H$	0.656319	1.524 s	302.5 s
$Case\ B \rightarrow \delta_{99} = 0.25H$	0.956429	1.045 s	209.6 s

Table 9: Averaging window requirements of the simulations.

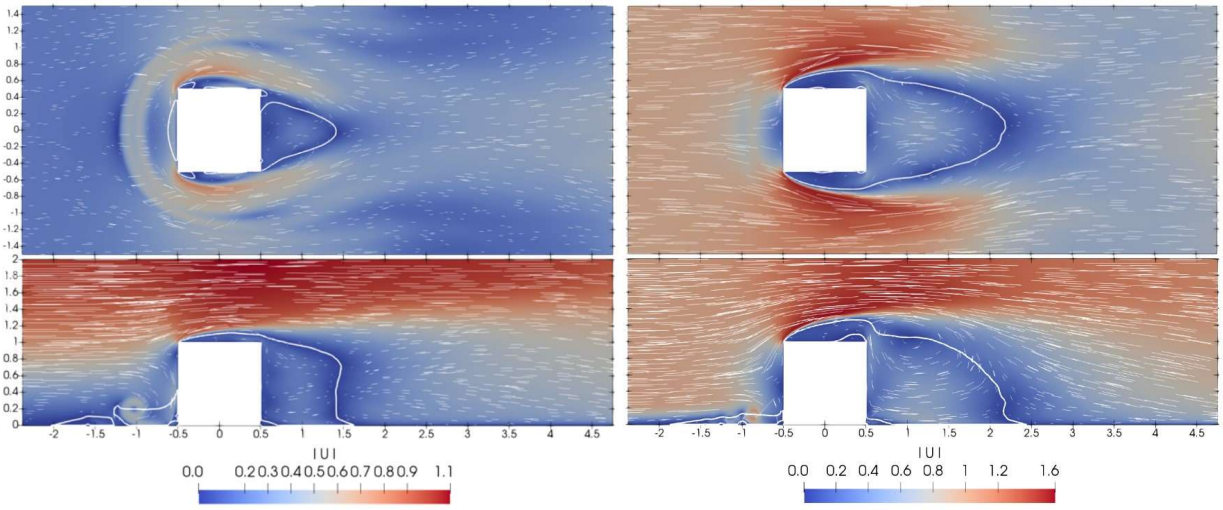
5.7 Results and Discussion

Figure 55 bellow, shows the results obtained for the mean flow for comparison against the reference results in figure 56 (introduced before as figure 44, repeated to allow side by side comparison).



Case A: $\delta_{99} = 2\ H$ Case B: $\delta_{99} = 0.25\ H$

Figure 55: Time-averaged results of velocity magnitude at a spanwise plane of y = 0.25 (top) and vertical plane z = 0 (bottom) for both studied cases. White solid line (indicating u = 0) highlights the recirculation region shape. Velocity field direction indicated by white dashes.



(a) Case A: $\delta_{99} = 2h$ (b) Case B: $\delta_{99} = 0.25h$

Figure 56: Corresponding results reported by Haering et al. (2021).

The velocity contours from figure 55 match all the flow features observed by the reference (figure 56), both in magnitude and direction. Furthermore, the wake reattachment lengths are also matched, occurring at $1.1H$ (case A) and $1.9H$ (case B) downstream from the cube, as observed by Haering et al.

The only significant difference that can be spotted is the fact that our results do show a perfect symmetry of the flow field, while this was not the case for the reference results. The reason for this lies in the fact that, due to the high computational cost of resolving all the turbulence scales, the work by Haering et al. had to limit themselves to a quite short averaging window, being therefore unable to

capture a symmetrically perfect flow field. This is most visible in the not-fully-symmetric recirculation region reported by Haering et al. for case A, whose lowest Reynolds number gives place to low-frequency content that does not seem to have been completely averaged out.

Moreover, figures 57-59 show line plots for the averaged streamwise velocity profiles at different distances downstream, together with the results reported by the DNS reference.

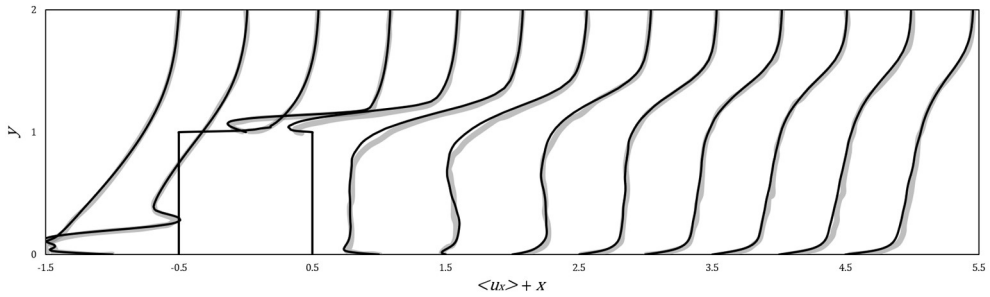


Figure 57: Averaged streamwise velocity (case A: $\delta_{99} = 2H$). Thin black shows LES results, thick grey shows Hearing et al.

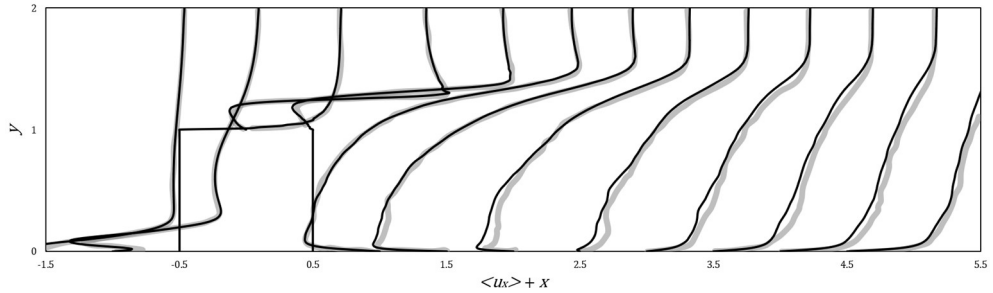


Figure 58: Averaged streamwise velocity (case B: $\delta_{99} = 0.25H$). Thin black shows LES results, thick grey shows Hearing et al.

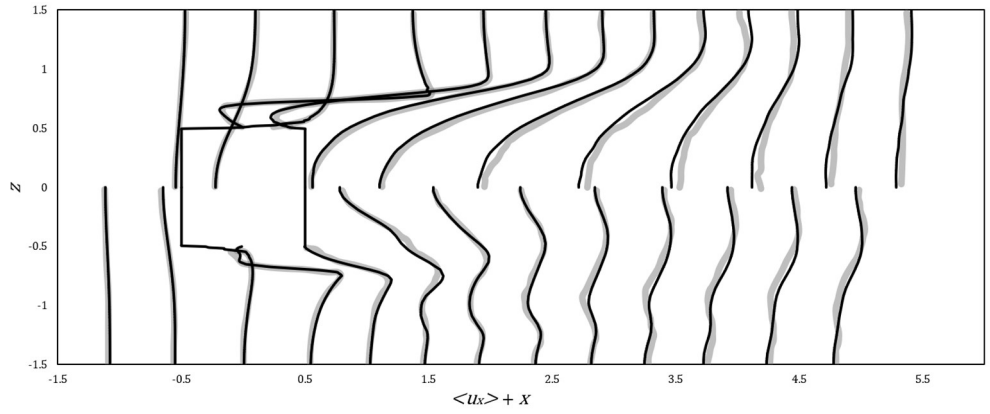


Figure 59: Averaged streamwise velocity on horizontal plane $y = 0.5$. Case A: $\delta_{99} = 2H$ (bottom half), case B: $\delta_{99} = 0.25H$ (top half). Thin black shows LES results, thick grey shows Hearing et al.

The line plots for the time-averaged streamwise velocity show a perfect match with the DNS reference data throughout the entire flow domain. It can be observed that the matching is slightly better for case A ($\delta_{99} = 2H$) than for case B ($\delta_{99} = 0.25H$). This is reasonable since the cube-height-based Reynolds number for the latter is larger**,** increasing turbulence scales separation, while the same mesh resolution was being used. Recall that $Re_{u_h} = 2929.7$ for case A, while $Re_{u_h} = 3900$ for case B, and that the

ratios of the Kolmogorov-scales to the integral-scales scale with the Reynolds number, as introduced in Chapter 2.

Moreover, the results from figures 57 & 58 show that the walls are properly resolved for both cases, which validates once again the adequacy of our mesh. Minor deviations appear in case B in the wake of the cube where, as it will be later on described, turbulence intensity is higher making smaller the small-scales of the flow.

From the Nek function *avg_all( )* and the KTH toolbox *stat.f* and *pstat3D.f* we obtain the average, $\overline{u_i}$, and the variance, $\overline{u_i u_i}$, for the three components of our 3D space. These outputs are enough to reconstruct the Reynolds stresses since, for a sufficiently large averaging window on statistically steady state flow field, the average of the fluctuations equals the variance minus the squared of the mean.

$$\overline{u'u'} = \overline{u\,u} - \bar{u}\,\bar{u}$$

From these results, we can easily obtain the turbulent kinetic energy (TKE) distribution, which is mainly associated to the large scales of turbulence, as the trace (*half*) of the Reynolds stress tensor:

$$k = \frac{1}{2}[\overline{u'u'} + \overline{v'v'} + \overline{w'w'}]$$

Figures 60 & 61 show the turbulent kinetic energy field for case A and case B, respectively:

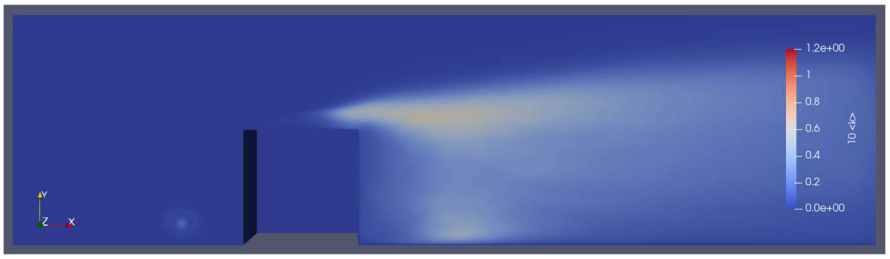


Figure 60: Clip (z = 1.5 plane) - TKE distribution for case A ($\delta_{99} = 2H$).

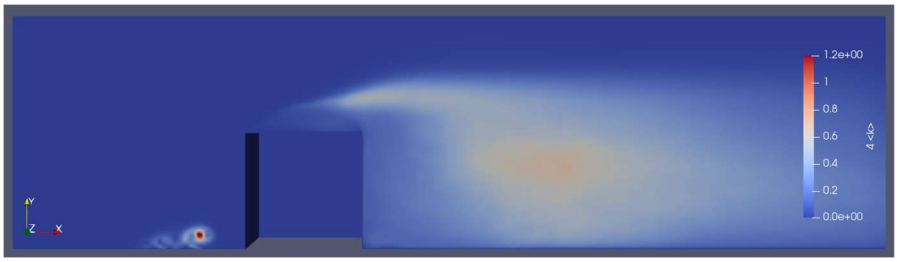


Figure 61: Clip (z = 1.5 plane) - TKE distribution for case B ($\delta_{99} = 0.25H$).

As descriptive as the 2D TKE contour plot can be, we use line plots once again in order to conduct an accurate quantitative validation.

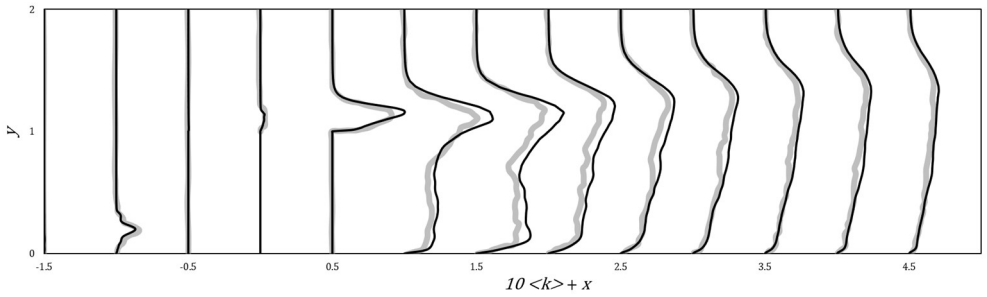


Figure 62: Averaged TKE profiles (case A: $\delta_{99} = 2H$). Thin black shows LES results, thick grey shows Hearing et al.

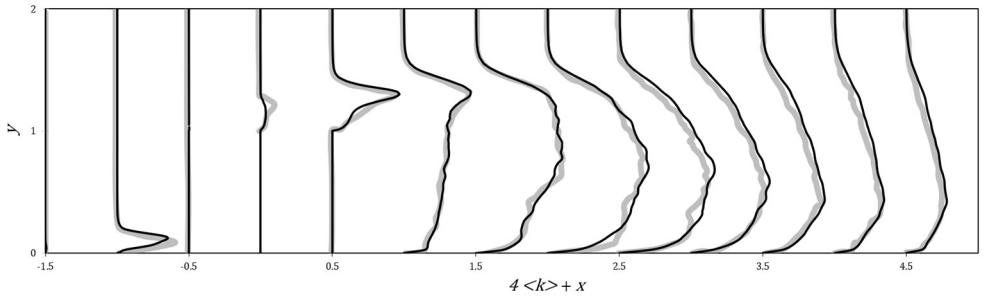


Figure 63: Averaged TKE profiles (case B: $\delta_{99} = 0.25H$). Thin black shows LES results, thick grey shows Hearing et al.

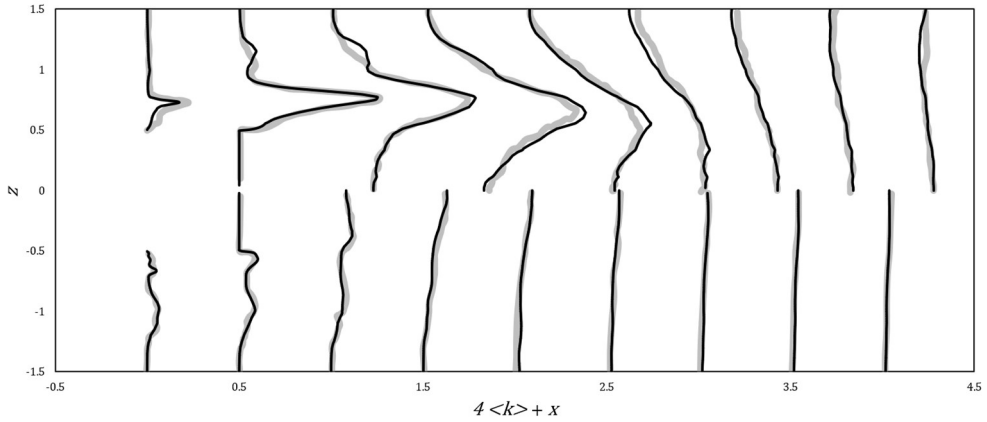


Figure 64: Averaged TKE on horizontal plane $y = 0.25$. Case A: $\delta_{99} = 2H$ (bottom half), case B: $\delta_{99} = 0.25H$ (top half). Thin black shows LES results, thick grey shows Hearing et al.

From figures 62-64, the achieved matching is satisfactory for an LES simulation. As expected for a higher-order statistic, the matching is not as good as the obtained for the mean-flow. However, it can be concluded that both the mean flow and the turbulent kinetic energy are optimally predicted.

It is relevant to mention that, opposed to what we saw for the mean flow profiles, the TKE is better matched in case B rather than in case A. At a first sight this could seem unintuitive, since the Reynolds number was larger in case B. However, it is important to mention that due to the highly different incoming Blasius profiles -being it highly-sheared for case A while near-uniform for case B-, the Reynolds number is not the only difference between the two cases. Therefore, for incoming flows that different in nature, no direct comparisons can be made in terms of the Reynolds number only.

Finally, it is interesting to note that the regions of higher turbulent kinetic energy are also the regions where we observed worse matching of the mean velocity profiles in figures 57-59. As previously hinted

in the discussion of the mean-flow profiles, the reason for this lies on the fact that the dissipation of turbulent kinetic energy (ϵ) scales with the turbulent kinetic energy (k) itself as:

$$\epsilon \sim \frac{U^3}{l} \sim \frac{k^{3/2}}{l}$$

Therefore, from the previously introduced Kolmogorov scales (Chapter 2) we can see that the larger the turbulent kinetic energy is, the smaller the smallest length- and time-scales of the flow will become, challenging our LES simulation.

Up to now, a quantitative validation for the mean flow profile and for the mean distribution of turbulent kinetic energy has been successfully conducted. At this point, the final stage of the validation work will be used to introduce some new concepts and to discuss the importance that vortical structures have for our research work, whose ultimate goal is the study of the dispersion of pollutants in urban environments.

Why are vortical structures important for our ultimate research goals?

Back in 1858, Helmholtz presented a series of theorems for vortex motion [39]. Among his conclusions, particularly from Helmholtz's second theorem, it follows that fluid elements that are part of a vortex line (or tube) will always belong to that same vortex line (or tube), as long as viscosity is negligible. As a direct consequence, any solid particles dispersed within the fluid and behaving as passive scalars will share the same fate. Therefore, most of them will tend to remain trapped inside the vortical structure just like the fluid elements around them, as long as scalar diffusion is negligible. As a result, moving vortices can transport mass, energy and momentum over significantly large distances with very little dispersion, making them an important mechanism for pollutant dispersion that needs to be analysed [40].

In this regard, one of the most commonly used criteria for the visualization of coherent vortical structures is the so-called Q-criterion. Hunt, Wray & Moin (1988) [41] defined "eddy zones" as regions where the second invariant (Q) of the velocity-gradient tensor ($e_{ij} = \partial u_i / \partial x_j$) was positive, i.e. $Q > 0$. Being the second invariant of the velocity-gradient tensor defined as:

$$Q = -\frac{1}{2}\left(\frac{\partial u_i}{\partial x_j}\frac{\partial u_j}{\partial x_i}\right) = \frac{1}{2}(\|\boldsymbol{\Omega}\|^2 - \|\mathbf{S}\|^2)$$

Where:

$$\|\mathbf{S}\| = \sqrt{tr(\boldsymbol{S}\boldsymbol{S}^T)} \qquad \|\boldsymbol{\Omega}\| = \sqrt{tr(\boldsymbol{\Omega}\boldsymbol{\Omega}^T)}$$

$$\boldsymbol{S} = \frac{1}{2}\left(\frac{\partial u_i}{\partial x_j} + \frac{\partial u_j}{\partial x_i}\right) \rightarrow Strain - rate\ tensor \qquad \boldsymbol{\Omega} = \frac{1}{2}\left(\frac{\partial u_i}{\partial x_j} - \frac{\partial u_j}{\partial x_i}\right) \rightarrow Rotation - rate\ tensor$$

$(symmetric\ part\ of\ the\ velocity\ gradient\ tensor)$ $(antisymmetric\ part\ of\ the\ velocity\ gradient\ tensor)$

Therefore, it can be seen that Q represents a local balance between shear strain-rate and vorticity magnitude. As a consequence, the main advantage of using Q-criterion for vortex visualization, instead of just using vorticity magnitude $|\boldsymbol{\omega}|$, lies in the fact that since the vorticity equals the shear-strain at the wall, the Q-value will vanish there [42]. Therefore, by highlighting regions where the vorticity magnitude is greater than the magnitude of the rate of strain, the Q-criterion is effectively removing the wall-shear-induced vorticity while keeping the coherent vortical structures of the flow.

Having introduced the definition and strengths of the Q-criterion for the visualization of vortical structures, the validation stage will be concluded by analysing the mean flow coherent vortical structures present in the surface-mounted cube, as well as comparing with the equivalent results reported by Haering et al. (2021) [17] (figure 65, previously introduced as figure 49, repeated to allow side by side comparison with the LES results shown in figure 66).

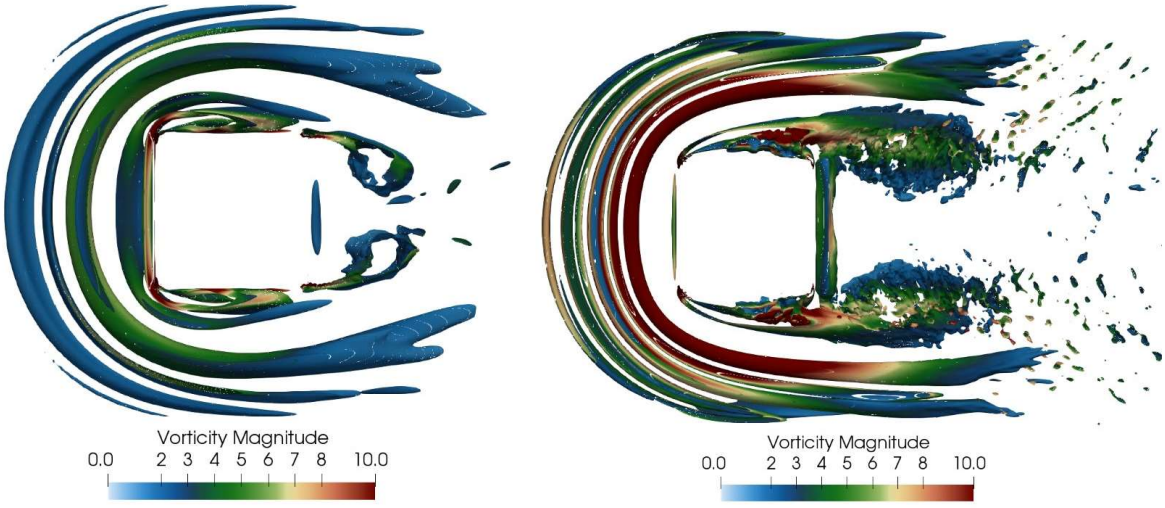


Figure 65: Horseshoe vortex system shown by Q-criterion iso-surface ($= 0.5$) coloured by vorticity magnitude. Displayed from bottom looking up over a thin slab of $\Delta y = 0.25H$. From Haering et al. (2021) [17].

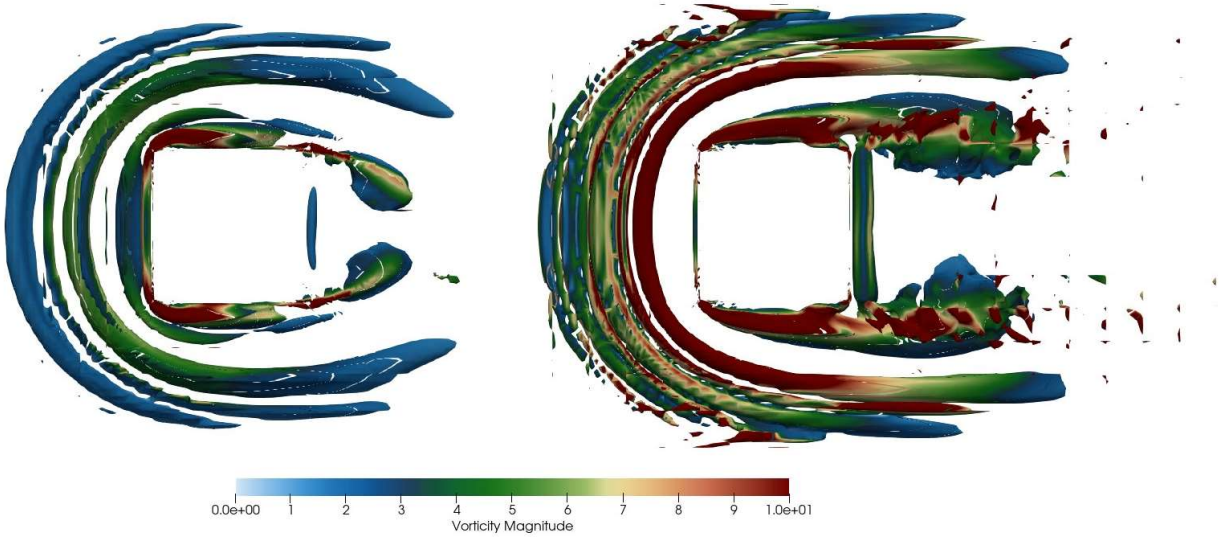


Figure 66: Obtained LES results showing the horseshoe vortex system by Q-criterion iso-surface (=0.5) coloured by vorticity magnitude for comparison against Haering et al. (2021) shown on figure 65.

The flow structure characteristic of flow past a surface-mounted prismatic body usually consists of a system of so-called horseshoe vortices. Such horseshoe vortex system can be quite complex and is composed of one primary and stronger horseshoe vortex, that can be even seen in the mean velocity profiles from figure 55-56, together with secondary vortices. A full view of the complex horseshoe vortex system can only be obtained by plotting iso-surfaces of Q-criterion. In this regard, figure 65-66 show iso-surfaces of $Q - value = 0.5$ coloured by vorticity magnitude for a thin slab of thickness $\Delta y = 0.25H$ (from bottom looking up).

Comparing our LES results (figure 66) with those reported by Haering et al. (figure 65), it is clear that the vortex system is overall properly predicted for both cases. On the other hand, it can be noted that the smallest structures (specially in case B) could not be captured by our LES resolution. However, the large-scale structures, which contain most of the turbulence kinetic energy and are responsible for most of the turbulent transport, are indeed properly matched, both in shape and in magnitude.

From a closer look at figure 66, it can be observed that the primary horseshoe vortex for case B is stronger and thinner as compared to that of case A, as was pointed out by Haering et al. (2021). Furthermore, it can also be seen that the horseshoe vortex system displayed by our LES results matches the number of horseshoe vortices reported by Haering et al. (2021), being it composed of four vortices for case A and seven vortices for case B.

Overall, we can conclude that this chapter successfully validated the flow solver and the used settings for the simulation of an isothermal flow past a surface-mounted cube up to $Re_{u_h} = 3900$, by comparing against Haering et al. (2021) [17] DNS results. Moreover, it also served to introduce the importance of vortical structures in pollutant dispersion, and to validate the used computational mesh that will be used in Chapter 6 of this thesis for the study of the thermal stratification effects on the rolls behind a surface-mounted cube.

Chapter 6

Thermal stratification effects on the rolls behind a high-rise building

6.1 Introduction

As introduced in section 1.5, the purpose of the present research work consists of modelling a high-rise building as a surface-mounted cube in order to study whether the roll structures downstream of the cube show a similar behaviour as the one observed by Jayaraman & Brasseur (2021) for the atmospheric large-scale rolls under weakly unstable stratification conditions [4]. To that end, simulations will be set up under different thermal stratification conditions while vorticity and Q-criterion will be used to assess if the rolls downstream from the cube do strengthen themselves by collecting small-scale plumes.

Note that by "roll structures downstream of the cube" it is meant the counter-rotating streamwise-oriented vortical structures visible at the rightmost part of the sketch from figure 10, which were presented in section 1.5, which are also part of the horseshoe vortex systems studied in Chapter 5.

These roll structures downstream of the cube can be seen in figures 67 & 68, where the mean-flow data from the case B ($\delta_{99} = 0.25H$) simulated in Chapter 5 has been used to show an iso-surface of Q-criterion ($= 0.01$) coloured by the x-component of the vorticity. Such a combination allows to visualize the vortical structures of the mean flow, as well as their sign of rotation. From the image, it is evident the presence of the two counter-rotating rolls in the wake that are characteristic of a surface-mounted cube flow (see figure 10 in section 1.5).

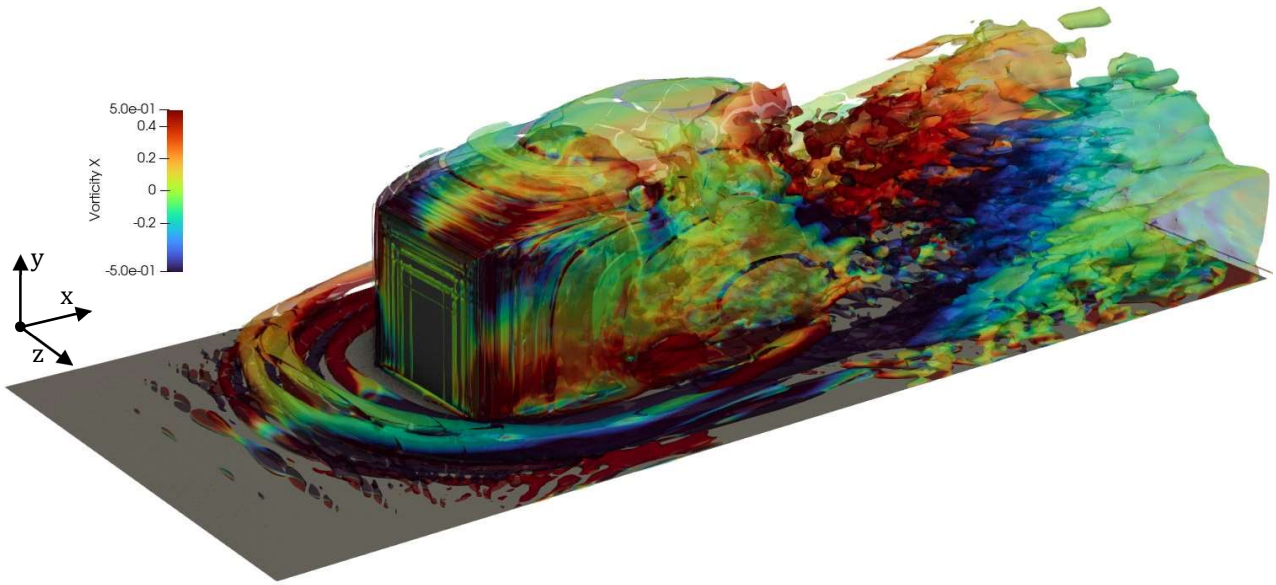


Figure 67: Iso-surface of Q-criterion ($= 0.01$) applied to the averaged flow field for visualization of the vortical structures of the mean-flow around the surface-mounted cube. Colour represents x-vorticity component, showing the sign of rotation.

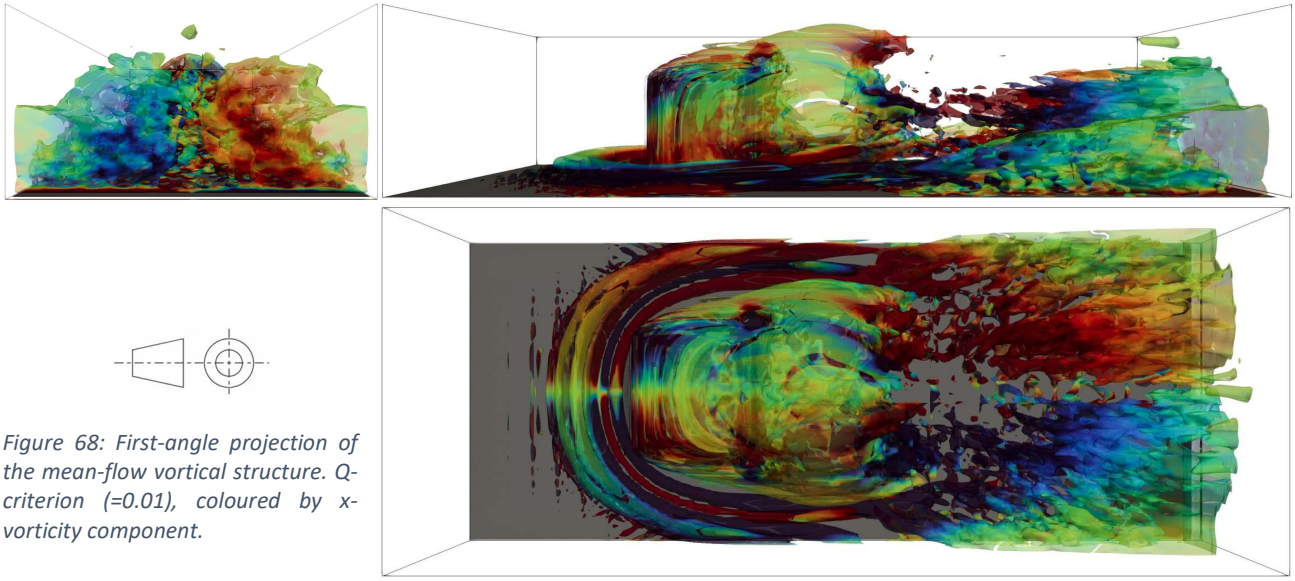


Figure 68: First-angle projection of the mean-flow vortical structure. Q-criterion (=0.01), coloured by x-vorticity component.

The present chapter will describe the setting up of the LES simulation, together with the discussion of the obtained results and the research questions presented in Chapter 1. Due to time constraints, the simulations carried out in this section have been made faster at the expense of accuracy on the results. This has been achieved by increasing the time step up to the maximum allowed to keep the simulation stable, by increasing the residual tolerances, and by reducing time for flow development and averaging windows. As a result, the accuracy of the results is not as good as in the previously presented simulations, but it will be enough to provide with a qualitative proof of concept showing whether or not will we have strengthening of the rolls behind the cube.

The reason for this shortage of time lies in the fact that it has been prioritized to build the most optimal numerical model for our case of study, producing highly accurate results with the minimum computational cost possible. Therefore, much effort has been made to conduct a very rigorous validation process, to obtain an optimal mesh and to determine the most adequate simulation settings and filtering parameters. This gave as a result, a very reliable and accurate model that will allow us to perform many different experiments in future works, in which a wide range of weakly unstable thermal stratification conditions will be tested to fully characterize the behaviour of the rolls behind a high-rise building. Moreover, passive scalars will be added to study what are the consequent effects for pollutant dispersion.

6.2 Governing Equations

The physics that govern the non-isothermal flow past a surface-mounted cube are described by the Incompressible Navier-Stokes Equations (Momentum and Mass conservation), as for the isothermal case from Chapter 5. However, in the current case thermal effects will be present too which, recalling the non-isothermal turbulent channel from Chapter 4, will imply solving the Energy equation for temperature, and modelling buoyancy effects by means of the Boussinesq approximation.

As previously introduced in section 3.2, Nek5000 spectrally solves the Conservative Form of the Incompressible Navier-Stokes Equations (Mass and Momentum conservation), for constant fluid viscosity and density, as well as the Energy Equation:

$$\nabla \cdot \boldsymbol{u} = 0$$

$$\rho\left(\frac{\partial \boldsymbol{u}}{\partial t} + \nabla \cdot (\boldsymbol{u}\boldsymbol{u})\right) = -\nabla p + \mu \nabla^2 \boldsymbol{u} + \rho \boldsymbol{f}$$

$$\rho c_p \left(\frac{\partial T}{\partial t} + \boldsymbol{u} \cdot \nabla T\right) = \nabla \cdot (\lambda \nabla T)$$

> Recall that the buoyancy effects can be modelled by a forcing term ($\boldsymbol{f}$) into the momentum equations defined by the Boussinesq approximation. Refer to section 4.2.3 for a description of the Boussinesq approximation and the methodology for setting up the desired dimensionless numbers in the simulation.

Finally, the energy drain to model sub-grid scales dissipation is achieved by applying the Explicit Filter [23] introduced in section 3.3.

6.3 Domain Discretization - Mesh

The geometry used is based on that from Chapter 5. One has to bear in mind that in a weakly unstable thermal stratification condition, some time and space for development is needed so that we can sense the thermal effects, meaning that the length of the domain needs to be increased.

To that end, based on an educated guess from observing the rolls obtained in Chapter 5, it is decided to increase the streamwise dimension of the domain from $L_x = 7.5H$ to $L_x = 18H$, while keeping the wall-normal and spanwise dimensions used in Chapter 5. It is expected that this length will allow for an entire rotation of the mean-flow rolls during the time it takes for the bulk flow to advect the structures downstream (discussed in section 6.6). Ideally we would probably need an even larger domain, however it has been limited due to computational time constraints. In addition, the proposed domain size should already be enough to get a qualitative proof of concept that allows us to answer our research questions.

Therefore, as shown in figure 69, the geometry consists of a cube of dimension $H = 1$ contained in a box of size $(18.0 \times 3.0 \times 2.0)H$, which allows for a wake length of $12.5H$. The adequacy of this length will be discussed a posteriori in the results section.

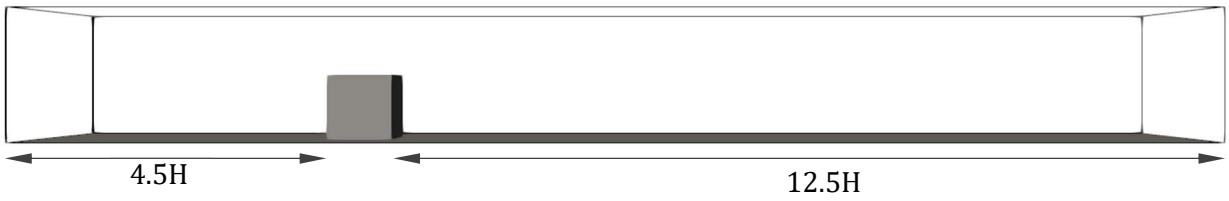


Figure 69: Domain geometry consists of a cube of dimension $H = 1$ contained in a box of size $(18.0 \times 3.0 \times 2.0)H$, which allows for a wake length of $12.5H$.

Regarding the domain discretization, recall that in Chapter 5 we have just validated a computational mesh for simulating flow past a surface-mounted cube up to $Re_{u_h} = 3900$. Therefore, the computational mesh for the current study (figure 70) will be based on the mesh from Chapter 5 (see section 5.3 for detailed description), being the only modification the increase in length of the domain, which was added while keeping exactly the same resolution from Chapter 5 everywhere. For mesh details refer to figure 52 and table 7 from section 5.3.

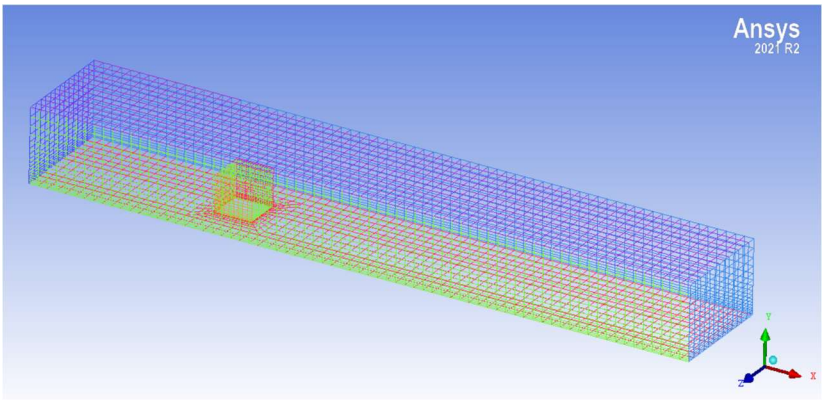


Figure 70: Computational mesh.

6.4 Boundary Conditions

Most of the boundary conditions are just like in Chapter 5. The bottom and cube walls are no-slip, the top wall is free-slip (which makes our flow problem similar to a half-channel, just like in Chapter 5), and the outflow boundary condition is zero pressure gradient ($\frac{\partial p}{\partial x}\Big|_{outlet} = 0$).

The differences appear in the addition of temperature as a flow variable, as well as, in the inflow condition, which in this case needs to be a turbulent inflow.

On one hand, the boundary conditions for the dimensionless temperature are:

$$\theta_{bottom\ wall} = 1.0 \qquad \theta_{top\ wall} = 0 \qquad \frac{\partial \theta}{\partial n}\Big|_{cube\ walls} = 0$$

On the other hand, one of the biggest challenges when it comes to simulate turbulence is generating an adequate inflow condition. Such inflow needs to be time-varying and consist of realistic turbulent structures. To that end, several methods such as precursor simulation, synthesised turbulence and recirculation exist, which, after a certain adaptation length, can end up in physically realistic turbulence.

The present work requires an inflow similar to a turbulent boundary layer of thickness $\delta_{99} = 2H = domain\ height$. Due to the similarity that our building domain has with a half-channel (recall top boundary is free-slip), the natural method to use is precursor simulation running concurrently, in this case a turbulent half-channel flow, which will be used to provide a realistic inflow condition to our building domain.

The precursor simulation consists of concurrently simulating a turbulent half-channel flow (in our case) and using a slice of it to be inputted to the actual domain of interest as inflow condition. This method

is illustrated in figure 71, where the building domain is visible together with the outline of the concurrently running turbulent half-channel domain and the slice of it that will be inputted to the building domain as inflow condition.

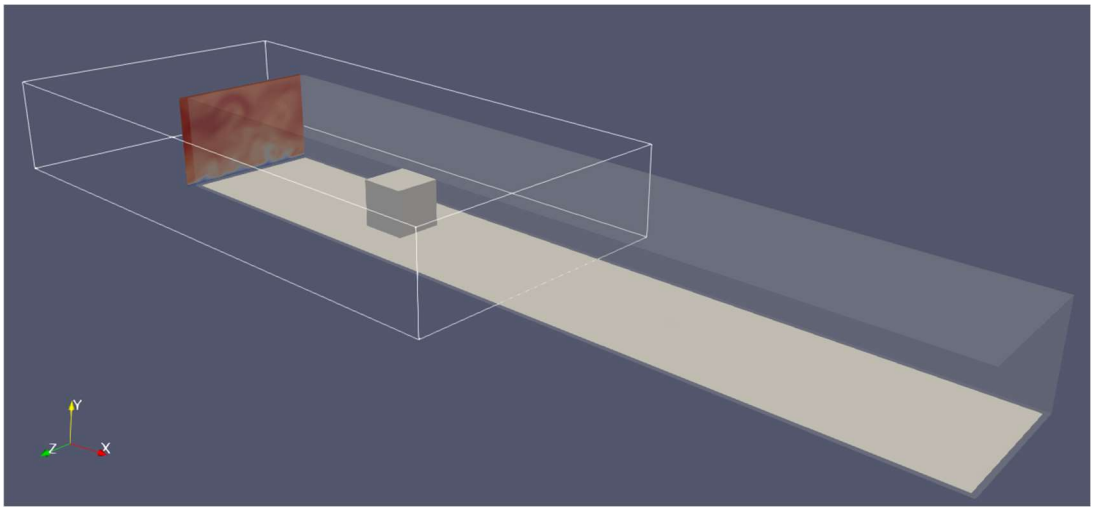


Figure 71: Image to illustrate how the precursor simulation for inflow generation works. Image shows the building domain and the outline of the concurrently running turbulent half-channel domain, together with a slice of instantaneous x-velocity from the half-channel domain that will be inserted into the building domain as inflow condition.

Regarding the implementation of such turbulent inflow generation method in Nek5000, a multidomain simulation is required. Such simulation consists of two unidirectionally-coupled cases: one representing a turbulent half-channel and another being a box which contains a surface-mounted cube. The (unidirectional) link between the turbulent half-channel precursor simulation and the surface-mounted cube domain is set up using the "*neknek_exchange*" subroutine for overlapping grids, which allows for data exchange between the two domains, so that a slice of the turbulent half-channel simulation is extracted and spectrally interpolated to the inlet boundary of the surface-mounted cube mesh, at every time step.

When using a precursor simulation, the user has to distribute the available resources (CPU) between the two concurrent simulations. Such distribution is usually called the CPU-split and can have a big impact on the efficiency of the simulation. The reason lies in the fact that the main simulation requires, at every time step, the input from the concurrently running precursor simulation. The optimal CPU-split is such that it guarantees that the precursor simulation always finishes slightly before the main simulation, so that the main simulation never has to wait, but making sure that it does not finish too much before, which would not be efficient either.

To setup an adequate CPU-split, an educated guess for a test run can be obtained based on the ratio of degrees of freedom between the two simulations. Finally, the computing times of each case can be monitored in Nek5000 by checking the "*multidomain data exchange*" times in the output "*logfile*", and the CPU-split can be adjusted, if needed.

6.5 Simulation set up considerations

In this final stage of the work, two distinct cases will be simulated. On one hand, an isothermal flow case will be computed first and will provide us a reference to compare the non-isothermal case with. Moreover, its results will be used for the setting up of the non-isothermal flow case providing an estimate of the required time for the thermal effects to be present, which is related to the time it takes for the mean-flow rolls to make an entire turn.

On the other hand, regarding the non-isothermal case, in section 1.3.2 we have shown how the instability parameter used by Jayaraman & Brasseur (2021) [4] can be derived from the definition of the Richardson number. Moreover, as introduced in section 1.4.2, Jayaraman & Brasseur (2021) found that the maximally coherent roll state occurred at an instability parameter of $-z_i/L = 1.08$. Therefore, despite the fact that we are dealing with a different problem, our initial guess for a weakly unstable stratification condition for which we expect to see strengthening of the rolls behind a surface-mounted cube is $Ri = 1.08$. This case may not correspond to the maximally coherent roll state since we are dealing with a different flow problem, but it is expected that it will at least show some sign of strengthening of the rolls.

The dynamics of a non-isothermal turbulent flow past a surface-mounted cube can be fully characterized by the Reynolds (Re_b), Rayleigh (Ra) and Prandtl (Pr) numbers, which can be combined forming the Richardson (Ri_b) number. Therefore, we can characterize the dynamics of the flow problem in terms of Reynolds (Re_b), Prandtl (Pr), and Richardson (Ri_b) numbers. On the other hand, the isothermal case is fully characterized by the Reynolds number (Re_b) alone.

Table 10 summarizes these nondimensional numbers for both, the isothermal and the non-isothermal cases. Note that the used Re_b is such that corresponds to a $Re_{u_h} \cong 3{,}900$, which is the Reynolds number for which the used mesh resolution was validated in Chapter 5.

	$Non-isothermal\ (Ri = 1.08)$		
	$Isothermal$		
relevant dimensionless number	$Re_b = \frac{(2H)u_b}{\nu} = 7{,}518.8$ $\downarrow$ $\left(Re_{u_h} = \frac{\rho\, U_{Inflow_at_H}\, H}{\mu} = 3{,}934.2\right)$	$Ri_b = \frac{Ra}{\mathrm{Pr}\ (Re_b)^2} = \frac{2\,\beta\, g\, \Delta\theta\, H}{{u_b}^2} = 1.08$	$Pr_{air} = \frac{\nu}{\alpha} = 0.71$

Table 10: Summary nondimensional numbers of simulated cases.

Where the relevant length-scale used for the definition of these numbers is the cube height (H), as a relevant length-scale for the rolls behind the cube, as well as for "boundary layer thickness" and the distance across which the temperature difference is imposed ($\delta_{99} = 2H$).

Regarding the setting up of the parameters of the nondimensional simulation to have the desired Richardson number, the exact same methodology described in section 4.2.3 has been used.

As introduced in section 6.1, due to time constraints, the simulations carried out in this section have been made faster at the expense of accuracy on the results, therefore the simulation settings were not the optimal ones. The numerical scheme was the same as in the isothermal flow case from Chapter 5, however, a larger time step ($CFL = 2$), and larger residual tolerances were used.

In the same way as done in previous chapters, turbulence statistics are only recorded once a statistically stationary state has been reached. In order to assess flow development, the time-evolution of the drag force is monitored. Figure 72 shows the drag force signal for the isothermal case, over a time span corresponding to the final averaging window from which the results were recorded, proving that the flow was already fully developed.

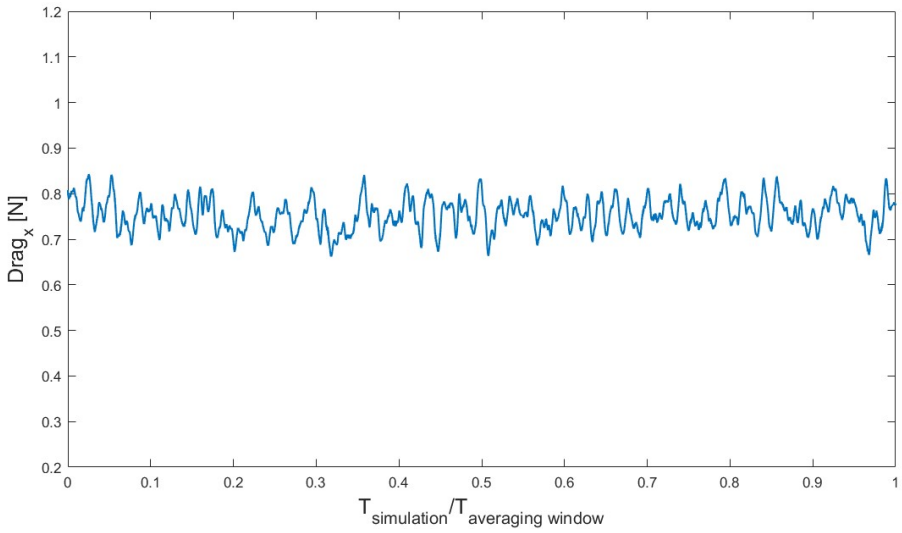


Figure 72: Time-evolution of the horizontal component of the drag force on geometry walls during the period of time corresponding to the final averaging window from which results were recorded. Time normalized by the averaging window.

Once the flow has reached an statistically steady state, statistics can be recorded. In this regard, the used averaging window is set at 100 convective-time-scales, satisfying the guidelines for isothermal flow past a surface-mounted cube described in section 5.6.

Regarding the non-isothermal case ($Ri = 1.08$), in the context of the simplified simulations in the present chapter where we only aim for a first qualitative proof of concept, a short simulation has been set up initializing the flow field using the isothermal flow solution. From the initialization, the

simulation has been running for 100 convective-time-scales, while collecting statistics. The decision of running the non-isothermal flow case for 100 convective-time-scales is not only based on the guidelines described in section 5.6, but is also based on the time required for the thermal effects to be observable, and will be described in section 6.6.

This simplified way of setting up the simulation will, of course, add inaccuracies coming from the transient effects. However, one has to bear in mind that the simulations being conducted in Chapter 6 already contain errors coming from the increased time-step and residual tolerances. Moreover, for such a weakly unstable thermal stratification condition, no transition of the overall flow structures is expected, but only a slight strengthening of them. Finally, as shown in figure 73, the time-evolution of the drag force clearly shows that the transient effects are weak.

Based on all these points, since our goal is a qualitative proof of concept of rolls strengthening, we can reasonably assume that our simulation is adequate for our purposes.

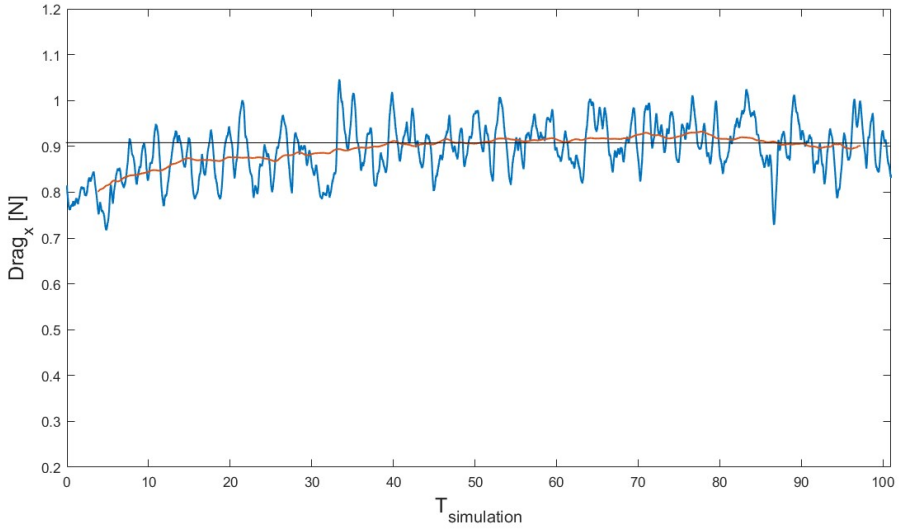


Figure 73: Time-evolution of the horizontal component of the drag force on geometry walls (blue), showing the transient of the thermal case. A moving average (orange), with a period = 1/5 of the data set, is added for visualizing convergence.

6.6 Results and Discussion

6.6.1 Isothermal Flow Case

To start with, figure 74 shows an instantaneous iso-surface of Q-criterion coloured by the velocity magnitude for the isothermal flow case, which shows a great deal of vortical structures and no rolls can be identified at all.

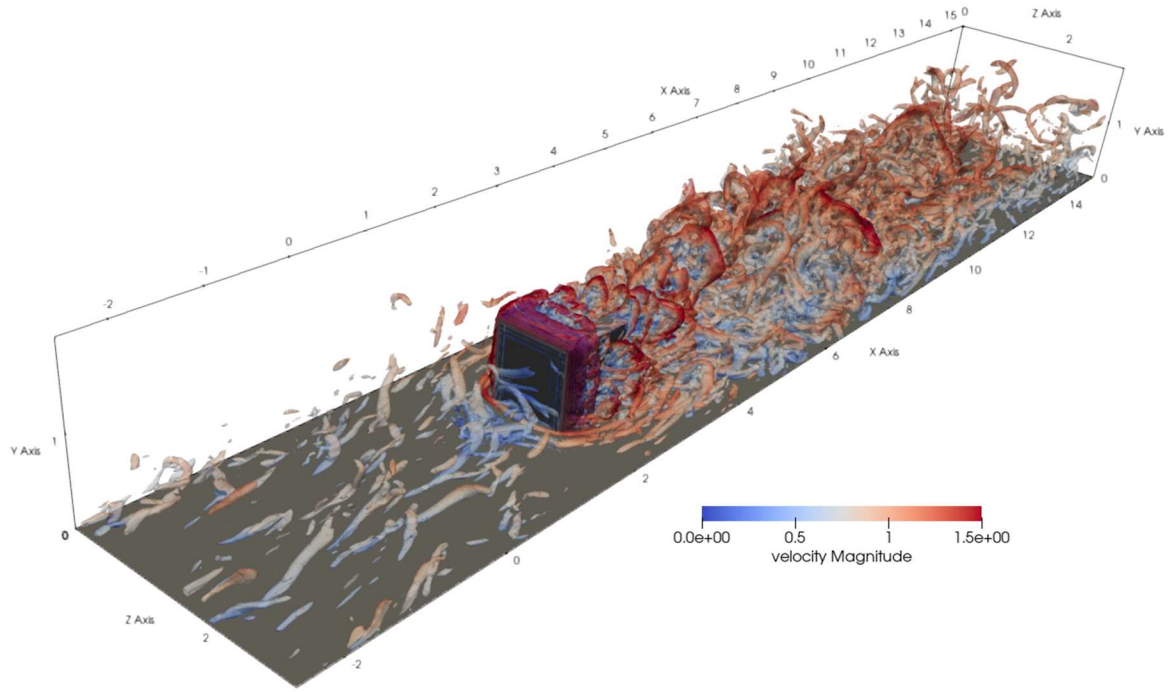


Figure 74: Instantaneous iso-surface of Q-criterion (=3) coloured by the velocity magnitude for the isothermal flow case.

However, rolls become evident when looking at the mean-flow, as it can be seen in figure 75 which shows an iso-surface of Q-criterion applied to the averaged flow for the isothermal flow case which. It is important to point out that the rolls do not look as coherent as in Chapter 5 (see figures 67-68). This is a direct consequence of having made the simulations of Chapter 6 faster by increasing time step and residual tolerances. Moreover, the used averaging window in Chapter 5 was twice the one used in the present chapter. In future works, the simulations will be repeated using the same standards as used in Chapter 5 for obtention of accurate results.

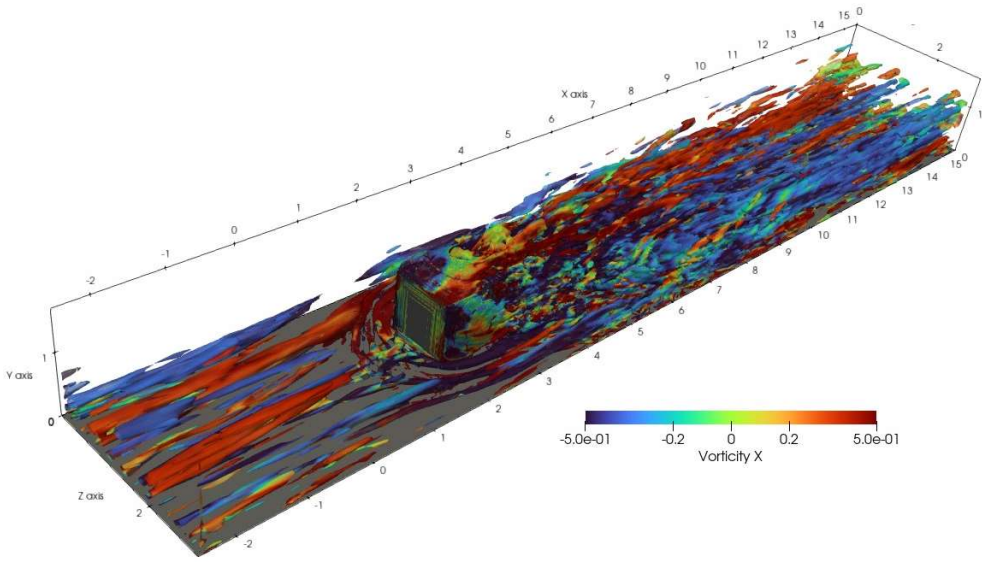


Figure 75: Iso-surface of Q-criterion (=0.03) coloured by x-vorticity component for the isothermal case.

Recall that in the non-isothermal case what we are expecting to see is if there is any strengthening of the rolls by collection of small-scale plumes. At this point one has to take into account that, if this process does indeed take place, it requires both, time and space, for its effects to be visible. Therefore, we need to make sure that our domain and our simulation time are large enough. These constraints have already been hinted in the present chapter, pointing out the importance of the required length of the domain and the required simulation time, in sections 6.3 and 6.5 respectively.

As introduced in section 6.5, the simulation time for the non-isothermal flow case has to be selected taking into account the speed of rotation of the mean-flow rolls. The reason for this lies in the fact that enough time needs to be allowed for the rolls to strengthen themselves by collecting small-scale plumes. Therefore, for the thermal effects to be sensed, the used simulation time should allow for a few entire rotations of the mean-flow rolls. In order to get an estimate of the rotation velocity of the rolls, the results from the isothermal case will be used.

From observation of the results in figure 75, the mean-flow rolls have a diameter of $\sim 0.1H$ when they are created, and reach around $\sim H$ at the end of the domain. Therefore, we use $L_{rolls} \sim 0.5H$ as the average characteristic length-scale of the rolls. On the other hand, from figure 76, one can obtain an estimate of the tangential velocity of the rolls, which can be estimated to be $u_{tangential} \sim 0.1\ m/s$, meaning that the rotation velocity of the rolls can be approximated by:

$$\omega_{rolls} \sim \frac{u_{tangential}}{L_{rolls}} \sim \frac{0.1\ m/s}{\frac{0.5\ m}{2}} = 0.4 \frac{rad}{s} = 0.064\ \frac{rev}{s} \rightarrow \sim \frac{15.6\ s}{1\ rotation}$$

From this estimate of the velocity of rotation of the rolls, we can conclude that our non-isothermal simulation running for $100s$ guarantees that the rolls will perform more than 6 entire rotations, which we consider enough for thermal effects to be visible.

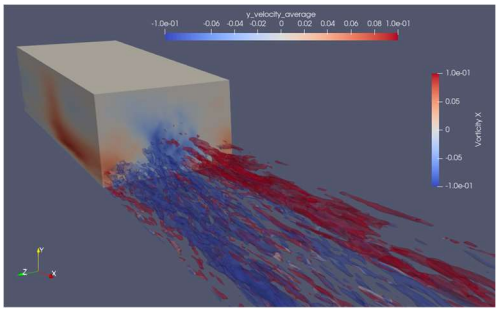
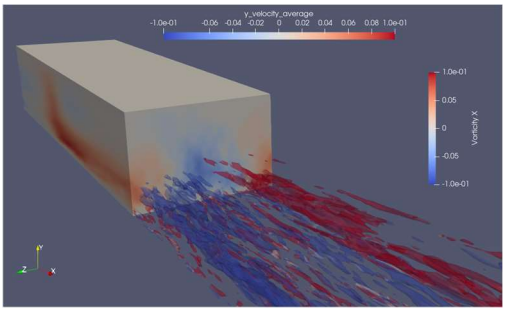
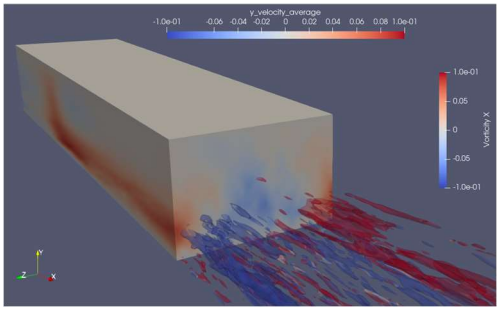
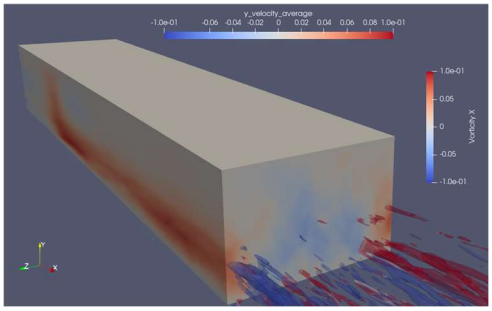
At a distance of $3H$ downstream of the cube	At a distance of $5H$ downstream of the cube
	
At a distance of $7H$ downstream of the cube	At a distance of $9H$ downstream of the cube
	

Figure 76: From the results at different planes downstream of the cube it can be observed that 0.1m/s is a good estimate for the tangential velocity of the rolls along most of the domain. Each of the pictures consists of a sliced domain showing the wall-normal velocity component together with an iso-surface of Q-criterion coloured by x-vorticity sign, for visualization of the rolls.

Finally, regarding the domain length, in section 6.3, it was introduced that the chosen length of the domain was selected expecting it to allow for an entire rotation of the mean-flow rolls before they are advected out of the domain. To verify this, a simple estimate can be computed based on the residence time of fluid elements in the wake of the cube before they are advected out of the domain:

$$t_{residence} \sim \frac{Wake\ length}{Bulk\ Velocity} \sim \frac{12.5\ m}{1\frac{m}{s}} = 12.5\ s$$

Which, recalling that the rolls take $\sim 15.6\ s$ to perform an entire rotation, means that with the used wake length, the mean-flow rolls can perform $\sim 80\%$ of a rotation before they are advected outside of the domain. This result obtained based on an order-of-magnitude argument coincides with what can be observed in figure 77, where the averaged velocity field is used to draw some streamlines.

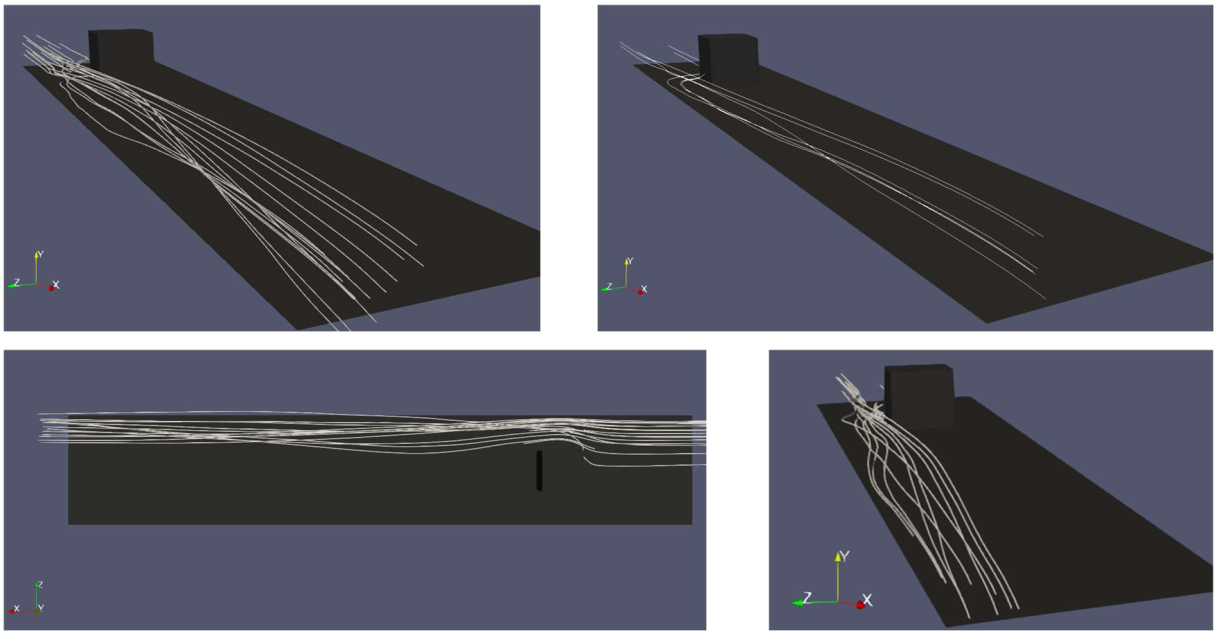


Figure 77: Streamlines of the averaged velocity field for the isothermal case.

Therefore, we can conclude that, despite not being ideal, our domain length and simulation running time are enough since they are able to capture almost an entire roll rotation in space, while more than 6 roll rotations can be captured in time. In conclusion, these parameters should be enough for the thermal effects to be visible, however, ideally we would target for even longer domain lengths and longer running times, together with domain-size independence studies.

6.6.2 Non-Isothermal Flow Case

Finally, the thermal stratification effects on the rolls behind the cube for the $Ri = 1.08$ case are assessed, in order to determine whether or not they become stronger and more persistent. To that end, figures 78-87 present slices of x-vorticity (component aligned with the rolls axis) together with 2D planar streamlines (v- and w- components of velocity), at different distances downstream of the cube.

It can be concluded that the slices consistently show that the roll structure of the non-isothermal case ($Ri = 1.08$) case is stronger compared to the isothermal one, which can be seen by larger x-vorticity values. Moreover, the rolls for the non-isothermal case are also more persistent in space, meaning that they show a high degree of coherency further downstream from the cube, as compared to the isothermal case.

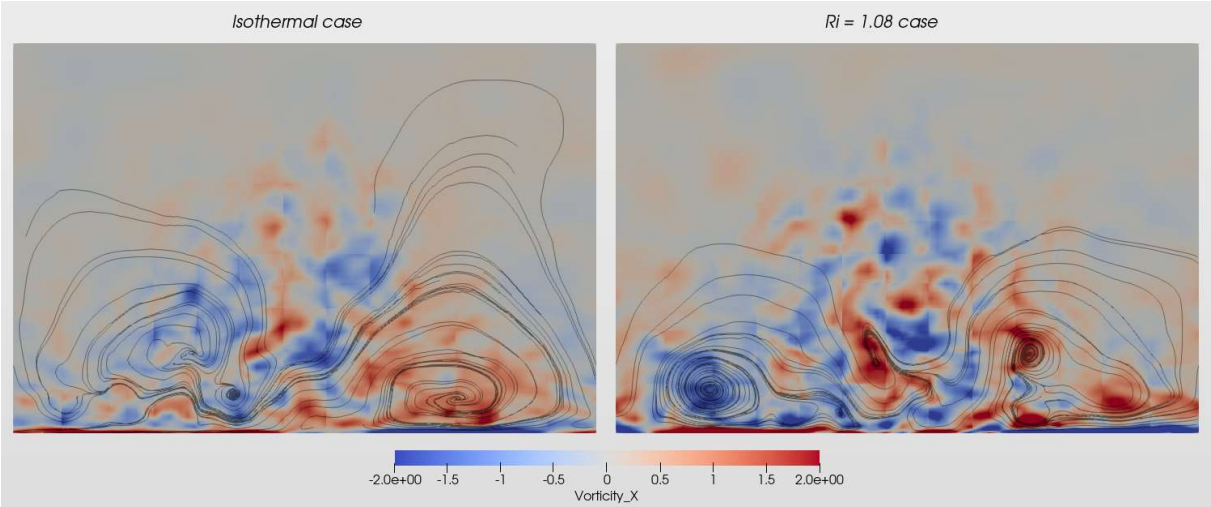


Figure 78: x-vorticity component and planar streamlines at a distance 2 cube-heights downstream of the cube.

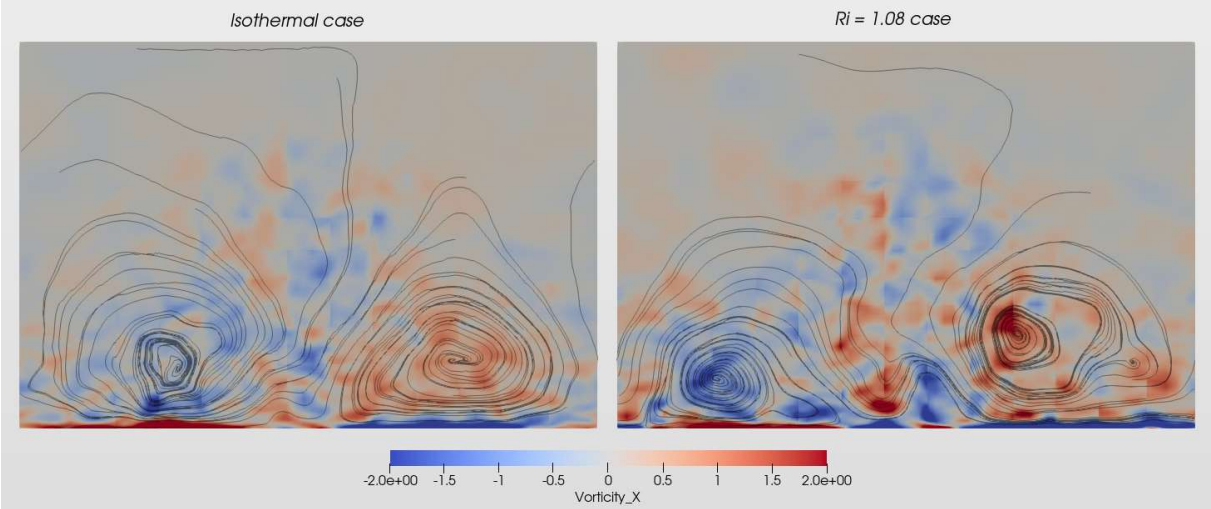


Figure 79: x-vorticity component and planar streamlines at a distance 3 cube-heights downstream of the cube.

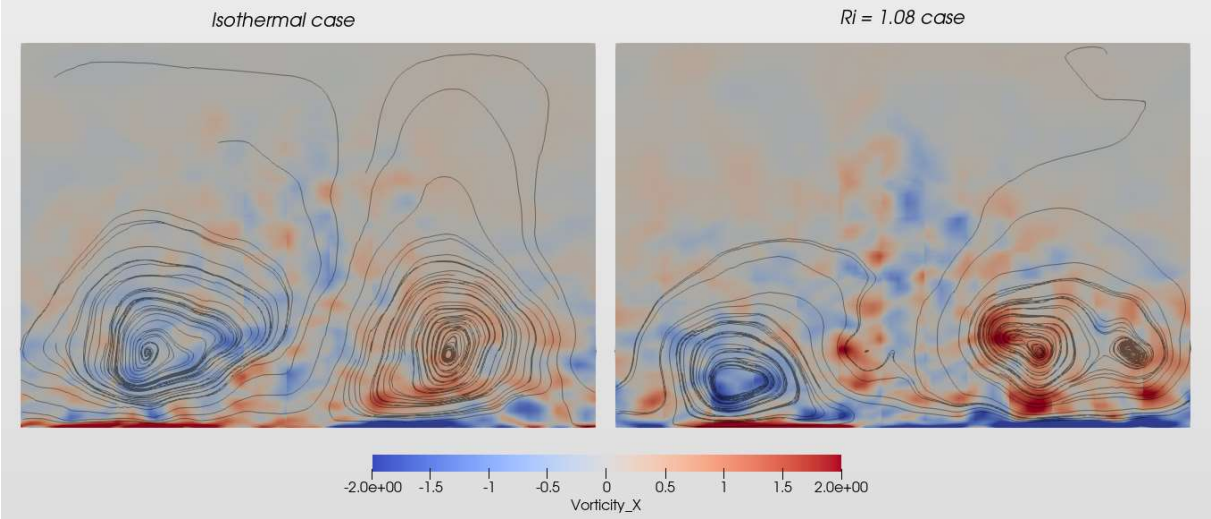


Figure 80: x-vorticity component and planar streamlines at a distance 4 cube-heights downstream of the cube.

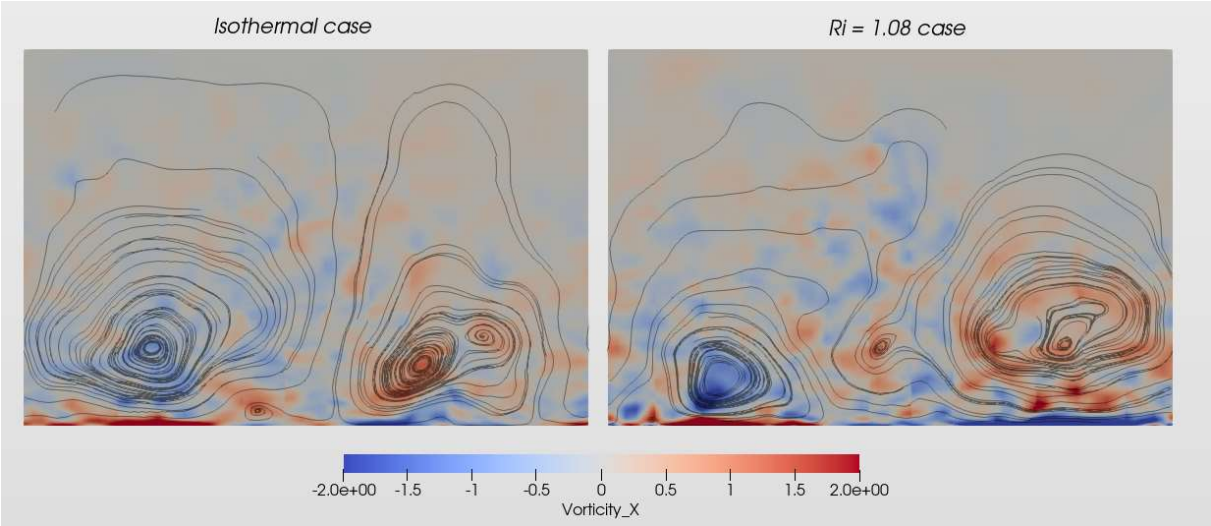


Figure 81: x-vorticity component and planar streamlines at a distance 5 cube-heights downstream of the cube.

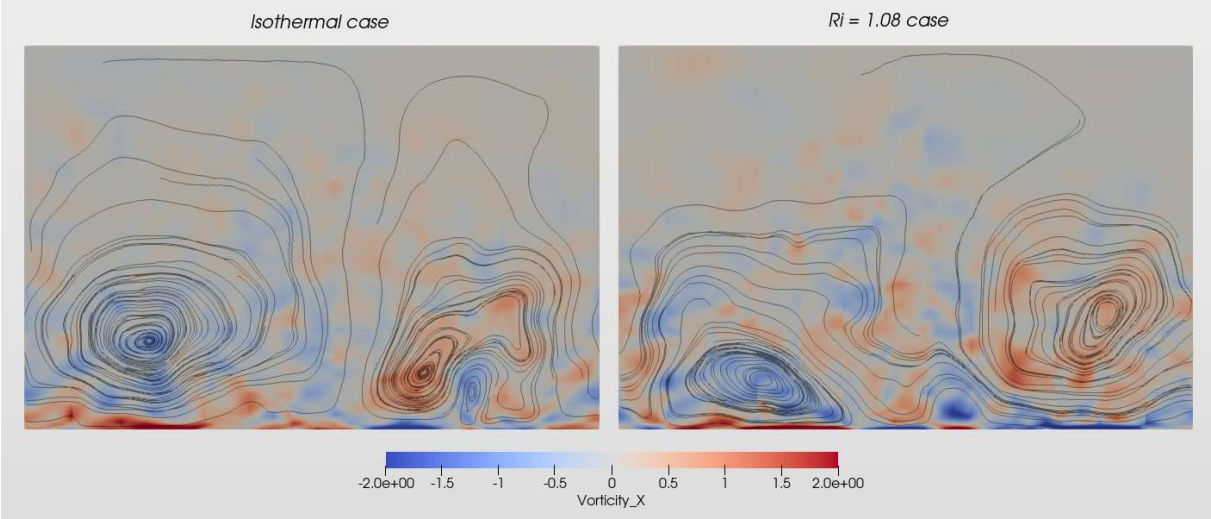


Figure 82: x-vorticity component and planar streamlines at a distance 6 cube-heights downstream of the cube.

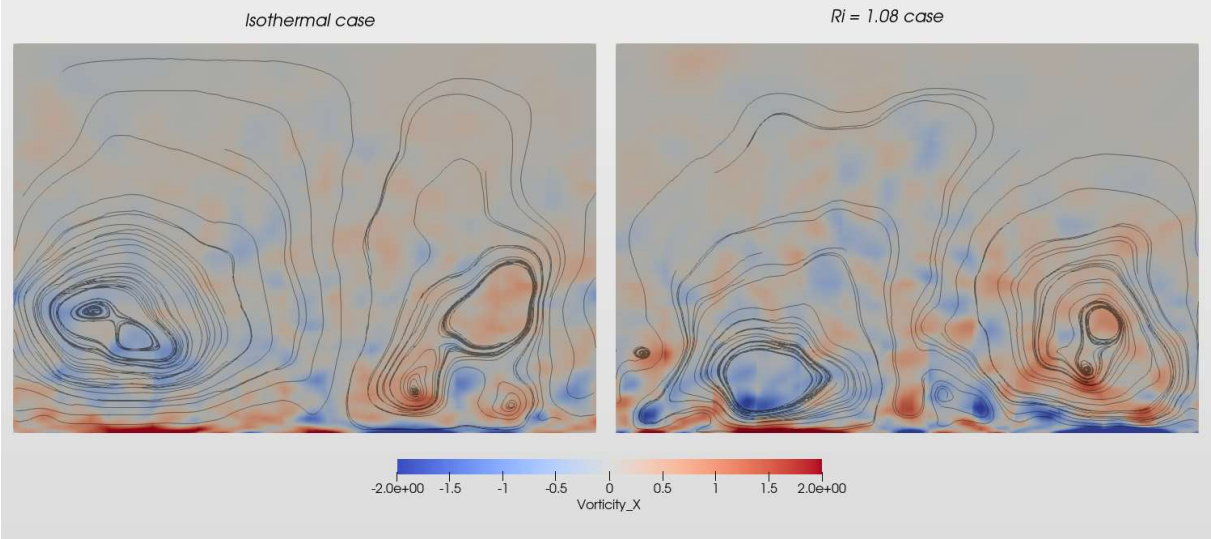


Figure 83: x-vorticity component and planar streamlines at a distance 7 cube-heights downstream of the cube.

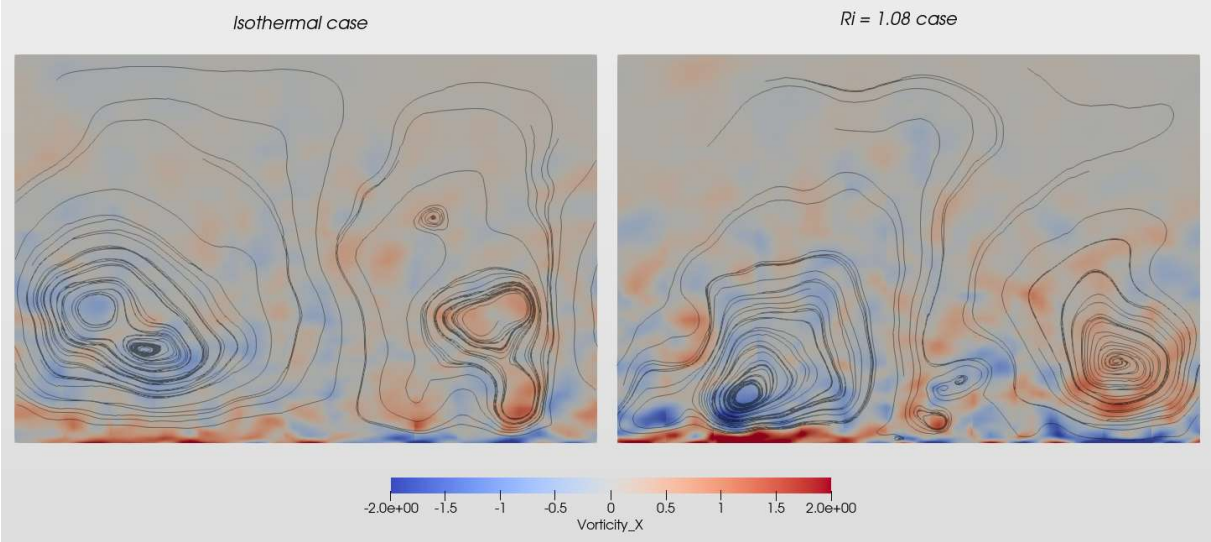


Figure 84: x-vorticity component and planar streamlines at a distance 8 cube-heights downstream of the cube.

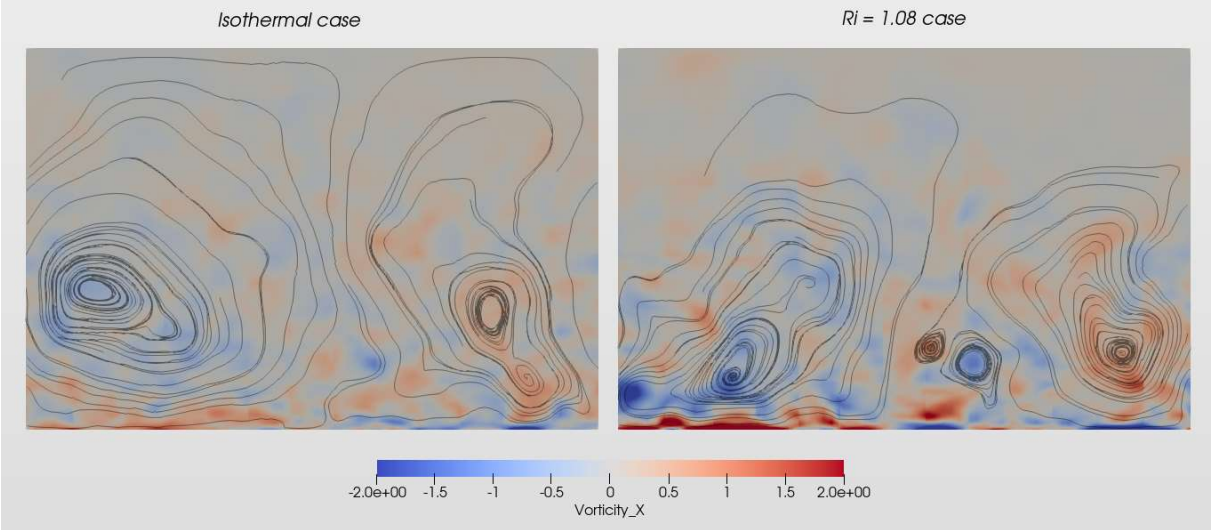


Figure 85: x-vorticity component and planar streamlines at a distance 9 cube-heights downstream of the cube.

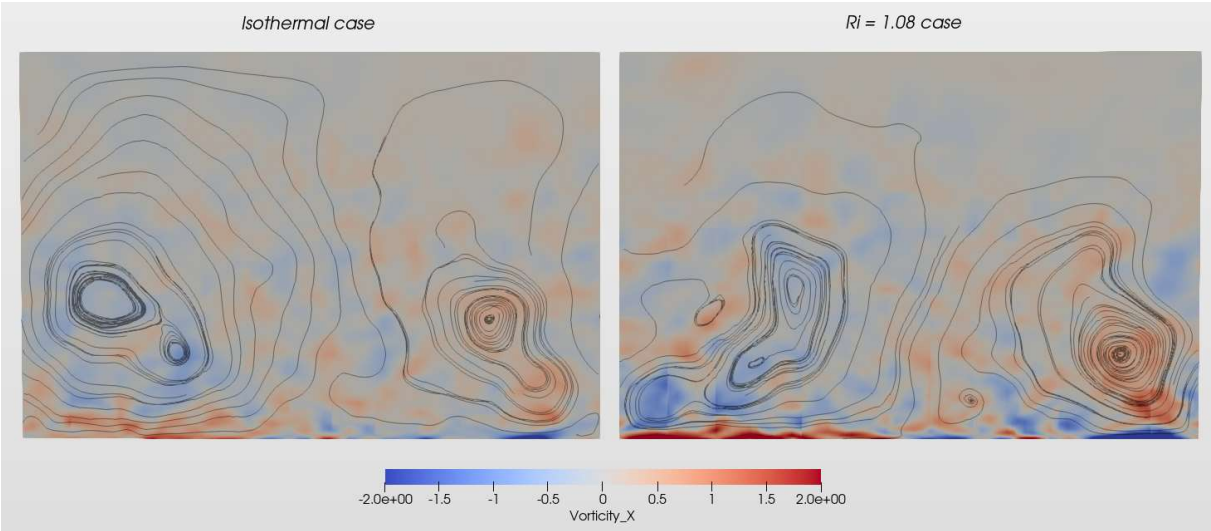


Figure 86: x-vorticity component and planar streamlines at a distance 10 cube-heights downstream of the cube.

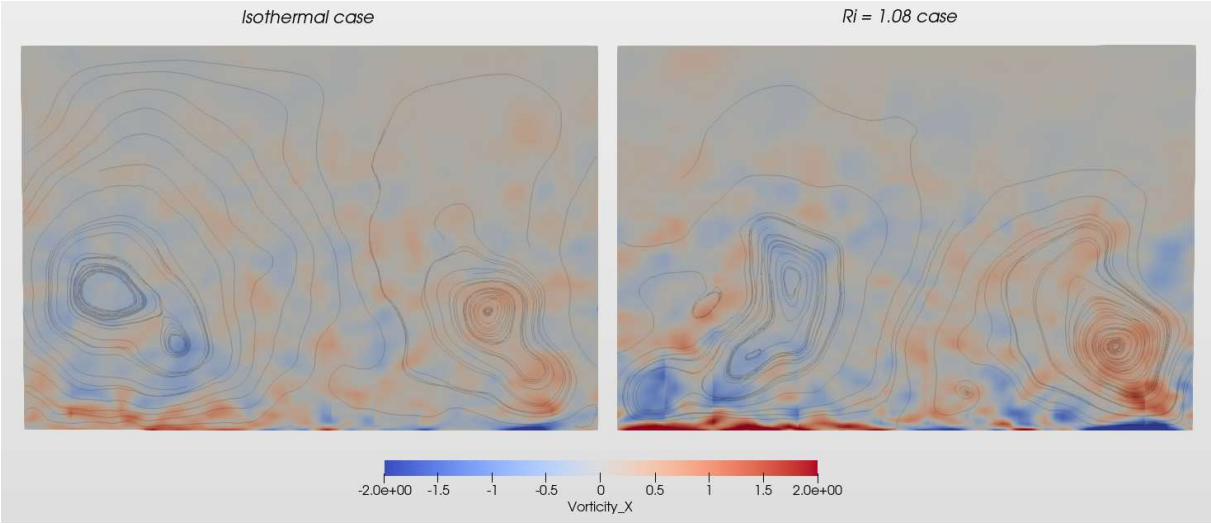


Figure 87: Slice at distance 10 cube-heights with streamlines made transparent for better visualization of the vorticity magnitude.

Finally, the strengthening of the rolls behind the cube under weakly unstable thermal stratification conditions can also be seen in figures 88-90, where iso-surfaces of Q-criterion coloured by x-vorticity are represented.

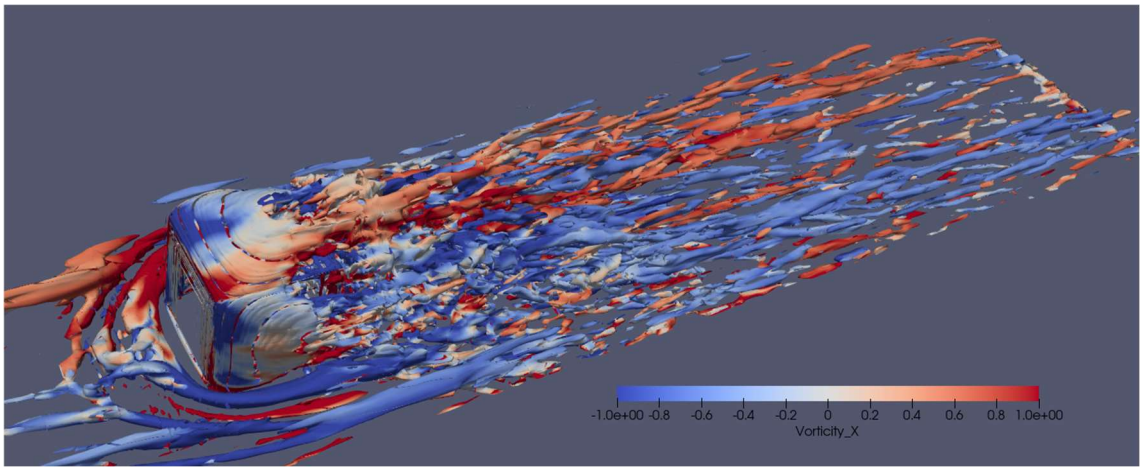


Figure 88: Iso-surface of Q-criterion (=0.1) coloured by x-vorticity component for the isothermal case.

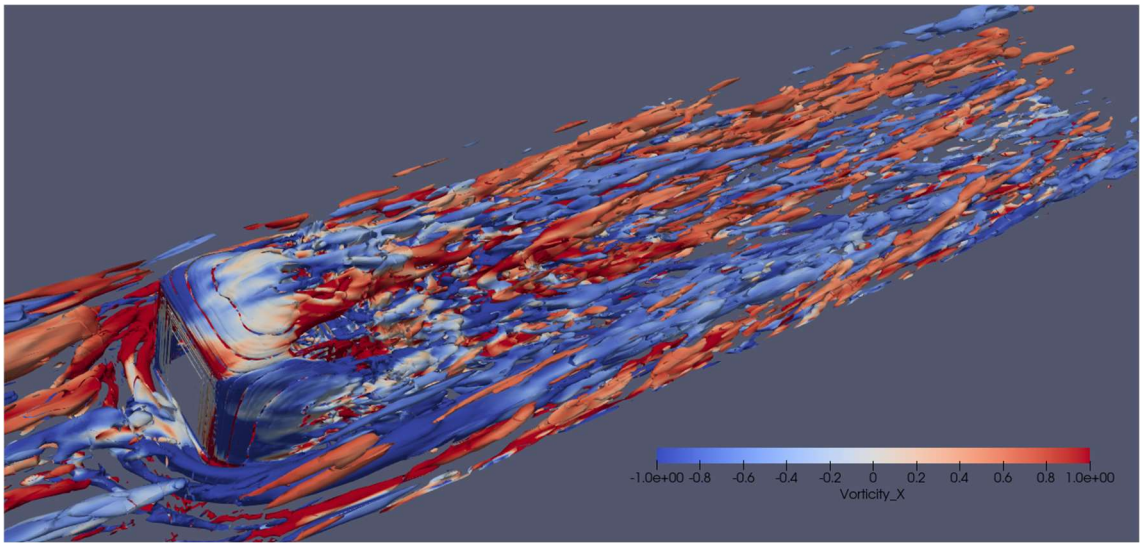


Figure 89: Iso-surface of Q-criterion (=0.1) coloured by x-vorticity component for the non-isothermal case (Ri = 1.08).

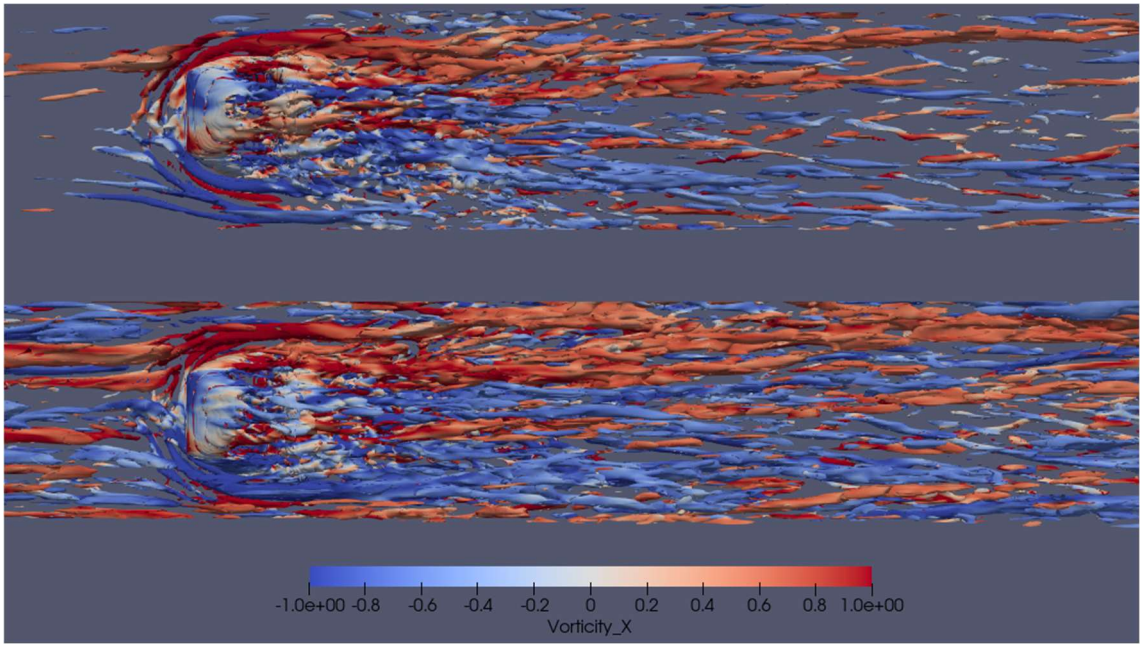


Figure 90: Iso-surface of Q-criterion (=0.1) coloured by x-vorticity component for the isothermal case (top) and the non-isothermal case Ri=1.08 (bottom). Comparison proves the strengthening of the rolls.

Chapter 7

Conclusions and Future Work

The present research work has been motivated by an unintuitive observation by Jayaraman & Brasseur (2021) [4] on the study of the transition of the atmospheric boundary layer (ABL) structure, from neutral to moderately convective. Such observation was a non-monotonic evolution of the streamwise coherence lengths, which represent the length of streamwise coherent structures, for increasingly stronger unstable thermal stratification conditions. Such observation evinced the existence of a sweet-spot where the large-scale roll structures, characteristic of weakly unstable stratified atmospheric boundary layers, become stronger and more persistent in space.

The reason for such behaviour was attributed to the nature of the mechanism for large-scale atmospheric rolls formation, where large-scale counter-rotating vortical structures (i.e. large-scale hairpin packets), characteristic of any isothermal turbulent boundary layer, were able to strengthen themselves by collecting small-scale thermal plumes, eventually creating the large-scale rolls. The importance of these findings lies in the fact that large-scale atmospheric rolls are known to be one of the most important structures when it comes to vertical transport of momentum and scalars (i.e. pollutants) in the ABL [5].

At this point, one can realise that the flow structure appearing in the flow past a high-rise building, which can be modelled as a surface-mounted prism, consists of two counter-rotating vortical structures that look quite similar to the large-scale structures of the turbulent boundary layer (large-scale hairpins). Furthermore, for a high-rise building, those counter-rotating vortical structures can even show the same scaling with respect to the boundary layer thickness (δ_{BL}) as shown by the large-scale hairpins in the turbulent boundary layer ($\sim 0.2\delta_{BL}$) [10]. This indicates that the counter-rotating rolls appearing behind a high-rise building could potentially exhibit the same behaviour as observed by Jayaraman & Brasseur (2021) and strengthen themselves under certain conditions by collecting small-scale thermal plumes. If this was the case, it would enhance large-scale vertical mixing which could be beneficial for street canyon ventilation, reducing urban pollution levels. Therefore, the

importance of studying the evolution of the roll structures behind a high-rise building under different thermal stratification conditions becomes evident.

In this regard, the present research work has succeeded in providing a qualitative proof of concept of the presented hypothesis, proving that the rolls behind a surface-mounted cube (model for a high-rise building) under weakly unstable thermal stratification conditions do strengthen themselves in a similar manner as observed by Jayaraman & Brasseur (2021) for the ABL. Moreover, a reliable LES numerical model for simulating flow past a surface-mounted cube (high-rise building) has been built and thoroughly validated against DNS data, tuning the optimal mesh, and simulation and filtering settings.

During the limited period of time of the present thesis work, only one thermal stratification condition could be tested, $Ri = 1.08$. Moreover, the final simulations were made faster at the expense of accuracy due to time constraints. Future work will use the developed model with the proper settings to conduct simulations for a wide range of Richardson numbers, ranging from neutral to moderately convective, in order to fully characterize the behaviour of the rolls behind a high-rise building and identify the condition at which the maximum coherence lengths are obtained (maximally coherent roll state). Furthermore, passive scalars will be added to study the effects that the thermal-induced strengthening of the rolls behind a high-rise building can have on pollution dispersion in urban environments. However, before conducting this series of experiments, a domain-size independency study will need to be conducted in order to determine the required wake length and domain width for not constraining the rolls.

REFERENCES

[1] J. M. Tomas, M. J. B. M. Pourquie, and H. J. J. Jonker, 'Stable Stratification Effects on Flow and Pollutant Dispersion in Boundary Layers Entering a Generic Urban Environment', *Boundary-Layer Meteorology*, vol. 159, no. 2, pp. 221–239, May 2016.

[2] F. T. M. Nieuwstadt, J. Westerweel, and B. J. Boersma, *Turbulence: Introduction to Theory and Applications of Turbulent Flows*. Springer International Publishing, 2016.

[3] Roland B. Stull, *An Introduction to Boundary Layer Meteorology*. Springer Dordrecht, 1988.

[4] B. Jayaraman and J. G. Brasseur, 'Transition in atmospheric boundary layer turbulence structure from neutral to convective, and large-scale rolls', *Journal of Fluid Mechanics*, vol. 913, Apr. 2021.

[5] D. Etling and R. A. Brown, 'Roll vortices in the planetary boundary layer: A review', *Boundary-Layer Meteorology*, vol. 65, no. 3, pp. 215–248, Aug. 1993.

[6] T. M. Weckwerth, J. W. Wilson, R. M. Wakimoto, and N. A. Crook, 'Horizontal Convective Rolls: Determining the Environmental Conditions Supporting their Existence and Characteristics', *Mon. Wea. Rev.*, vol. 125, no. 4, pp. 505–526, Apr. 1997.

[7] S. Khanna and J. G. Brasseur, 'Three-Dimensional Buoyancy- and Shear-Induced Local Structure of the Atmospheric Boundary Layer', *Journal of the Atmospheric Sciences*, vol. 55, no. 5, pp. 710–743, Mar. 1998.

[8] B. Jayaraman and J. Brasseur, 'Transition in Atmospheric Turbulence Structure from Neutral to Convective Stability States', in *32nd ASME Wind Energy Symposium*, National Harbor, Maryland, Jan. 2014.

[9] B. Jayaraman and J. G. Brasseur, 'The Surprising Transition in Atmospheric Boundary Layer Turbulence Structure from Neutral to Moderately Convective Stability States and Mechanisms Underlying Large-scale Rolls'. Physics, Environmental Science, Dec. 07, 2018.

[10] R. J. Adrian, 'Hairpin vortex organization in wall turbulence', *Physics of Fluids*, vol. 19, no. 4, p. 041301, Apr. 2007.

[11] G. E. Elsinga, R. J. Adrian, B. W. Van Oudheusden, and F. Scarano, 'Three-dimensional vortex organization in a high-Reynolds-number supersonic turbulent boundary layer', *J. Fluid Mech.*, vol. 644, pp. 35–60, Feb. 2010.

[12] R. Martinuzzi and C. Tropea, 'The Flow Around Surface-Mounted, Prismatic Obstacles Placed in a Fully Developed Channel Flow (Data Bank Contribution)', *Journal of Fluids Engineering*, vol. 115, no. 1, pp. 85–92, Mar. 1993.

[13] J. Kim, P. Moin, and R. Moser, 'Turbulence statistics in fully developed channel flow at low Reynolds number', *J. Fluid Mech.*, vol. 177, pp. 133–166, Apr. 1987.

[14] R. D. Moser, J. Kim, and N. N. Mansour, 'Direct numerical simulation of turbulent channel flow up to Reτ=590', *Physics of Fluids*, vol. 11, no. 4, pp. 943–945, Apr. 1999.

[15] M. Lee and R. D. Moser, 'Direct numerical simulation of turbulent channel flow up to Reτ=5200', *Journal of Fluid Mechanics*, vol. 774, pp. 395–415, Jul. 2015.

[16] S. Pirozzoli, M. Bernardini, R. Verzicco, and P. Orlandi, 'Mixed convection in turbulent channels with unstable stratification', *J. Fluid Mech.*, vol. 821, pp. 482–516, Jun. 2017.

[17] S. Haering, R. Balakrishnan, and R. Kotamarthi, 'Direct Numerical Simulation of Flow Over a Wall Mounted Cube with the Nek5000 Spectral Element Code: DNS at Reh = 3900', ANL/CPS-21/1, Jul. 2021.

[18] P. Moin and K. Mahesh, 'DIRECT NUMERICAL SIMULATION: A Tool in Turbulence Research', *Annu. Rev. Fluid Mech.*, vol. 30, no. 1, pp. 539–578, Jan. 1998.

[19] R. D. Moser and P. Moin, 'The effects of curvature in wall-bounded turbulent flows', *J. Fluid Mech.*, vol. 175, no. 1, p. 479, Feb. 1987.

[20] A. T. Patera, 'A spectral element method for fluid dynamics: Laminar flow in a channel expansion', *Journal of Computational Physics*, vol. 54, no. 3, pp. 468–488, Jun. 1984.

[21] P. M. K. Prasad, 'Comprehensive assessment of NEK5000 DNS capabilities: Turbulent Channel Flow and Conjugate Heat transfer', 2016.
[22] M. O. Deville, P. F. Fischer, and E. H. Mund, *High-Order Methods for Incompressible Fluid Flow*. Cambridge: Cambridge University Press, 2002.
[23] P. Fischer and J. Mullen, 'Filter-based stabilization of spectral element methods', *Comptes Rendus de l'Académie des Sciences - Series I - Mathematics*, vol. 332, no. 3, pp. 265–270, Feb. 2001.
[24] S. Stolz, P. Schlatter, and L. Kleiser, 'High-pass filtered eddy-viscosity models for large-eddy simulations of transitional and turbulent flow', *Physics of Fluids*, vol. 17, no. 6, p. 065103, Jun. 2005.
[25] K. Morishita, T. Ishihara, and Y. Kaneda, 'Small-scale statistics in direct numerical simulation of turbulent channel flow at high-Reynolds number', *J. Phys.: Conf. Ser.*, vol. 318, no. 2, p. 022016, Dec. 2011.
[26] K. Morishita, T. Ishihara, and Y. Kaneda, 'Length Scales in Turbulent Channel Flow', *J. Phys. Soc. Jpn.*, vol. 88, no. 6, p. 064401, Jun. 2019.
[27] R. D. Moser and P. Moin, 'Direct Numerical Simulation of Curved Turbulent Channel Flow', p. 170, 1984.
[28] J. Jimenez, 'Computing high-Reynolds-number turbulence: will simulations ever replace experiments?', *J. of Turbulence*, vol. 4, p. N22, Jun. 2003.
[29] P. S. Negi, R. Vinuesa, A. Hanifi, P. Schlatter, and D. S. Henningson, 'Unsteady aerodynamic effects in small-amplitude pitch oscillations of an airfoil', *International Journal of Heat and Fluid Flow*, vol. 71, pp. 378–391, Jun. 2018.
[30] P. J. Mason and N. S. Callen, 'On the magnitude of the subgrid-scale eddy coefficient in large-eddy simulations of turbulent channel flow', *J. Fluid Mech.*, vol. 162, no. 1, p. 439, Jan. 1986.
[31] 'Nek5000 — Nek5000 documentation'. https://nek5000.github.io/NekDoc/index.html.
[32] S. Pirozzoli, M. Bernardini, and P. Orlandi, 'Passive scalars in turbulent channel flow at high Reynolds number', *J. Fluid Mech.*, vol. 788, pp. 614–639, Feb. 2016, doi: 10.1017/jfm.2015.711.
[33] D. D. Gray and A. Giorgini, 'The validity of the boussinesq approximation for liquids and gases', *International Journal of Heat and Mass Transfer*, vol. 19, no. 5, pp. 545–551, May 1976.
[34] O. Shishkina, R. J. A. M. Stevens, S. Grossmann, and D. Lohse, 'Boundary layer structure in turbulent thermal convection and its consequences for the required numerical resolution', *New J. Phys.*, vol. 12, no. 7, p. 075022, Jul. 2010.
[35] E. R. Meinders, K. Hanjalic, and R. J. Martinuzzi, 'Experimental Study of the Local Convection Heat Transfer From a Wall-Mounted Cube in Turbulent Channel Flow', *Journal of Heat Transfer*, vol. 121, no. 3, pp. 564–573, Aug. 1999.
[36] A. Yakhot, H. Liu, and N. Nikitin, 'Turbulent flow around a wall-mounted cube: A direct numerical simulation', *International Journal of Heat and Fluid Flow*, vol. 27, no. 6, pp. 994–1009, Dec. 2006.
[37] W. Rodi, J. H. Ferziger, M. Breuer, and M. Pourquie, 'Status of Large Eddy Simulation: Results of a Workshop', *Journal of Fluids Engineering*, vol. 119, no. 2, pp. 248–262, Jun. 1997.
[38] M. Stuck, A. Vidal, P. Torres, H. M. Nagib, C. Wark, and R. Vinuesa, 'Spectral-Element Simulation of the Turbulent Flow in an Urban Environment', *Applied Sciences*, vol. 11, no. 14, Art. no. 14, Jan. 2021.
[39] H. Helmholtz, 'Über Integrale der hydrodynamischen Gleichungen, welche den Wirbelbewegungen entsprechen.', *Journal für die reine und angewandte Mathematik*, vol. 55, pp. 25–55, 1858.
[40] P. Gousseau, B. Blocken, and G. J. F. van Heijst, 'Large-Eddy Simulation of pollutant dispersion around a cubical building: Analysis of the turbulent mass transport mechanism by unsteady concentration and velocity statistics', *Environmental Pollution*, vol. 167, pp. 47–57, Aug. 2012.
[41] J. Hunt, A. Wray, and P. Moin, 'Eddies, streams, and convergence zones in turbulent flows', *Studying Turbulence Using Numerical Simulation Databases*, vol. 1, pp. 193–208, Nov. 1988.
[42] J. Jeong and F. Hussain, 'Hussain, F.: On the identification of a vortex. JFM 285, 69-94', *Journal of Fluid Mechanics*, vol. 285, pp. 69–94, Feb. 1995.